Title
Bandgap Engineering of NiO-CdO

Author
Francis, Christopher

Publication Date
2017

Peer reviewed|Thesis/dissertation

Bandgap Engineering of NiO-CdO

by

Christopher Francis

A dissertation submitted in partial satisfaction of the
requirements for the degree of

Doctor of Philosophy

in

Engineering — Materials Science and Engineering

in the

Graduate Division

of the

University of California, Berkeley

Committee in charge:

Professor Oscar D. Dubón, Chair
Professor Jie Yao
Professor Ali Javey

Summer 2017

Bandgap Engineering of NiO-CdO

Abstract

Bandgap Engineering of NiO-CdO

by

Christopher Francis

Doctor of Philosophy in Materials Science and Engineering

University of California, Berkeley

Professor Oscar D. Dubón, Chair

Understanding and controlling the electronic structure of materials are longstanding endeavors in semiconductor physics and technology, especially in the transparent conducting oxide community. In thin films of CdO and NiO, such control has been attempted on these individual materials through alloying with other binary oxides. No such studies, however, exist on the electronic structure evolution of the combined CdO-NiO alloy system. This dissertation addresses this issue by conducting and reporting a bandgap engineering study on $Ni_xCd_{1-x}O$ alloys.

This dissertation first reviews previous bandgap engineering studies performed on other systems, initially focusing on alloying and later focusing on other advanced bandgap engineering methods. A discussion of the earliest point defect and ADM theory studies then justifies the dissertation's selection of CdO—it's strong electrical properties are suitable for bandgap engineering. Investigations of previous literature involving the Group II-oxides of ZnO, MgO, and CdO lead to two key conclusions. First, few studies exist in which CdO is a primary alloying material. Second, the properties of CdO are tunable with better complementary materials such as NiO, a transition metal (TM) oxide, instead of commonly used ZnO and MgO. Given their unique properties, there is an opportunity to investigate the structure, properties, and behavior of CdO system after alloying it with NiO. Hall effect, optical reflectance and transmittance and X-ray diffraction measurements are utilized first and the structural, electrical transport, and optical properties of $Ni_xCd_{1-x}O$ films sputtered in argon (Ar) with radio frequency (RF) magnetron are then reported.

This initial study shows that $Ni_xCd_{1-x}O$ alloys are rocksalt-structured and exhibit a monotonic shift of the (220) diffraction peak to higher 2θ angles with increasing Ni concentration. The electron mobility and electron concentration decrease with increasing Ni—becoming highly resistive for Ni content greater than 43.4% Ni. This decrease in n-type conductivity is consistent with the movement expected from a virtual crystal approximation (VCA) of the conduction band minimum (CBM) from below to above the Fermi stabilization energy (E_{FS}). The optical absorption edge of the alloys is tunable from CdO to NiO. An intrinsic, carrier-free bandgap of the alloys, E_g, was calculated from the electrical and optical measurements, accounting for Burstein-Moss carrier filling and carrier-induced bandgap correlation effects. An unusual super linear composition

dependence of the intrinsic bandgap is revealed when accounting for these effects. The super linear behavior was initially attributed to an interaction between the conduction-band extended states and localized donor and acceptor *d*-states of Ni.

To probe the mechanisms behind the anomalous electrical transport and optical behaviors of the Ar sputtered alloys a collection of experimental and modeling investigations via ion irradiation, band anticrossing (BAC) simulations and X-ray Photoelectron Spectroscopy-Ultraviolet Photoelectron Spectroscopy (XPS-UPS) was then used. This study discovered that the introduction of a TM with two impurity levels leads to interactions that reconstruct both the conduction and valence bands of the alloy with increasing Ni. Irradiation of the films leads to a saturation of the electron concentration associated with the pinning of the Fermi level at E_{FS}. The composition dependence of the pinned E_F enables determination of the CBM energy relative to the vacuum level. There is an unusually strong deviation of this CBM energy observed from the VCA which is then explained by a BAC interaction between localized 3*d* states of Ni and the extended states of the $Ni_xCd_{1-x}O$ alloy host. The resulting band structure is responsible for the dependence on composition of the electrical and optical properties of the alloys, the rapid reduction of the electron mobility, and previously observed positive bandgap bowing parameter. XPS-UPS studies confirm that the Γ- and L-point valence band maxima in the Cd-rich alloys are unaffected by interactions with Ni *d*-states. The results from this study provide much-needed context to the previously reported, but unexplained, electrical transport and optical behavior found in $Ni_xCd_{1-x}O$, $Ni_xMg_{1-x}O$ and $Ni_{1-x}Zn_xO$ alloys—the interactions govern their measured electrical and optical properties. These breakthroughs are also applicable to metal-oxide-based semiconducting alloys with TM acting as the dopant or alloying agents—such as V-doped ZnO.

With an understanding of the structure, properties, and behavior of n-type, Ar sputtered $Ni_xCd_{1-x}O$, exploratory work for applications was then conducted. First, the electrochemical modification of these alloys for electrochromic windows was completed and the resulting electrical transport and optical properties were reported. Second, separate studies on the modification of $Ni_xCd_{1-x}O$ with the percent of O_2 sputtering gas were implemented to evoke p-type conductivity for p-n junctions and hole emitter applications. Following this growth method, rapid thermal annealing studies under N_2 and O_2-rich environments were conducted. These studies probed the defect mechanisms and discussed the optimal processing conditions that encourage the growth of reproducible and measurable p-type conductivity in $Ni_xCd_{1-x}O$. By altering the percent of O_2 in the growth ambient, $Ni_xCd_{1-x}O$ films with tunable electrical transport properties and charge type are realized—the first such result of its kind. This dissertation concludes with a proposal for the future studies that can provide additional information on $Ni_xCd_{1-x}O$ and other metal-oxides as a result.

Overall, this dissertation makes exciting contributions to the general area of semiconductor science while shedding light on fundamental processes at the intersection of chemistry, materials science and processing, and solid-state physics. With this greater understanding, we can now proceed with tuning $Ni_xCd_{1-x}O$ for transparent electronic, photovoltaic, and photoelectrochemical applications, which require its components to have tailored electrical transport and optical properties for effective use.

Acknowledgments

The last five years were an incredible ride of highs and lows. I need to thank my mentors, family, colleagues, and friends for helping me get through this thing-especially during the times that I felt like quitting. I thank Professor Oscar Dubón. Oscar dared me to be a better researcher and to delve deeper into topics than I ever could have on my own. There is no doubt that the person who walked into onto the Berkeley campus on day one and the person leaving five years later are two completely different people knowledge-wise and professionally because of him. I learned how to conduct proper, honest, and thorough research because of his mentorship. These values will be vital to my future experiences. What I valued the most from Oscar was that he cared about me not only as a researcher and asset to his group but, more importantly, as a person. It is rare to find an understanding, accommodating, and reasonable mentor and I'm glad that I was brought in contact with someone who champions the students first before himself. Thank you for allowing me to dictate my path and being open to feedback. Thank you for being patient with me. I am also very fortunate that he also put me in contact with Dr. Wladek Walukiewicz and Dr. Kin Man Yu. They facilitated a laid-back but intense environment that fit my personality. They were always accommodating and helped me figure out my project many years ago when I felt directionless. They also trained me on many of the instruments that I became a super-user of and that I used for this dissertation. I thank you three for taking a chance on me. As well, I want to thank Professors Mark Asta, Ali Javey, Jie Yao, and Lane Martin for their feedback and guidance during my qualifying exam and dissertation writing processes.

Over the last five years many researchers helped me execute experiments and brainstorm interpretations, and taught me concepts that I could not grasp on my own. First, I want to thank Dr. Doug Detert for being an amazing officemate and friend during my first three years in graduate school. I learned so much from the invaluable advice that he gave me and all the hours he helped me to get my project off the ground. I also want to thank the various Dubón and Solar Energy Materials Group past and present members who helped me including Maribel Jaquez, Dr. Jose Fonseca-Vega, Edy Cardona, Dr. Matt Beres, Min Ting, Dr. Alex Luce, Dr. Paul Rogge, Dr. Weiwei Gao, Dr. Natalie Segercrantz, and Dr. Petra Specht. An enormous thank you also goes to my international collaborators, Dr. Guibin Chen, Dr. Mimoza Ristova, Dr. Juan F. Sánchez Royo, Dr. Sepher K.V. Farahani, and Professor Chris F. McConville, who pushed the progress of my projects forward with their insight and experimental contributions. The feedback and education that I gained from each of them

were extremely helpful. Thank you Jeff Beeman for helping me with my ion irradiation experiments and for your words of wisdom that I will take with me into my policy career. Many thanks to Andre Anders and Joe Wallig for assisting me with my RBS measurements and for maintaining such a priceless machine despite the headaches associated with it. As well, I want to thank everyone who helped me prepare for my qualifying exam in 2015. I also want to thank Dr. Jonathan Solomon for being such a great friend. Your help not only in MSE 201, but also during my qualifying exam preparation and general advice was incredibly helpful. I want to also thank all my close friends who at times had more faith in me than myself and kept me sane when things looked murky.

I also want to acknowledge the funding sources that I needed to complete this work. This work was supported by the Director, Office of Science, Office of Basic Energy Sciences, Materials Sciences and Engineering Division, of the U.S. Department of Energy under Contract No. DE-AC02-05-CH11231 and carried out at Lawrence Berkeley National Laboratory. I would like to acknowledge support through the UC Berkeley Chancellor's Fellowship for the first two years and the National Science Foundation's Graduate Research Fellowship Program for my final three years of my Ph. D program.

Finally, and most importantly, I want to thank my family. My parents Pennilope Brijlall and Anthony Francis supported me during my entire academic career. Mom and Dad instilled in me the value of having an education from an early age. They also made me aware of the power and responsibility that comes for obtaining an education. I cannot thank them enough for the support throughout my entire life and for making the sacrifices you did to raise me. No question about it--I truly wouldn't have made it this far without their support. The headaches were worth it! I want to thank my sister Tresha Francis-Ward, for being a second mother to me, for pushing me through tough times, and for keeping me honest when it looked like I could slip through the cracks. I want to thank my significant other, Tiffany Tu, for changing me and for being an incredible pillar of support as I went through the last five years. She supported me in whatever decision, endeavor, or challenge I wanted to undertake. She helped me think about other perspectives and dared me to be a better person. And, her family was a great support system these last five years. Without Tiffany being there by my side, I'm not sure that I could have withstood the difficult times.

This was a true team effort. Many thanks everyone!

Table of Contents

Table of Figures

Table of Data

Chapter 1
Bandgap engineering, defects, and metal-oxides

1.1 Bandgap engineering

Bandgap engineering is an essential concept in semiconductor science and technology. Its origins trace to the 1950s when semiconductor heterojunction designs to improve device performance. On record, the 1951 Shockley transistor patent is the first documented use of this concept [1]. Six years later, researchers such as Kroener more concretely proposed the use of bandgap engineering to develop a "compositionally graded semiconductor" with electrical properties, such as mobility, and optical properties, such as the optical bandgap, that vary with the semiconductor's stoichiometry [2]. He believed that with bandgap engineering lasing action could occur at lower current densities through carrier confinement in a heterojunction between low and high gap materials [3]. This scheme would, as a result, evoke higher population inversion. He would later produce an AlGaAs/GaAs heterojunction to prove the feasibility of his concept [4-5]. Today, we define bandgap engineering as the “tailoring of the bandgap...to achieve new material and device properties." Overall it has been, and continues to be, critical to the multi-decade development, adoption, and performance of materials for optoelectronics [6]. Alongside the maturation of epitaxial growth methods, this concept is important for light emitting diodes (LEDs) and lasers as well as many other devices and applications. Classically, bandgap engineering studies use materials with tunable lattice constants and bandgaps. **Figure 1** shows the classic diagram for well-known materials, and the materials studied in this dissertation. This concept has since evolved; currently, bandgap engineering studies also incorporate other intrinsic properties such as electrical type, electronic structure, and crystal structure.

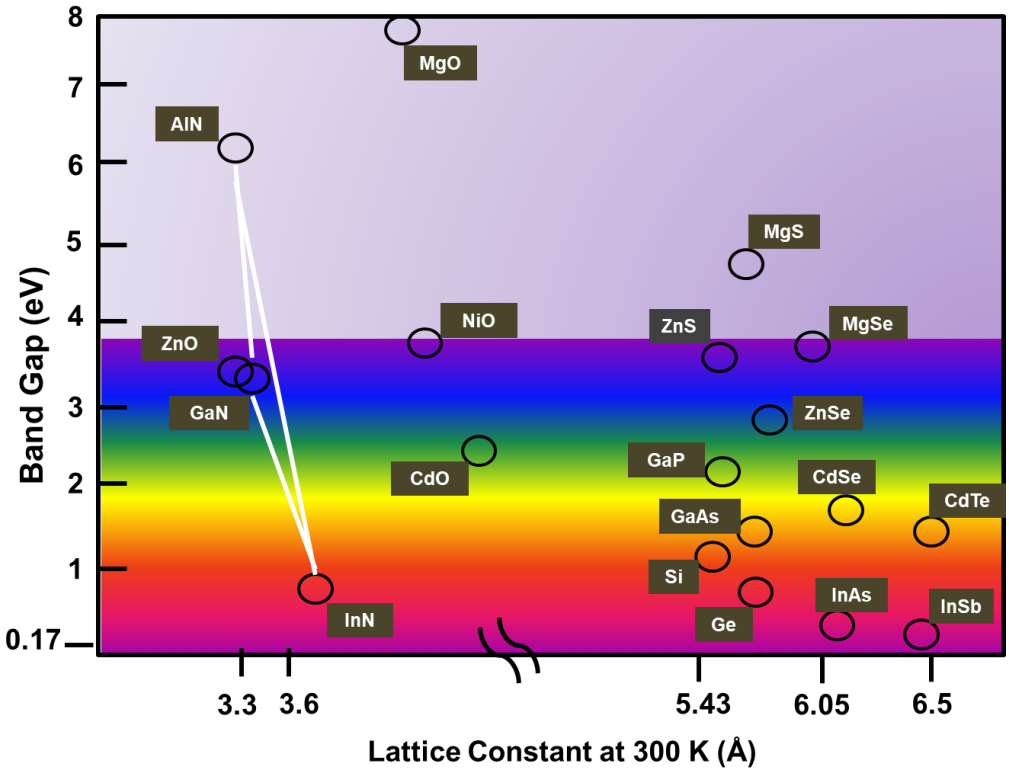

Figure 1: Bandgap versus lattice constant for Group IV, Group III-V, Group II-VI, and metal-oxide materials that are candidates for bandgap engineering studies. Adapted from Reference [7].

Since the 1950s an array of methods has been used to engineer a material's bandgap such as quantum confinement, strain engineering, and alloying. Quantum confinement uses the classical particle-in-a-box concept, in which a material produces discrete energy levels upon the reduction of that material's dimension. Thickness and depth govern the spacing between these levels [8-9]. The development of molecular beam epitaxy paved the way for the capitalization of quantum confinement through quantum wells, which stack materials of different energy levels for improved recombination in LEDs and lasers [10]. Quantum confinement is also exploited in devices based on quantum dots, which are zero-dimensional structures. Quantum dots are important for biolabeling applications. The CdSe quantum dot is a well-known example of bandgap tuning achieved through size reduction. Its tunable photoemission energy varies from 2.0 to 2.7 eV with lower dot diameter from 2.4 to 0.9 nm [11]. Quantum confinement also paved the way for superlattice-based technologies. Superlattices are formed through the strategic combination of materials with different band edge alignment. These materials are important for far-infrared detectors and tunneling applications [12].

Strain is another way to engineer a material's bandgap. The material's band edges, and therefore bandgap, changes in response to the deformation potential. As a result, changes to the material's electrical transport and optical properties occur.

Alloying, the method central to this dissertation research, typically involves the creation of solid solutions with two or more materials to optimize key properties that each constituent material lacks on its own. Limiting the discussion to ternary alloys, we can

discuss the linear bandgap dependence of an alloy, $A_xB_{1-x}D$, based on constituent endpoint compounds AD and BD, on its composition through the quadratic formula [13-16]:

$$E_g(A_xB_{1-x}D) = A(x) + B(1-x) - Cx(1-x)\,, \quad (1)$$

in which AD and BD represent the binary endpoint compounds, x is the composition, and C is the bowing parameter. The bowing parameter indicates the deviation from linearity. Studies, such as those discussed in Section 1.2, indicate that this parameter should be negative. Conceptually, a negative bowing parameter indicates that the bandgap across the composition range is deviating from the linear interpolation of the bandgap for the two endpoint compounds called the virtual crystal approximation (VCA). This VCA replaces the atomic potential of a cation (anion) of one endpoint compound with a weighted average from two cations (anions). Physically, the negative bowing parameter represents the disorder stemming from the inclusion of multiple cations [13-14]. Currently, we have a very deep understanding of how alloying impacts materials' properties principally in studies of the III-V compound semiconductors.

1.2 The state of research on alloys

The III-V system currently serves as the foundation for many of the optoelectronic applications and devices that exist today. This family of semiconductors is diverse in a range of properties including, but not limited to, lattice constants, bandgaps, electron effective masses, direct bandgap, photon interactions, band edge offsets, and deformation potentials [13]. Additionally, the growing ease of synthesizing high-quality III-V materials makes this system continuously critical to industry. The performance and characteristics of applications and devices depend heavily on the candidate materials selected during the development process. Therefore, with these constituent materials, researchers can develop a range of applications that take advantage of the flexibility that the III-V system offers.

Investigations have focused on alloys from the III-nitrides, III-arsenide, III-phosphide, and III-antimonide families and the types of applications involving these materials. III-nitride based alloys are attractive because their constituent materials can lead to the tunability of bandgaps from the near infrared (IR) to deep ultraviolet (UV) range. This broad range is critical for multijunction solar cell applications and blue LEDs [17]. Examples of III-nitride alloys include Ga-rich $In_xGa_{1-x}N$ and $Ga_{1-x}Al_xN$, whose energy gaps are tunable in the UV range [18]. The expansion of the $In_xGa_{1-x}N$ gap is the result of investigations on InN, which has a narrow 0.7 eV bandgap [19]. The bandgap of $In_xGa_{1-x}N$ ranges from 0.7 to 3.4 eV and spans the solar spectrum [20]. Other applications that utilize III-nitrides are high power, high speed devices such as high electron mobility transistors [20]. III-arsenide based alloys include AlGaAs, GaInAs, and AlInAs, which are important for transistors, IR lasers, and heterostructure barrier layers respectively [13, 21]. III-phosphides include GaInP, AlGaP, and AlInP and are attractive for quantum well devices such as red diode lasers [22]. III-antimonides include GaInSb, AlInSb, and AlGaSb which are important for photodetectors, mid-IR interband cascade lasers, infrared optoelectronic devices respectively [23-25]. Clearly, there is a large body of work on III-V bandgap engineering studies by alloying. Although our understanding of these systems and their use is thorough, our understanding of other systems such as alloys based on Group-II cations is not as thorough.

Traditionally, studies beyond III-V semiconductors have been limited to direct wide bandgap II-VI materials based on Zn and Cd sulfides, selenides, and tellurides. These materials are believed to be complementary to, or a replacement for, III-V systems, particularly in the light emission in the blue, green, and higher energy ranges. Examples include ZnSe (E_g~ 2.7 eV) for blue-green laser diodes and CdTe (E_g~1.5 eV) for photovoltaic (PV) applications [25-26]. CdSe for biolabeling purposes is also important. The strong absorption characteristics and relative ease of thin film synthesis make these materials attractive replacements for III-V semiconductors. Additionally, this system's defect behavior can cause materials to have similar recombination behaviors to III-V semiconductors [25-27]. Recently, interest in metal-oxide semiconductors based on Group-II cations has re-emerged for transparent conductor applications.

1.3 Metal-oxides for bandgap engineering studies

Metal-oxide semiconductors generate enormous interest because of their potential applicability to optoelectronic devices. Owing to unique combinations of bandgaps, which allows broad transparency, and electronic structure, which makes it able to be doped to relatively high concentrations, metal-oxides are of interest in transparent conducting applications.

Transparent conducting materials are typically defined by their simultaneous low resistivity of $<10^{-3}$ Ω·cm and high transparencies of >80% at the wavelength of interest [28-30]. Transparent conducting oxides (TCOs) are metal-oxide transparent conductors. Industrially relevant examples include the "gold standard" tin-doped indium oxide (ITO), as well as zinc and tin oxide based conducting oxides such as Al- and Ga-doped zinc oxide (AZO and GZO, respectively) [28-32]. One distinguishing feature of these materials is the ability to have strong conductivities through the synthesis of polycrystalline and amorphous films. The electrical transport properties of TCOs take advantage of the electrically active defects formed in such films. As a result, the synthesized films are highly n-type semiconductors. And, due to their band offsets with respect to the average energy of formation of defects—the Fermi stabilization energy (E_{FS})— the formation of native defects or intentionally added impurities, by doping, can increase the electron concentration and makes p-type conductivity difficult to achieve [29]. As a result, TCOs demonstrate electron typically between 10^{19}-10^{21} cm^{-3}, mobilities (μ) typically between 10-50 $cm^2/V{\cdot}s$, and resistivity values between ~10^{-5}-10^{-4} Ω·cm [31, 33]. Furthermore, these materials have bandgaps between 3.3-4.0 eV, relevant for applications requiring visible region transparency.

The combination of these properties makes TCOs a promising component for flat panel displays, architectural windows, and photovoltaics. The materials requirements for these devices tend to vary: architectural windows require materials with high visible transparency and low IR reflectance to enhance the thermal insulating properties of such windows while PV cells require broad spectrum transparency into the IR range [31, 33]. A transparent top-layer material in thin film PV cells, for example, requires a material with high conductivity and transparency from the IR to the UV ranges. In single-junction and multi-junction solar cells with low absorber layers such as Si (1.1 eV) and Ge (0.6 eV), the current charge collecting components are opaque metal busbars, typically Al or Ag, instead of TCOs [29-30]. Due to their low visible transparency and shape, the achievable efficiency

is limited because light to the absorber layer is blocked. One solution would be a TCO as a replacement charge collection component.

On the other hand, integration of TCOs into existing and future optoelectronics faces two significant challenges: finding materials that simultaneously satisfy the conductivity and transparency requirements mentioned, and creating materials that can exhibit both n-type (electron) and p-type (hole) conductivity. Researchers face the challenge of decreasing the resistivity of TCOs while retaining its optical transparency. The transparency of these materials is usually limited to the visible spectrum because in the UV and IR regions of the spectrum, carrier transition events degrade the material's optical activity. In the UV region, the transparency is enhanced by carrier induced Burstein-Moss shifts [34-35]. In the IR region, the transparency is degraded by free carrier absorption and plasma reflection events [36]. This trade-off is responsible for no broad spectrum TCOs, precluding its use in applications requiring long wavelength transparency. **Figure 2** illustrates the result of these trade-offs: that the resistivity of industrially relevant TCOs have stagnated. Consequently, there are few applicable TCOs and an untapped field of oxide based optoelectronics [28].

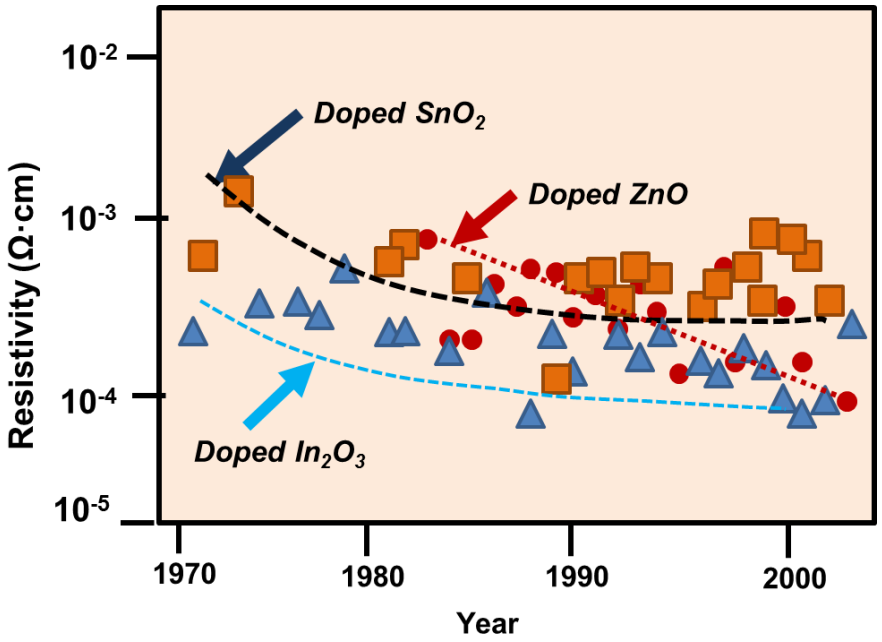

Figure 2: The evolution in studies for TCOs based on doped In, Zn, and Sn oxides. Adapted from References [28 and 37].

Investigating the properties of metal-oxides, and their alloys, is critical to expanding the range of usable materials for transparent electronic devices and applications. And the ability to grow amorphous and polycrystalline metal-oxides without compromising performance is also important. One class of metal-oxides that of importance for TCO applications is the Group-II oxides of ZnO, MgO, and CdO. Proper treatment of this system will be presented in Chapter 2**.** However, it is important to know that studies on these parent materials and its alloys are few in scope, with most of studies on ZnO.

1.4 This dissertation

One Group II-oxide that gained prominence in the past two decades but with few alloying investigations is CdO. This material possesses dynamic electrical transport and optical properties that can be exploited for several desired applications and devices outlined previously. This dissertation extends this interest by correlating the electronic and optical properties of $Ni_xCd_{1-x}O$, a previously unstudied material system, with its electronic structure. Central to this dissertation is bandgap engineering through alloying. Alloying generates thin films with tunable optical and electrical properties over a wide composition range. Without such studies, we cannot determine the feasibility of new materials for devices and applications such as electrochromic windows, water splitting, and thin film photovoltaic applications. In the following sections, the Group II-oxide system and NiO are discussed. However, before undertaking this discussion, we must understand semiconductors within the context of the amphoteric defect model. Only then can we truly understand what makes CdO, NiO, and the $Ni_xCd_{1-x}O$ more unique than other materials.

1.5 Semiconductor point defects

Changes in a material's defect chemistry can bring about consequences, intended or unintended, in a material's optical and electrical properties. The change in a material's defect chemistry can occur through the unintentional introduction of native defects and/or intentional introduction of impurities through doping [32]. Of greatest importance to this dissertation is the alteration of charge carrier densities through native and non-native point defects and surface states.

A point defect is a zero-dimension disruption that breaks bonds and symmetry within a perfect crystal [32, 38]. Native point defects involve the atoms of the crystal as well as missing atoms. There are four types of native point defects: lattice vacancies (a host atom is missing from its intended crystal site), interstitials (a host atom is lodged at tetrahedral or octahedral voids in the crystal), Schottky defects (the formation of both an anionic and cationic defect), and Frenkel defect pair (the formation of a vacancy and interstitial pair) [32, 38]. Extrinsic defects are intentionally introduced atoms that are not native to the system and include substitutional atoms at host atoms and/or interstitial extrinsic effects at non-atomic sites in the "perfect lattice" [32, 38]. Defect complexes that involve combinations of two types of point defects can also occur.

Defects within a semiconductor introduce impurity states in its electronic structure. Deep-level impurities involve strong binding between an electron of the impurity. The orbiting radius of the electron is smaller, which leads to the electron wavefunction not being averaged over a large volume [32]. This is a highly localized level in real space. Shallow-level impurities, conversely, involve the loose binding between an electron of the impurity. The shallow level scheme is typically described by a hydrogen model. The orbiting radius is large and this leads to averaging of the electron wavefunction over a large volume [32]. Both levels have an associated charge state and energy cost, formation energy.

The formation energy of a point defect is related to the charge state of the associated defect. The charge state of the defect and energy of an electron, which is equal to the fermi energy (E_F) influences the formation enthalpy, and concentration of defects. These two factors in turn determine self-compensation events in compound semiconductors [32]. Generally, the term qE_F, where q is the defect charge state (-2, -1, 0, +1, +2 for metal-oxides), is added to the formation enthalpy of a defect [32]. When E_F is low, as in p-type

semiconductors where the defect charge is negative, the formation energy of compensating donor defects is reduced. Conversely when E_F is high, as in n-type semiconductors where the charge state is positive, the formation energy of compensating acceptor defects is reduced [32]. The implication of this self-compensation mechanism is that intrinsic limits exist to the maximum achievable charge carrier density by native and non-native defects.

This self-compensation mechanism is important in industrially relevant semiconductors such as GaAs, Si, Ge, GaP and many others [39-41]. For example, it is relatively easy to dope GaAs p-type to hole concentrations more than 10^{20} cm^{-3} but relatively difficult to n-type beyond electron concentrations of 10^{19} cm^{-3} [39-44]. And certain semiconductors, such as ZnO and InN, demonstrate a strong propensity toward one type of conductivity, n-type, over another. Prior to the 1980's, little research on the physics behind such behavior in semiconductors.

1.6 Amphoteric defect model: native and non-native defects

Until the development of the amphoteric defect model (ADM) by Walukiewicz in the 1980s, the doping limits of materials remained unexplained [41]. Today this model is used to explain the doping limits for not only GaAs, the initial focus of the ADM, but also other compound semiconductors [41]. The ADM was initially created to explain Fermi level pinning behaviors in irradiated group-IV and group III-V semiconductors and non-irradiated versions of the same semiconductors that were made into Schottky barriers [40-42]. For each tested semiconductor, room temperature irradiation of covalent or weakly ionic semiconductors induced alignment of the Fermi level at an energy labeled as the stabilization energy.

For these tested semiconductors, the value at which the Fermi level stabilized in irradiation experiments and pinned in metal-semiconductor junctions with respect to the valence band maximum (VBM) were similar [41]. Moreover, the value of this energy was discovered to be 4.9 eV for all the tested materials. This value physically represents the average hybrid energy of sp^3 bonds or the charge neutrality level for elements and compounds with sufficient covalent character [41]. This result was particularly remarkable because there were two distinct methods of defect introduction—induced surface metal gap states and the intentional point defects.

It was deduced that the stabilization energy was linked to charge neutrality level that Tersoff discovered and labeled as a reference point for metal-induced gap states at metal-semiconductor interfaces [39, 41]. With knowledge of the band offsets and the charge neutrality level, a picture was built—and a prediction of the electrical behavior of the material became easier to make. With time expanded to semiconductors that became more ionic in character, such as II-VI semiconductors and metal-oxides [43].

Because of the ADM, the charge type and maximum achievable electron and hole concentrations for a semiconductor can be predicted. Empirically, this has been confirmed through irradiation experiments. The ADM finds that the doping limitations of a semiconductor are not because of the dopant itself but, instead, are intrinsic to the system. Central to this theory is a common energy level which describes the average energy of formation of defects, called the Fermi stabilization energy (E_{FS}). Both the charge type and doping limits are connected to E_{FS}. **Figures 3 (a)-(d)** illustrate two concepts.

First, Figures 3 (a)-(b) show a hypothetical example: a nominally undoped compound semiconductor, AB, in which A has an oxidation state of 2^+ and B has an

oxidation state of 2, and the band offsets are in positions that result in E_{FS} laying within the mid-bandgap. Figures 3 (c)-(d) show a hypothetical nominally undoped metal-oxide semiconductor, AB, in which A has an oxidation state of 2^+ and B has an oxidation state of 2^- and the band offsets are such that E_{FS} is near the conduction band minimum (CBM) of the semiconductor. In each of these situations, the nominally undoped necessitates the E_F to be positioned near the mid bandgap of each material.

Firstly, there is a universal self-compensation mechanism dependent on the Fermi level location with respect to E_{FS}. The effect of this mechanism is to align E_F with E_{FS}, a condition satisfied when $E_F=E_{FS}$. When the system is in equilibrium, the average formation energy of donor and acceptor compensating defects are equal. The example in Figures 3 (a)-(b) suggests that this semiconductor is in a state of equilibrium and does not demonstrate a propensity to form donors over acceptors and vice versa. When E_F is out of alignment with E_{FS}, there is a driving force for donors (if $E_F<E_{FS}$) and acceptors (if $E_F>E_{FS}$) to form and bring the system to equilibrium. In Figure 3 (c)-(d), the E_{FS} is near the CBM and E_F is therefore lower than E_{FS} ($E_F<E_{FS}$) [42-43]. As a result, this material in Figure 3 (c) demonstrates a propensity to form native donor defects, because the formation energy of these defects is lower than that of an acceptor defect. This example is crucial to industrially relevant metal-oxides because most of these materials strongly favor the formation of donor defects and can easily be made n-type through native or non-native defect introduction.

The second concept central to the ADM is that the band edge location with respect to E_{FS} predicts the ultimate doping limits of a semiconductor. As mentioned above, most metal-oxides demonstrate a propensity to be easily doped n-type because of their low CBM, which situate E_{FS} near or within the metal-oxide's conduction band. This location of the CBM also means that the maximum achievable electron concentration is higher than other semiconductors. For example, In-, Zn-, and Sn-based oxides can be doped between 10^{19}-10^{21} cm^{-3}. It also explains why CdO exhibits, in its nominally undoped form, an electron concentration, n, of 10^{20} cm^{-3}.[1] The intentional doping of a metal-oxide typically involves the aliovalent substitution of the host metal with an impurity metal [28-33, 45]. The intentional introduction of native defects, through irradiation for example, typically involves the formation of favorable thermodynamically defects such as oxygen vacancies [46-48]. As the carrier concentration reaches the previously mentioned threshold concentrations, the average energy of compensating acceptor defects decreases. These compensating defects are readily formed and oppose the creation of donor charge carriers. Therefore, there is an upper limit to the carrier concentration that cannot be surpassed.

Finally, the ADM illustrates why few metal-oxides exhibit p-type electrical transport behavior. Of the industrially relevant metal-oxides, NiO and Cu_2O exhibit the rare propensity towards p-type electrical transport behavior. Their behavior can also be explained with the ADM model. This explanation is shown in **Figures 3(e)-(f).** Overall, the ADM predicts the self-compensating mechanisms for an undoped semiconductor and is also applicable to the intentional addition of dopants.

Semiconductors with ionocovalent character, the group III-nitrides such as InN and GaN, II-VI semiconductors such as CdS and CdTe, and Group II-oxides such as ZnO and CdO can now be understood with the ADM [19, 50-53]. In Group III-nitrides, the analog to the

[1] Chapter 2 discusses the electrical transport properties of CdO.

II-oxide system, it has been shown, using the ADM that the low location of the CBM leads to high n-type doping behavior and difficult to dope with acceptors [19, 43]. Moreover, the large CBM offset between GaN and InN is responsible for the electron concentrations differences: 10^{20} cm^{-3} for GaN and 10^{21} cm^{-3} for InN respectively [19, 53]. This comparison validates the argument that the band edges are instrumental to a material's doping limits. The known band offsets with E_{FS} for a variety of semiconductor systems are shown in Appendix A.

1.7 Amphoteric defect model: surface states

The ADM can also explain surface accumulation effects responsible for relatively high electron concentrations and mobilities in metal-oxides. Disruptions in surfaces within a semiconductor introduce gap states in a similarly to point defects. Typically, high electron concentrations are expected to introduce carrier scattering effects that compromise the electron mobility. These surface states are extended and can be neutral, acceptor-like or donor-like dependent upon the locations of the CBM and VBM [54]. The ADM determines the charge type of these—which is critical for semiconductor thin films in which both bulk and surface contributions impact the materials' overall conductivities [54].

As a response to surface states, the near surface region screens the surface charge, causing an upward or downward bending of the bands. If the surface is positively charged, then the near-surface regions will be negatively charged. On the other hand, if the surface is negatively charged, then the near surface region will be positively charged. This determines whether a material has surface accumulation or surface depletion.

The surface contributions to conductivity can be understood by comparing a conventionally doped semiconductor to a nominally undoped metal-oxide used in TCO applications. In all situations, the ideal condition stabilizes E_F at E_{FS} on surfaces. Consider an n-type Si or GaAs film—where the E_{FS} is lower than E_F [54-58]. Since $E_{FS} < E_F$, there is a contribution of acceptors to the near surface regions. Therefore, the negatively charged acceptor states pin E_F at a position lower than the bulk E_F—and both are pinned lower than the band edges. And, upward band bending occurs with a depleted region of carriers near surface leading to the formation of a positively charged region that neutralizes the negatively charged surface [54].

A different mechanism occurs in most metal-oxides, however, since E_{FS} lies near or within the CBM. There is a high concentration of surface defects, such as dangling bonds, on the surface. As a result, the positively charged donor states pin the E_F. To bring the surface E_F up to E_{FS}, there must be a contribution of donors from the surface to the near surface regions. Donated electrons experience an electrostatic attraction with this positive surface. King *et al.* found with high resolution X-ray photoemission spectroscopy (HR-XPS) on single crystalline In_2O_3 that the surface E_F (~3 eV above VBM) became pinned at a level higher than the bulk E_F (~2.94 eV above VBM). Both levels were higher than the band edges, leading to band bending and electron accumulation [54, 59-60]. In In_2O_3, the surface E_F is pinned at 0.4eV above the CBM. The result is an increase in electron concentration near the material's surface. Similar mechanisms are observed for InN, which has a similar band offset to CdO, and InAs [61-64].

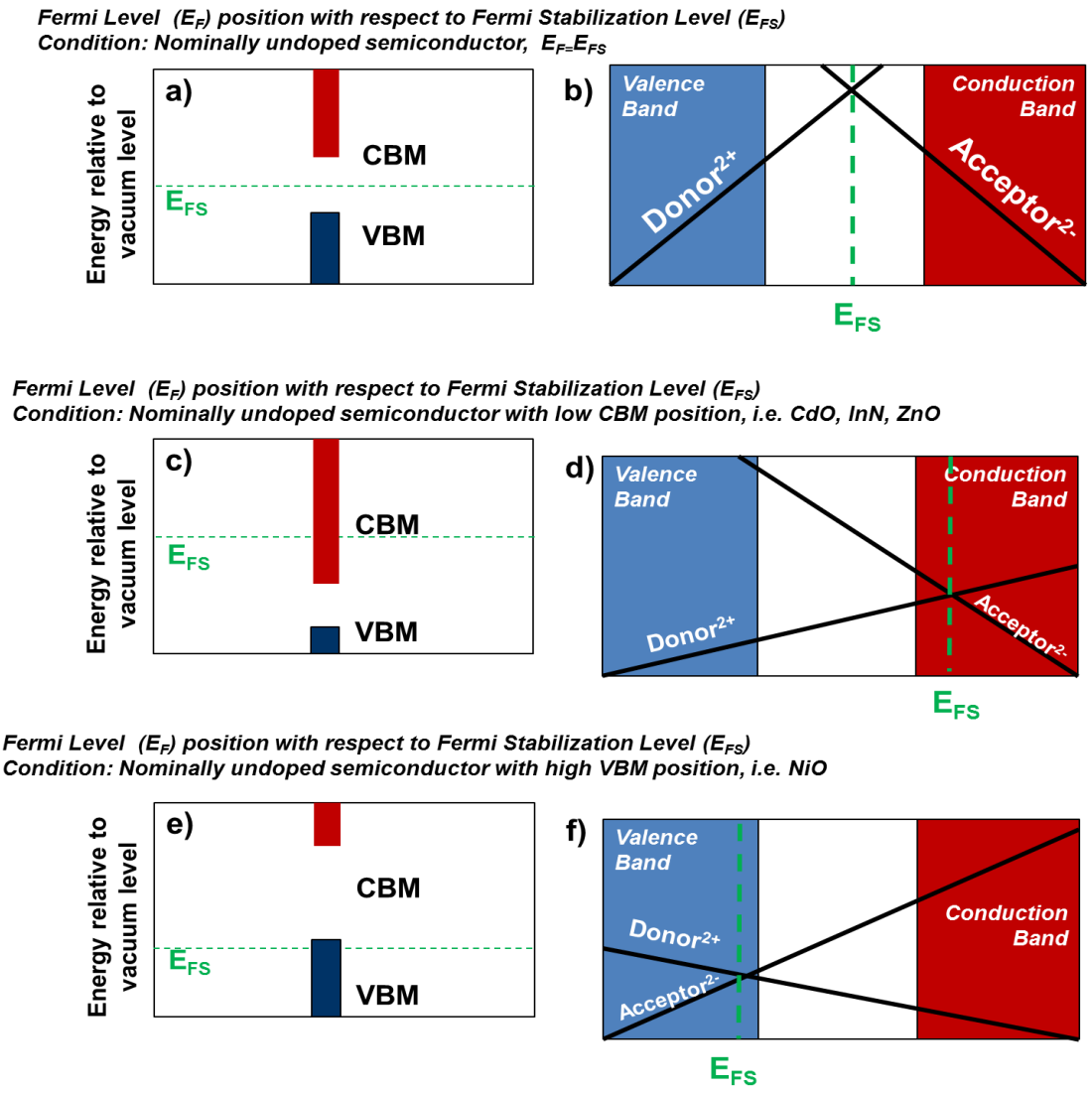

Figure 3: ADM model for (a) nominally undoped semiconductors with band edges that result in the E_{FS} placement within in the material's mid bandgap. As shown in (b), the formation energy of donor and acceptor defects are equal—making neither defect favorable to form. This condition is met when the Fermi level E_F=E_{FS}. The ADM model for nominally undoped semiconductors with a low CBM is shown in (c). This condition leads to E_{FS} being situated near the material's CBM. For these films, the doping limits relative to semiconductors without low CBM are higher. This condition manifests itself in (d) where the formation energy for donor defects is lower than acceptor defects, and E_F can be shifted into the conduction band. This condition explains the high doping limits for ZnO, InN, and CdO as well as the ability to move the E_F into these material's respective conduction bands. For p-type semiconductors, the converse exists and there is a low formation energy of acceptor defects. This condition is reflected in (e) and (f) and, though, a rarity amongst metal-oxides, exists in NiO. Adapted from References [42-44 and 49].

This surface accumulation also causes screening effects that get stronger with increasing electron density. Therefore, fewer collisions occur and higher mobilities are measured. Although the charge carriers' mobilities are higher than typically expected they are usually limited through three main mechanisms upon doping or intentional introduction of defects: acoustic (lattice vibrations), ionized impurity scattering, and grain boundary scattering (which occurs at a threshold carrier concentration). Each of these mechanisms depends on

temperature. The roles of these mechanisms on CdO and $Ni_xCd_{1-x}O$ are discussed in Appendix D. It is important to note that the opposite is true for p-type TCOs—in which upward band bending is favored to downward bending for conventional p-type semiconductors.

The ADM is an essential tool that governs the tunability of a materials' electrical transport and optical properties. The electrical transport properties of a semiconductor are closely linked to its band extrema and are important to a device's design and performance. For example, the band extrema are important for determining the feasibility of a proposed electrical junction, for testing water stability, or for photoelectrochemical schemes—as well as other purposes. These band extrema, relative to the E_{FS}, help predict a system's predominant native defects, identify electrical type (n or p), and quantify doping limits at a given composition. Because of the ADM we can now identify, with better precision, the appropriate candidate materials for bandgap engineering studies based on their band offsets and electrical transport behavior in addition to bandgap and lattice constant. It is this framework that illuminated the promise of the Group II-oxide system, CdO, MgO, and ZnO, for bandgap engineering studies.

Chapter 2
Group II-oxides and NiO

2.1 Overview

Although most oxides are insulting, some metal-oxides have strong semiconducting behavior and gained interest from the electronics community as a result. The Group II-oxide system, of which the principle materials are CdO (E_g~ 2.2 eV, rocksalt), ZnO(E_g~ 3.3 eV, wurtzite), and MgO (E_g~ 7.8 eV, rocksalt), are examples [28-31, 33, 38, 43-48, 65, 66-77]. These three materials are analogous to the III-nitrides (AlN-GaN-InN) and are the basis for next generation oxide-based devices [73]. **Table 1** is a comparison of the intrinsic structural, electrical transport, and optical properties for these oxides and demonstrates plausibility for engineering studies by alloying [73-77].

Historically, ZnO garnered the most interest of the II-oxides. ZnO is the analogue to GaN because of their similar bandgaps (3.3 eV for ZnO to 3.4 eV for GaN at 300K), crystal structures (wurtzite at ambient conditions), and a-axis lattice parameters (3.21 Å for ZnO versus 3.19 Å for GaN [49, 69, 78-80]. The comparatively higher exciton binding energy for ZnO (60 meV) to GaN (20.4 meV) opens the door to replace GaN in UV/blue LEDs and lasing devices [69, 81-84].

The crystallization of ZnO, MgO, and CdO into their respective crystal structures is a result of thermodynamic requirements that crystal structures have its cations and anions organized in the most stable and closed packed configuration possible. This configuration obeys Pauling's rules, maximizes electrostatic attraction between cations and anions that are nearest neighbors, minimizes electrostatic repulsion between second nearest neighbors, ensures local charge neutrality, and coordinates a polyhedron of anions around one cation according to the cation-anion size ratio [38]. ZnO has a cation-anion ratio of ~0.40, leading to configurations with a coordination number of 4. In this structure, O^{2-} anions occupy closed-packed sites and Zn^{2+} cations occupy half of the wurtzite structure's voids. Like other TCOs, manipulation of ZnO's defects involves intentional doping or native defects and is critical to the material's electrical performance. Much controversy exists over the source of ZnO's native defects— O vacancies, Zn interstitials, antisites, hydrogen or defect complexes— that act as shallow donors [69, 85-88]. Nevertheless, ZnO's low

CBM (~4.9 eV below vacuum level) with respect to E_{FS} makes it easily doped n-type to concentrations of ~10^{19}-10^{21} cm^{-3} and resistivities of 10^{-4} Ω·cm with Group III elements Al, Ga, and In [49, 69, 74, 89-92]. In combination with its wide bandgap, ZnO's conductivity makes it a candidate for thin film transistors and solar cells [49, 69, 74, 89-92]. However, the system is not without limitations. The material is limited in applications requiring transparency above 3.3 eV, the deep UV range, and is relatively difficult to dope-p-type.

MgO, by contrast, is an extremely wide bandgap material that is like AlN. Because of a cation-anion ratio of ~0.5, MgO crystallizes in the rocksalt crystal structure [38]. In this NaCl-like crystal structure, O^{2-} anions occupy the close packed FCC sites and surround octahedral voids, which are fully occupied by Mg^{2+} cations. Unlike ZnO and CdO, MgO has an unusually high CBM (~0.5-1 eV), and unusually low VBM with respect to the E_{FS} [93]. The location of these band edges are responsible for its highly resistive behavior and large defect formation energies, on order of 7 eV, for acceptor and donor native defects [38]. This resistive behavior is supported by the lack of reports of this material's electrical transport properties. As a result, MgO is not a candidate material for applications requiring strong electrical transport properties. However, owing to its large bandgap of 7.7 eV, MgO is believed to be a complementary material to expand a host material's bandgap [94-95]. For example, MgO is a candidate in the expansion of the ZnO bandgap above 3.3 eV, which is useful for deep UV applications.[2]

The third Group-II oxide, CdO, is an intriguing metal-oxide with renewed interest over the last two decades. Like MgO, CdO crystallizes in the rocksalt structure— a result of its cation-anion ratio of ~0.7 [38]. And similarly, to InN, CdO has a low CBM of ~6.0 eV below the vacuum level [49, 52, 73-74, 96]. This low location situates the E_{FS} ~1 eV above the CBM and causes easy n-type doping. Moreover, CdO's band offset enables higher doping limits than most semiconductor systems. Strong surface electron accumulation effects, like those in InN, occur in CdO because of its band edges.[3] Unlike MgO and ZnO, CdO has two reported bandgaps— a 1.1 eV indirect bandgap due to its unique electronic structure and a 2.2 eV direct bandgap upon consideration of carrier-filling effects [49, 52, 74-75, 96-100].[4]

The native defect behavior in CdO is due to ability to control oxygen vacancies, which act as double donor defects [47, 49, 96-100]. The predominant defect condition for native defect formation in CdO is given in Kröger-Vink notation by:

$$O_O^x \rightarrow \frac{1}{2}O_2 + V_{\ddot{O}} + 2e' \quad . \tag{2}$$

Under oxygen deficient processing conditions, this defect behavior results in measurable electron concentrations of ~10^{20} cm^{-3}. Typically, we anticipate high concentrations to result in impurity scattering, one of the main scattering mechanisms for metal-oxides, between carriers and a low carrier mobility. By contrast, CdO's high nominally undoped mobility, on order of 100 $cm^2/V{\cdot}s$ at 10^{20} cm^{-3}, arises from its high static dielectric constant compared to other metal-oxides, ~21. CdO can thus effectively screen ionized impurities [98, 101]. Furthermore, these nominally undoped properties can be enhanced with Group-III cation

---

[2] Studies that investigate this potential are detailed in Section 2.2.1.

[3] As explained in Section 1.7.

[4] Please note: The 1.1 eV indirect gap previously reported by theoretical calculations has not been confirmed for thin film CdO.

donors such as Ga or In [98-99, 102-103]. Yu *et al.* demonstrated significant increases in electron concentration (up to 10^{21} cm^{-3}), increases in mobility (up to 200 $cm^2/V{\cdot}s$ at concentrations of 10^{20} cm^{-3}), and improvements in IR transparency (down to 0.8 eV) with In and Ga. These reported properties render enhanced CdO systems to be potential replacements for industrially relevant AZO [99]. Other doping agents used to enhance CdO's properties were Y, F, Sc, and Sn— which yielded resistivities as low as 10^{-4} $\Omega{\cdot}cm$ [104-107].

The implementation of CdO into devices depends on its low bandgap, high IR transparency, and high conductivity. This rich combination makes CdO a potential transparent grid material in multijunction and Si PV technologies [99]. Overall, among known metal-oxides, CdO has the highest mobility (over 200 $cm^2/V{\cdot}s$ for doped electron concentrations up to 10^{21} cm^{-3}), high conductivity (>10^5 S/cm), and high transparency, >85%, for photon wavelengths up to 1500 nm [102-104]. However, the small intrinsic direct bandgap of CdO limits its transparency to short wavelengths with a maximum achievable E_g of 3.2 eV for Y- and In-doped CdO, when heavily doped to electron concentrations > 10^{21} cm^{-3} [99, 104]. The transparency limit thus remains too low for potential UV and deep UV applications. Still, there remains interest in bandgap engineering of CdO by alloying to capitalize on its intrinsic properties.

The implications of potential bandgap engineering studies are potentially impactful for optoelectronics—which require its component materials to have tailored electrical and optical properties. For example, one could maintain the high conductivity of CdO and increase its bandgap through alloying to create an ideal transparent conductor for application in full spectrum photovoltaics [49, 74-75]. A review of literature, however, shows that few bandgap engineering via alloying studies exist for CdO.

2.2.1 Group II-oxide bandgap engineering by alloying: previous literature

Most researchers used ZnO as the host material in bandgap engineering studies. Moreover, the case studies that investigated CdO alloys focused primarily on MgO and ZnO as the complimentary agent.

Table 1: Comparison of the optical, structural, and electrical transport properties of CdO, ZnO, and MgO.

	Metal-oxides		
Material property	***ZnO***	***MgO***	***CdO***
Direct Bandgap, E_g (eV)	~3.3	~7.8	~2.2
Crystal Structure, ambient conditions	Wurtzite	Rocksalt	Rocksalt
***a- axis Lattice Parameter* (Å)**	3.21	4.22	4.70
***c- axis Lattice Parameter (*Å)**	5.20	--	--
Electron concentration, n, nominally undoped (cm^{-3})	~$3x10^{19}$	--	~$2x10^{20}$
Electron mobility, μ, nominally undoped ($cm^2/V{\cdot}s$)	~10	--	~100

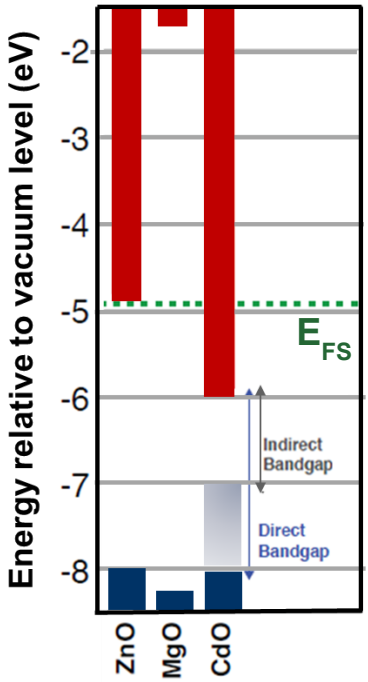

Figure 4: Band offset diagrams for the Group II-oxides developed from experimental information. Note that the electrical transport properties of these systems are governed by the location of each material's band edges with respect to the Fermi stabilization energy. Adapted from References [41-43, 49, 52, 69, 73-74, 93, and 96].

2.2.2 $Zn_xMg_{1-x}O$ alloys

Researchers want to exploit the bandgap and high exciton binding energy of ZnO for potential p-n junctions, superlattice barriers, and/or blue LED active layers. Previous bandgap engineering studies by alloying employed MgO and CdO as complimentary agents for alloying [69, 70]. MgO is used as a compliment to ZnO due to the potential a tunable bandgap from 3.3 eV to 7.7 eV—rendering this alloy suitable for electron confinement in quantum wells [68, 71, 108-112]. Ohtomo *et al.* reported the ability to widen the bandgap up to 3.89 eV through pulsed laser deposition (PLD) for up to 33% Mg in films [108]. Matsumoto *et al.* then demonstrated the ability to dope ZnO to increase the bandgap to 3.7 eV via laser molecular beam epitaxy but with only 20% Mg [109]. Subsequent and recent findings by Makino, Laumer, Maemoto on epitaxial $Mg_xZn_{1-x}O$ films showed a similar trend to Ohtomo's and Matsumoto's films. The bandgap enhancement up to 3.8 eV was also supported by first principle calculations [71] .

Limitations existed in each of these studies. A phase transition from wurtzite to rocksalt, confirmed via X-ray diffraction (XRD), at around 33% Mg for $Mg_xZn_{1-x}O$ alloys was observed; this outcome was due to solubility limits between the endpoint compounds. An attempt to address this limitation was reported by Choopun *et al.*, who observed a metastable cubic phase and bandgap up to 5.0 eV for PLD grown thin films with up to 50% Mg [113]. An additional limitation, given the insulating behavior of MgO, was that these studies failed to induce p-type conductivity. Recent studies by Wei *et al.*, Li *et al.*, and Shan *et al.*, however, demonstrate p-type electrical transport behavior is possible, leaving promise in this relatively unreported research topic [114-116]. Nevertheless, the studies that have realized p-type $Mg_xZn_{1-x}O$ are few in nature.

2.2.3 $Cd_xZn_{1-x}O$ alloys

A larger number of studies on ZnO-CdO alloys exist. The motivation behind creating $Cd_xZn_{1-x}O$, unlike $Cd_xMg_{1-x}O$, is to narrow the ZnO bandgap (increase the CdO bandgap) and enable transparency between the IR to visible ranges of 2.2 eV to 3.3 eV. Initially reported in 1996 by Choi *et al.*, the alloy was synthesized on five films spanning the composition range by sol-gel processing. These researchers found that the inclusion of Zn to CdO increased the resistivity from $\sim 10^3$ -10^2 Ω·cm and increased the bandgap from 2.4-3.3 eV [117]. Subsequent studies by Makino *et al.* characterized PLD grown alloys with up to 7% Cd and reported a decreasing bandgap with increasing Cd [71]. The low Cd content compared to initial studies underscored the insolubility issues between ZnO and CdO. Conflicting reports on the system's solubility emerged since that study. While Gruber *et al*. reported large bandgap bowing and attributed this result to the insolubility of metalorganic vapor phase epitaxy (MOVPE) grown alloys in five films spanning the composition range, Virgil *et al.* reported a small bowing parameter and narrowed bandgap from 3.3 to 2.5 eV across the entire composition range [118-119]. A similar shift to Virgil's work was observed by Ma *et al.* for films up to 53% Cd [120]. Wang *et al.* however observed a shift down to 2.9 eV in molecular beam epitaxy (MBE) deposited alloys containing up to 19% Cd [121].

Commonalities exist between these studies. First, the studies failed to reconcile the true bandgap trend of the alloy—indicated by the various bandgap ranges. Second, these studies did not reconcile the structural differences between ZnO and CdO. While some studies did not observe a wurtzite to rocksalt transition in these alloys, other studies noted a transition under Cd-rich conditions [118]. The inability to characterize this change could be attributed to the inability to grow films within potential composition ranges of interest or with non-equilibrium growth techniques. *Ab initio* calculations, which accounted for the differences in crystal structure, predicted a transition at about 95% Cd, also conflicting with experimental findings [122].

The conflicting differences were addressed by Ishihara, who conducted a full spectrum structure and optical characterization of $Cd_xZn_{1-x}O$ alloys. In this study metalorganic chemical vapor deposition (MOCVD) grown films were grown in increments of 10-15% Cd. This study observed, via XRD, a phase transition from wurtzite to rocksalt and a shift in PL behavior from 3.3 eV to 1.8 eV up to 69% Cd [123]. But this study faced also had limitations. Specifically, explanations of the PL shift, the electrical transport properties, and the electronic structure evolution of these alloys across the entire composition range, were not reported. These limitations also plagued previous studies.

A seminal study that reconciled the previous studies' issues was reported by Detert *et al*. In this study, the electronic and optical properties of cathodic arc deposited $Cd_xZn_{1-x}O$ films were correlated with its electronic structure [74]. Owing to the difference in structure for the two endpoint compounds, CdO and ZnO, the alloy was split into two regimes representing the wurtzite and rocksalt regions. A transition between these phases was reported around 31% Zn content. Measurable electron concentration and mobility across the composition range was correlated with this phase transition. From the rocksalt region to wurtzite region, up to 31% Zn, the electron concentration decreased from 2 x10^{20} cm^{-3} to 10^{19} cm^{-3} and the mobility abruptly decreased from 90 $cm^2/V{\cdot}s$ to 30 $m^2/V{\cdot}s$. Between 31% Zn and Cd, the mobility drops further to 15 $m^2/V{\cdot}s$ [49, 74]. Additionally, optical reflectance and transmittance measurements showed a shift in the absorption edge (E_{AE})

from 2.6 eV to 3.3 eV with Zn. The values in the Cd-rich region were affected by carrier filling effects like Burstein-Moss carrier shifts, and carrier correlation effects. When accounted for they resulted in a bandgap shift from 2.2 to 3.3 eV. Finally, the PL measurements supported those of Ishihara and demonstrated a shift from 1.79 eV at 31% Zn to 3.27 at ZnO [74].

A follow up study correlated these results with the electronic structure evolution of the alloys and attributed that electrical transport properties to the changing positions of the alloy's band offsets with added Zn [49, 96]. By changing the positions of the CBM and VBM relative to E_{FS}, then the formation energy for forming oxygen donor defects increased and resulted in the generation of fewer charge carriers.

Despite this new literature, work on $Cd_xZn_{1-x}O$ still has limitations. If MgO or CdO was a complementary agent, then a phase transition from wurtzite to rocksalt occurred and this transition compromised its electrical transport properties. Though the measured properties were maintained over a wider range for Cd-based ZnO alloys, this phase transition poses issues upon application. A further limitation, given the n-type behaviors of both ZnO and CdO, was the inability to induce p-type conductivity—a feature that also plagued MgO-ZnO studies.

2.2.4 $Cd_xMg_{1-x}O$ alloys

The CdO-MgO studies highlighted a potential bandgap tunability from 2.2 to 7.7 eV, a much wider range than ZnO. Unlike ZnO based systems, this system has isostructural compatibility between the endpoint compounds. Nevertheless, this system is heavily compromised in other ways. Only two experimental studies and one theoretical study on $Cd_xMg_{1-x}O$ exist [75, 124-125]. Paliwal *et al.* predicted a lattice constant shift from 4.79 Å to 4.21 Å with increasing Mg [124]. The most comprehensive study characterized the electronic and optical properties of RF magnetron sputtered $Cd_xMg_{1-x}O$ correlated the results with the change in its electronic structure. This $Cd_xMg1_{-x}O$ study by Chen tuned the bandgap of CdO for up to 28% Mg and showed that alloying raises the carrier-free bandgap by up to 400meV [75]. This shift is accompanied by drastic reductions in electron concentration and mobility (2.0×10^{20} cm^{-3} to $\sim 10^{14}$ cm^{-3} and 100 $cm^2/V{\cdot}s$ to and 1 $cm^2/V{\cdot}s$ respectively) with just 10% Mg. This effect was attributed to two causes. First, the large band offset between the MgO and CdO led to a rapid upward shift in the CBM with Mg content—increasing the formation energy to form native donors. The decrease in electron mobility was attributed to alloy disorder scattering. This study also reported poor structural quality in grown films. The XRD patterns for the alloy displayed broadening of the (220) peak with increasing Mg and poor substitution of Mg into Cd sites—both likely to large differences in the atomic radii.

2.2.5 Implications of previous studies

Previous literature shows the limited knowledge of Group II-oxide bandgap engineering studies. Despite the relatively few studies however, useful information can be extracted. CdO, for example, remains a research area rife with potential. And, criteria exist to identify the ideal complimentary agent for alloying studies involving CdO that can exploit on the strong electrical transport properties of CdO.

First, the complimentary material should be isostructural with CdO. Second, it should preserve the electrical transport properties with small alloy compositions. These two criteria are connected. $Cd_xZn_{1-x}O$ alloys spanned the entire composition range but

experienced an abrupt shift in electrical transport behavior due to the phase transition from wurtzite to rocksalt. $Cd_xMg_{1-x}O$ alloys did not span the entire composition range and did not experience a phase transition. But $Cd_xMg_{1-x}O$ alloys experienced a dramatic decrease in electrical transport properties with just 10% Mg. The third criteria, is to offer flexibility in the tunability of the band extrema. This criterion was seen in all previous studies. The complementary material should enable bandgap tunability of CdO from 2.2 eV. A final, very attractive feature is to synthesize alloys that, with composition, changes from n- to p- type and vice versa. An evaluation of these factors led to the selection of NiO, a metal-oxide that itself is popular within the ceramic, perovskite, and TCO communities.

2.3 NiO

The charge carrier type of industrially relevant metal-oxides is an important, unresolved issue. N-type metal-oxides are most commonly used and available than p-type materials, which make use of hole injection because of mobile electrons from donors and [31]. Although p-type materials are highly desirable, these materials are relatively unstable in their measurable conductivity. Some p-type materials have transparencies limited up to 1000 nm and/or high resistivities [126]. It is believed the poor conductivity of p-type metal-oxides stems from the electronegativity difference between oxygen and the metal atom, which causes the oxygen atoms' 2*p* levels to become suppressed at levels lower than the metal atom's orbitals [127-129]. This results in the strong localization of holes around the oxygen atoms, which can only be overcome with a high photon or thermal energy. As a result, their uses as hole injectors are limited. Moreover, devices based on p-n junction schemes are few in amount [127].

Nickel oxide (NiO) is a wide bandgap (~3.6-3.7 eV) semiconductor that crystallizes in the rocksalt crystal structure [126-135] Its measurable p-type electrical transport properties were initially discussed in 1993 by Sato *et al.* In his study, RF magnetron sputtered NiO reported high resistivites of 10^{-1} Ω·cm and hole concentrations of $\sim 10^{19}$ cm^{-3} [130]. Future studies confirmed similar behavior in sputtered NiO films [131-132]. NiO is important for current and future transparent device applications, such as electrochromic displays and chemical sensors [13, 14, 126-135]. The source of conductivity is believed to be O interstitials or Ni vacancies, which are acceptors typically prevalent under O-rich processing conditions [130]. Jang *et al.*, studied point defects in sputtered NiO films under various O and Ar atmospheres. This study correlated the changes in the coordination number as a function of O content with Secondary ion mass spectrometry and Extended X-ray absorption fine structure and concluded that Ni vacancies were the conductivity source [136]. In annealed non-stoichiometric NiO films, it was found that their Ni-O (first nearest neighbor) bond length increased but their Ni-Ni (second nearest neighbor) bond length did not change with annealing temperature. Moreover, the Ni-Ni coordination number increased with annealing temp and the Ni-O coordination number remained constant. This result is significant because under non-stoichiometric environments, a Ni vacancy formation manifests through the bond length reduction between O anions and Ni cations, and changes Ni^{2+} anions to Ni^{3+} [136]. As a result, the ionic radius of the Ni^{3+} cations decreased and the electrostatic attraction between Ni and O ions increased. Their proposed defect mechanism supports early theories of NiO defect formation, which in Kröger-Vink notation, is expressed as:

$$\frac{1}{2}O_2 \rightarrow O_O^x + 2V_{Ni}^{"} + 2Ni_{Ni}^{\cdot}, \quad (3)$$

in which Ni vacancies accommodate the oxygen excess. Oxygen is initially introduced to an oxygen ion site as a neutral atom and gains electrons from two separate Ni ions giving electrons [137]. These two ions are reduced from Ni^{2+} ions to Ni^{3+}. Two Ni vacancies form and give up holes to electronically compensate for this electron donation. This interaction yields an overall final effective charge state of zero.

Aside from this study, few studies reconcile the predominant defect mechanism in this system [127, 138]. From an ADM perspective, the VBM of NiO is near E_{FS}. Therefore, as-grown non-stoichiometric NiO film exhibit a strong propensity towards p-type conductivity, a rarity among metal-oxides [139-142].

2.4 Potential of the $Ni_xCd_{1-x}O$ alloy

The band diagram of CdO and NiO reveals a great flexibility that bandgap engineering studies can exploit. CdO crystallizes in the rocksalt structure and possesses both an indirect (1.1eV) and direct bandgap (2.2 eV). The electronic structure of the CdO VB is well known and studied with various experimental and computational methods [48-49, 52, 96, 143-147]. This electronic structure is the result of hybridization between the shallow core-level Cd 4*d* states and the predominantly O 2*p* VB states, which have different parity and cannot mix at the Γ-point. Instead, repulsive interactions between these Cd and O states occur at the K- and L-points, resulting in an upward shift of the O 2*p* states and formation of two maxima: one at the L-point, and one midway along the ΓK direction. The interaction additionally leads to an indirect bandgap of ~1.1 eV from the VBM at the L-point to the CBM at the Γ-point. The conduction band of CdO obtains its behavior from Cd 5*s* states. And CdO exhibits a strong propensity towards n-type behavior which, as seen through previous studies, can be enhanced through intentional doping or alloying.

NiO, like CdO, is a rocksalt crystal structure and possesses a direct bandgap of 3.6-3.7 eV. Multiple studies on the electronic structure of NiO report a VB structure formed from the hybridization between O 2*p* and Ni 3*d* states. These studies determined the NiO electron affinity, and therefore its CBM, to be at ~1.4-1.5 eV below the vacuum level and its VBM at 5.1 eV below the vacuum level [134, 140-149]. NiO exhibits a strong propensity towards p-type behavior. A comparison between CdO and NiO shows a stark difference between the two compounds' band offsets.

The high NiO VBM and low CdO CBM leads to a type-III band offset where the CdO CBM is located about 1 eV below the NiO VBM. Therefore, an alloy, $Ni_xCd_{1-x}O$, provides the unique opportunity to study the evolution in very large, larger than 3 eV, shifts of the band edges. The possibility of tuning the CBM and VBM of this alloy and its electrical transport and optical properties also exists. Moreover, the bandgap differences give an opportunity to change the optical bandgap from 2.2 eV to 3.7 eV. Finally, there is a potential for switching electrical behavior from n- to p- with composition and stoichiometry—a phenomenon unobserved in metal-oxide alloys. The suitability of NiO as an alloying agent has been supported by recent studies of $Ni_xZn_{1-x}O$ and $Ni_xMg_{1-x}O$ alloys, which investigated these alloys for UV applications [150-155]. However, these studies provided limited commentary of their measured properties. And, until this work, there were no studies of a $Ni_xCd_{1-x}O$ alloy system. This dissertation fills that gap and provides insights into a dynamic

system. The knowledge gained from this dissertation is not only applicable to CdO but also Group II-oxide alloys and metal-oxide based semiconducting alloys with transition metals.

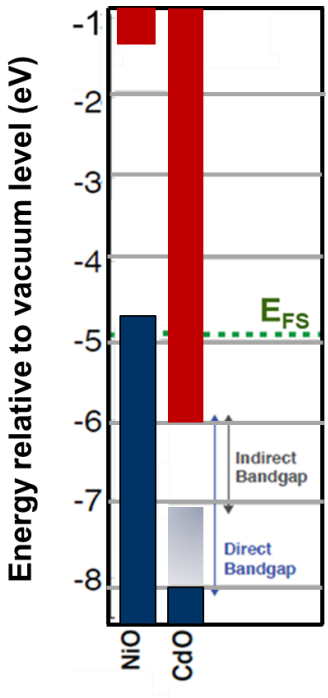

Figure 5: Band offset diagram for the NiO-CdO system. Adapted from References [43, 49, 75, 96, and 140-142].

The guiding questions for this dissertation focused on the ways that specific properties evolved with Ni composition and experiments that could measure this evolution. Examples of guiding questions are, but not limited to, the following:

1. How do the electrical transport, optical, and structural properties change with Ni composition and why do they change?
2. Is p-type conductivity measurable?
3. How do the optical properties change with Ni composition?
4. How does the electronic structure of the alloys change and how is this evolution correlated with the electrical transport and optical properties of the system?

The next chapter describes some of the methods initially employed to answer the above questions.

Chapter 3
Film growth and basic characterization

Before discussing the measured properties of $Ni_xCd_{1-x}O$ alloys in Chapter 4, I will first discuss some methodologies used for this dissertation. Please note that there is no precedent for growing these alloy films.

3.1 Thin film growth: RF magnetron sputtering

Sputtering is a physical vapor deposition technique in which ions from an inert gas, such as Ar, collide with a target known as the source [156]. The system is configured so that a target and a substrate are respectively connected to the cathode and anode. Plasma generation, whereby an ionized gas is created from the interaction between an accelerated stray electron and neutral atom, occurs near the cathode. After plasma creation, high powered gas ions are then accelerated to the target. An elastic collision between the ions and the target occurs with conservation of the energy and momentum transferred from the ions to atoms in the source. The collisions between the ions and target atoms cause a cascade effect [156]. As the cascade effect proceeds, source atoms are energized and collide with other atoms leading to the ejection of atoms, ions, and secondary electrons. Overall, sputtering is a technique in which "what we put in is what we get out," i.e. the desired target composition is the end composition on the substrate. Moreover, large area deposition with high deposition rates and good uniformity are achievable even at low temperatures. Other benefits of sputtering are the ability to have deposition rates of several μm/ minute and operate at lower pressure [156].

The flux and scattering yield affects the arrival of atoms on the surface and therefore impacts the film's composition and thickness. The sputtering rate gives the number of atoms/ second sputtered from the target. The flux and scattering yields are related by the following expression:

$$Q_S = \frac{Y_S I_S}{q}, \quad (4)$$

with Y_S, as the sputtering yield, I_S as the ion current, and q as the charge [157]. The ion current depends on the input power and the applied voltage. The sputtering yield, number of sputtered atoms per incident ion, is determined by the input voltage, power, incident angle of ions, energy of the ions, surface binding energy of the target atoms, and the masses of the target and gas atoms. If there are two atoms, A and B, and $Y_A > Y_B$, then A will be sputtered more than B and the surface of the target will be B-rich for example.

Adatoms are attracted to the substrate surface bond to each other and diffuse over the film surface until the film attains a low energy configuration. From there different processes—shadowing, bulk diffusion, surface diffusion, and desorption—occur and dominate depending on substrate temperature [156]. This combination of factors, in turn, governs the structure and morphology of films.

Temperature is a key processing factor for sputtering thin films. Kinetic and thermodynamic processes, governed by substrate temperature, influence the crystallinity and grain sizes of grown films. Typically, there is a direct relationship between the grain size and the crystallinity. Smaller grain sizes correspond to a polycrystalline film. But with increased temperature, atoms gain enough energy to diffuse across the surface and arrange themselves into larger grains to reduce its energy. On the other hand, at cooler temperatures, an atom has less energy to diffuse across the surface and rearrange itself. Sputtering can be further enhanced through the inclusion of alternating current, direct current, radio frequency, and magnetron components.

Of relevance to this dissertation is RF magnetron sputtering. In RF sputtering, the radio frequency is changed to ensure that the insulating films overcome charge build up. When the voltage is positive in this arrangement, ejected electrons are attracted back to the target and ion bombardment stops. Conversely when the voltage becomes negative, the ions become attracted to the substrate and ion bombardment of the target continues. Plasmas need to be enhanced because the cathode sheath within the chamber is wide and the electron density from ionization is, as a result, low. The magnetron component enhances the plasma. By using Lorentz Forces an electron, ejected upon ion and atom collisions, becomes bent back into the cathode and ionizes a larger amount of the sputtering gas near the target, thus enhancing ionization [156].

The RF magnetron sputtering instrument used for this study contains two guns connected to CdO and NiO targets. By varying the power of each gun, the composition can be varied. **Figure 6** displays photos and a schematic of the homemade RF Magnetron Sputtering configuration. Thin films of nominally undoped $Ni_xCd_{1-x}O$ alloys were grown on glass and sapphire substrates using a dual-gun RF magnetron sputtering system with separate NiO and CdO targets. The chamber was evacuated to $1x10^{-6}$ Torr prior during deposition [100]. The background pressure was maintained at ~5 mTorr of Ar at substrate temperature of 270°C (substrate power of 60%) during sputtering. Films with CdO:NiO ratio ranging from 0 to 1 were deposited by varying the sputtering power and substrate-to-target distance of the CdO and NiO targets. A complete list of the sputtering conditions and films grown for each project within this dissertation are in Appendix B.

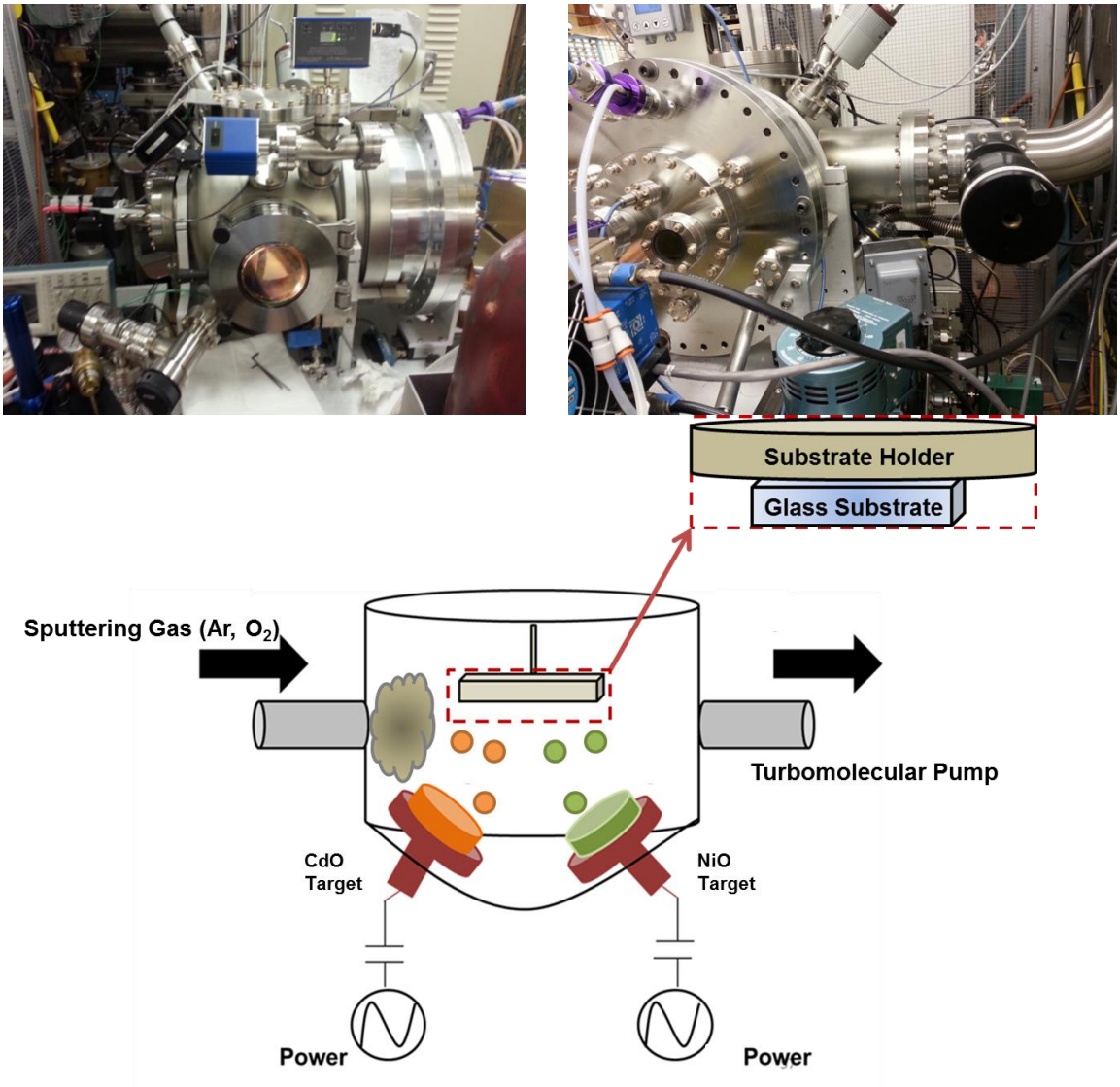

Figure 6: (Top) Pictures of the RF magnetron sputtering setup utilized at Lawrence Berkeley National Laboratory and (Bottom) corresponding schematic of the RF magnetron sputtering processes used to grow films for this dissertation and described in Section 3.1.

Upon thin film growth of $Ni_xCd_{1-x}O$, it was important to maximize the conditions that yield conductive films. Crystallinity was not as much of a concern because native defects within polycrystalline films have been shown to intentional tune the native defect concentration and, as a result, carrier concentration in the films. Furthermore, it has been shown that polycrystalline and monocrystalline CdO films have similar electrical transport properties. This method, compared to others like MOCVD, Cathodic arc deposition, and PLD grows thin films with comparable electron concentrations and mobilities [49, 74-75, 100, 157-158].

3.2 Composition and thickness by Rutherford backscattering spectrometry

After film growth, the stoichiometry and thickness of the films were characterized with Rutherford backscattering spectrometry (RBS) using a He^{++} beam. RBS is a powerful analytical, nondestructive technique for quantitative analysis of a film's thickness and

composition. RBS also determines crystalline perfection in thin films, detects defects in single crystalline films, and identifies impurities amongst other uses. The selection of He is attributed to its ability to resolve the resolution of high projectile masses. A spectrum for each of film containing three identifying features is obtained after firing the He^{++} ions into the substrate. First the kinematic factor, important for mass determination, is obtained from the elastic energy transfer between source ions and target atoms [32]. The detected energy for backscattered alpha particles enables the identification of elements with different masses within both the film and substrate. The ratio of the kinetic energy before and after, E_0 and E_1 respectively, the collision gives insight into the kinematic factor, K, [32, 159]:

$$K_{m_2} = \frac{E_1}{E_0} = \left[\frac{\sqrt{(m_2^2 - m_1^2 sin^2\theta)} + m_1 cos\theta}{(m_2 + m_1)}\right]^2 = K(\theta, m_2, m_1). \quad (5)$$

This equation gives us information about the mass of the targets' constituents, m_2, after being brought into contact with the source ion that has a mass m_1.

Second, the inelastic energy loss of an ion traversing through a target is important for the determination of target thickness [32]. This energy loss occurs when the ions interact with either the electrons in the film or the nuclei of target atoms. Glancing collisions between a source ion, the nucleus of the element, and the electron cloud of the element occur. Since atomic nuclei are small, ion-nucleus interactions are neglected and the energy loss due to electron- ion interactions governs the energy loss. This change in energy corresponds with the thickness of the film. With the K, E_0, and E_1 calculated in Equation 5 and film thickness, t, the total energy loss, ΔE, and therefore the depth scale, can be determined by using the equation [32, 159]:

$$\Delta E = \left(\frac{K}{cos\theta_1} \cdot \frac{dE}{dx}|_{E_0} + \frac{1}{cos\theta_2} \cdot \frac{dE}{dx}|_{KE_0}\right) \cdot t\ . \quad (6)$$

The information calculated is displayed in the spectra's peak width, allowing for film thickness determination [160-161].

Third, the scattering cross-section, captures the probability of an elastic collision between a source ion and target atom and governs the film composition [32]. After interacting with the target atom the number of backscattered ions at an initial characteristic energy backscattered at an angle, with respect to the detector, must be determined. The number of backscattered particles, A, is calculated using the equation:

$$A = \sigma \Omega N_S Q, \quad (7)$$

in which σ is the average scattering cross-section, Ω is the detector solid angle, N_S is the atom/ cm^2 for the target, and Q is the total number of incident particles [159]. It is important to note the direct relationship between N_s and A. Larger amounts of target atoms results in larger backscattering yields. Because of this relationship, the backscattering

yield, Y, can be approximated with the atomic number of the target atoms, Z_2, and source ion, Z_1 with initial energy E_0, using the equation [32, 159]:

$$Y \propto \left(\frac{Z_1 Z_2}{E_0}\right)^2. \quad (8)$$

The height of the obtained spectra signifies the number of backscattered particles detected at a given energy and enables chemical composition determination.

The detection of low mass impurities in high mass substrates is limited when energies that cause pure Rutherford scattering events are used however [162]. Therefore, during investigations of thin oxide films, an energy of ~3.04 MeV, corresponding to the ^{16}O-resonance as calibrated by an impurity-free SiO_2, is typically chosen [162]. The high energy results in larger non-Rutherford scattering cross sections than pure Rutherford scattering and better mass resolution as a result [162]. For $Ni_xCd_{1-x}O$, an energy corresponding to the ^{16}O -resonance was used for detection of low mass impurities.

Analyses of the thickness and composition for each film were executed with a SIMNRA simulation of the obtained spectra.[5] The thicknesses of the films ranged from 100 to 200 nm and the alloys were grown across the composition range within an error of ±1% Ni.

3.3 Structural, electrical transport, and optical characterization

XRD with Cu K_α radiation probed the crystal structure of $Ni_xCd_{1-x}O$ films. XRD employs a monochromatic beam of X-rays, typically from a Cu K_α source, to interact with the target material. The material-X-ray beam interaction leads to scattering of the beam, emblematic of constructive interactions and diffraction [85, 163, 164]. This interaction is characterized by Bragg's law:

$$n\lambda = 2d \sin\theta, \quad (9)$$

in which n is a whole number that indicated constructive interference, λ is the incoming x-ray wavelength, θ is the angle of incidence and reflection, and d is the distance between planes [32] The output from this detected interaction is peak intensity versus 2θ XRD pattern that contains peaks at given angles. These peaks correspond to the position of planes within the crystal. From this information, users identify the crystal structure of the target material. The phase identification, phase separation analysis, and lattice constant determination across the composition range were performed. A determination of deviation from Vegard's law was also performed, as was the grain size and preferred orientation determination [164]. The selection of XRD helps determine the isostructural nature of grown alloys across the composition range—one of the criterion established by Section 2.2.5.

[5] An example of SIMNRA simulations used to determine film thickness and composition is given in Appendix C.

Electrical transport properties including concentration, resistivity, and mobility were obtained by room temperature Hall effect and resistivity measurements in the Van der Pauw configuration with magnetic fields of 0.6 and 1T at room temperature of 300K. Briefly, consider a material containing a density of electrons *n*. Upon application of an electric field, in the x-axis, the electrons move will move. But a magnetic field application perpendicular to this electric field, in the z-direction, will force the electrons to move in response to the magnetic and electric forces. This direction is related to the Lorentz Force [165]. The electrons will bend their trajectory in the –y direction, perpendicular to the two forces and collect on one side of the film. A measurable voltage drop known as the Hall voltage is induced in the y-direction. Therefore, with a current, I, and magnetic field, B, the charge of a free carrier q, and Hall voltage V_H, the sheet concentration, n_s, of the film can be calculated using [165]:

$$V_H = \frac{IB}{qn_s} \ . \tag{10}$$

From this quantity, the bulk concentration can be calculated by using the equation [165]:

$$n = \frac{n_s}{d}, \tag{11}$$

in which d is the thickness of the film. The resistivity of a material is not a material property because different materials can have the same resistivity. The measured resistivity of a material varies due to film processing method. Calculating the sheet resistance overcomes any differences. This method, called the van der Pauw technique, takes an arbitrarily shaped film and uses ohmic contacts to determine the resistances at two terminals [166]. Measurement of these properties is essential for measuring changes in electrical transport properties with Ni composition.

The optical properties, particularly the absorption edge (E_{AE}), were determined with optical absorption spectroscopy (OAS) over a photon wavelength range of 250–2500 nm.[6] Optical photospectrometers can handle photons of micro eV and higher and provide a non-destructive method to measure a material's fundamental optical parameters such as transmittance (T), reflectance (R) [32, 36, 167]. For an absorption event to occur, a photon must have sufficient energy ($h\nu > E_g$) to generate an electron-hole pair and promote that electron from an occupied VB state to an unoccupied CB state. There must be an available final state for such a transition to occur. The energy and momentum of an absorbed photon are conserved and the transition from initial to final state of an electron provides information on the density of available states, occupation probability for available states, and possible transitions [36, 167] Absorption is typically evaluated in terms of the absorption coefficient, α, which in turn is described by:

---

[6] Note: Differences in nomenclature for the absorption edge (E_{AE}) and bandgap (E_g) exist. The distinction between the two energy gaps is important in films with high carrier concentrations, approximately 10^{16} cm^{-3} and greater. Chapter 4 explains this distinction with greater detail.

$$\frac{I}{I_O} = \exp(-\alpha x), \quad (12)$$

in which I_0 is the intensity of the incident light, I is the intensity of light that has exited through the film without being scattered, and x is the thickness [36, 167]. It is important to note that the ratio of I/I_0 is the material's transmittance. And if the total intensity, I, of transmitted, reflected, and absorbed light is assumed to be equal to the incident intensity, $I_0=1$, then one can determine α from T and R [36]. Using R(E) and T(E), in conjunction with Beer's Law of absorption, α as a function of energy was determined. Therefore, equation 12 can be rewritten as:

$$T(E) = (1 - R(E)) \exp(-\alpha x) \ . \quad (12.1)$$

By rearranging equation 12.1 into:

$$\alpha(E) = -\left(\frac{1}{d}\right) \ln\left(\frac{T(E)}{1-R(E)}\right), \quad (12.2)$$

the α as a function of energy is then calculated. Using these values, an energy dependent α plot for each film is then created. Typically, α is sensitive to transitions, indirect and direct, from filled VB to unfilled CB states. Then a linear fit of α^2 versus energy plots are performed to extrapolate the E_{AE}. This method was used for $Ni_xCd_{1-x}O$ films. This measurement was essential for determining and explaining the change in optical properties with Ni composition.

Next, the results obtained with the techniques and an analysis of these results are reported in Chapter 4.

Chapter 4
Electrical, optical, and structural characterization of $Ni_xCd_{1-x}O$ alloys

As previously described in Section 2.4, the high location of the VBM of NiO results in an extreme band offset between CdO and NiO in which the CdO CBM located at 1 eV below the NiO VBM. The band offset schematics for the CdO-NiO material system were shown in Figure 5. The $Ni_xCd_{1-x}O$ alloy system provides a unique opportunity to study the evolution in the electrical and optical properties of a material system with very large, > 3 eV, shifts of its band edges. Initially, synthesized $Ni_xCd_{1-x}O$ alloys over the entire composition range were grown and their structural, electrical and optical properties were measured.

4.1 Structural characterization by X-ray diffraction

Figures 7 (a)-(c) and 8 (a)-(b) show an XRD analysis of $Ni_xCd_{1-x}O$ films across the composition range. They show that all films are polycrystalline with random grain orientations and an average grain size of ~16 nm.[7] Figures 7(a)-(b) shows that the (220) peak monotonically shifts to higher 2θ angles (~55°-62°) with increasing Ni content. The patterns in Figures 7(a) and (c) indicate a reduction in the lattice parameter of the alloy as the Ni content increases, consistent with the smaller lattice parameter of NiO (a_{NiO}=4.209Å, a_{CdO}=4.719 Å). Using these endpoint parameters, the amount of substitutional Ni^{2+} ions at Cd^{2+} sites in $Ni_xCd_{1-x}O$ were calculated with Vegard's law for random alloys.

The calculated lattice constant values are presented as a function of Ni composition in Figure 8(a). Figure 8(b) compares the calculated substitutional Ni content by XRD and total measured Ni content by RBS. The dashed line indicates that all Ni atoms in the alloy are substitutional. The compositions obtained from XRD and RBS are in general agreement. The slightly lower Ni content

[7] An analysis of the films' grain size and correlation with carrier scattering is in Appendix D.

measured by XRD, especially for alloys in the range of 20-80% Ni may originate from the effects of stress and/or defects such as Ni interstitials, or clusters.

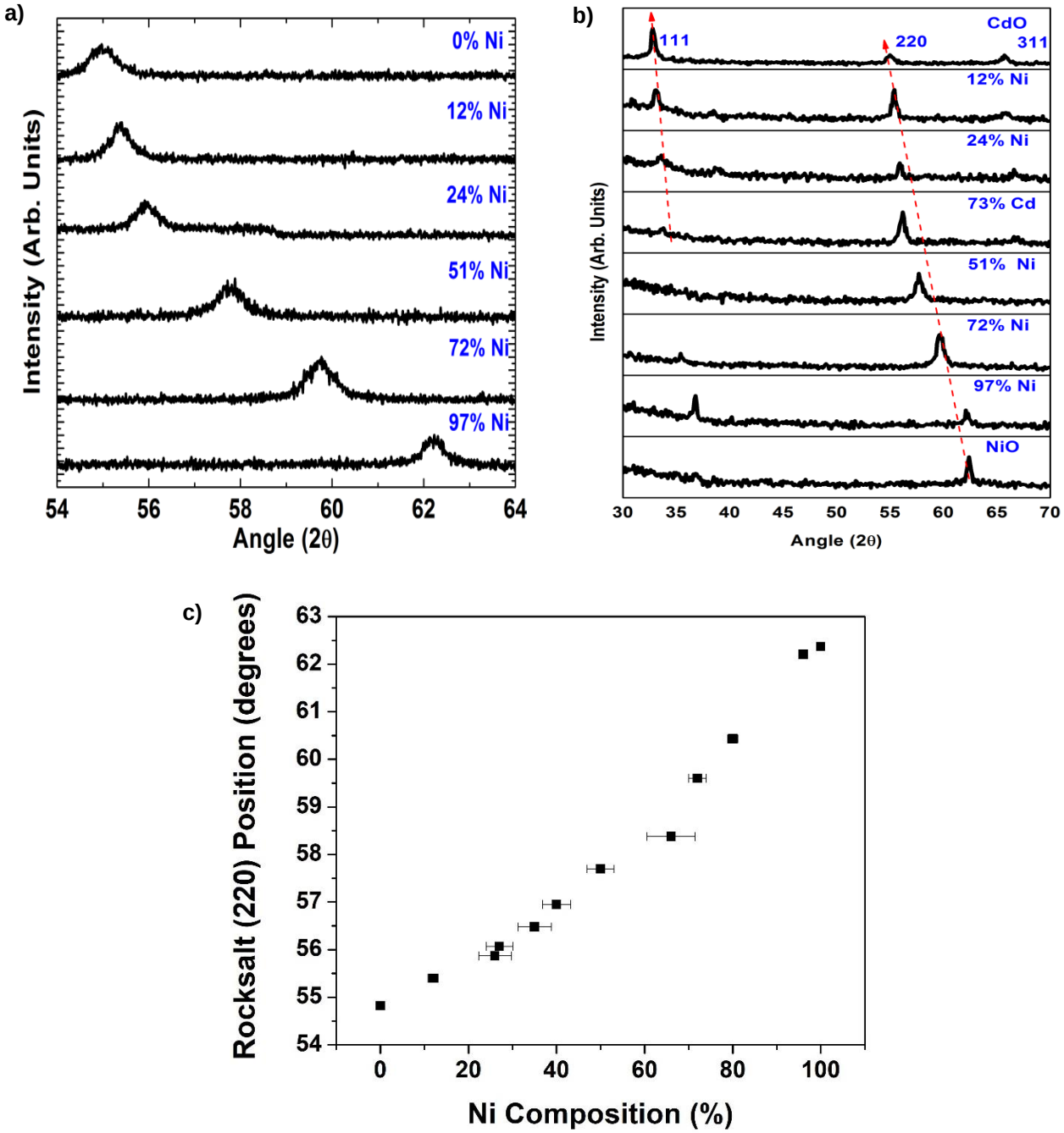

Figure 7: (a) (220) XRD peaks of $Ni_xCd_{1-x}O$ films with increasing Ni content, (b) XRD peaks across the composition and 2θ ranges for $Ni_xCd_{1-x}O$ films and (c) the rocksalt (220) position for all films analyzed by XRD.

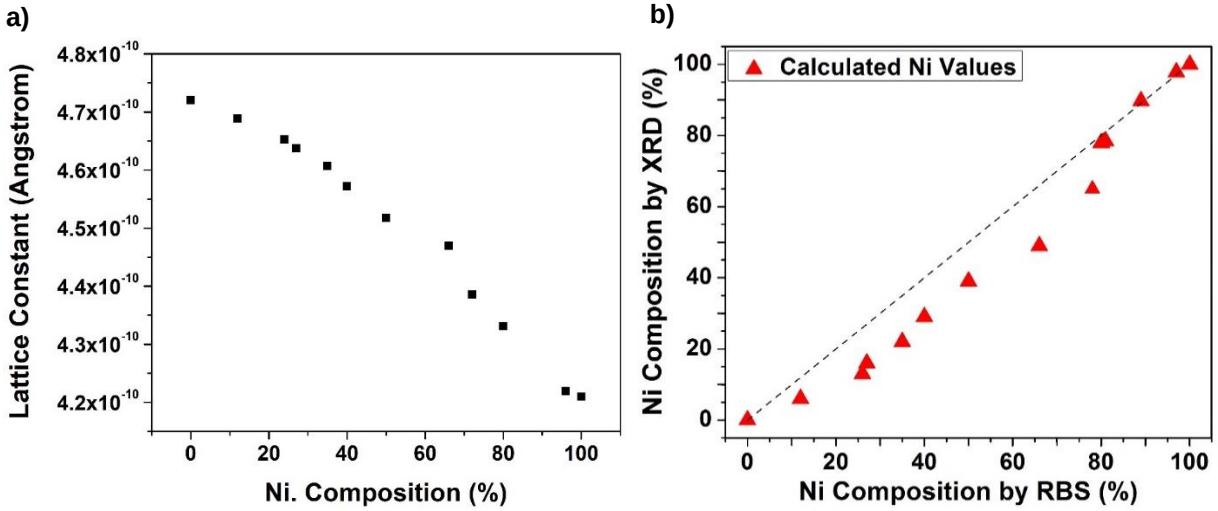

Figure 8: (a)The determined lattice constant as calculated with Vegard's law which shows a change from 4.72 to 4.20 Å and (b)the dependence of the substitutional Ni composition determined by XRD as a function of the total Ni content measured by RBS. The dashed line shows 1 to 1 relationship.

4.2 Electrical transport characterization via Hall effect

Figure 9 and **Table 2** summarizes the measured electrical properties of the alloys.

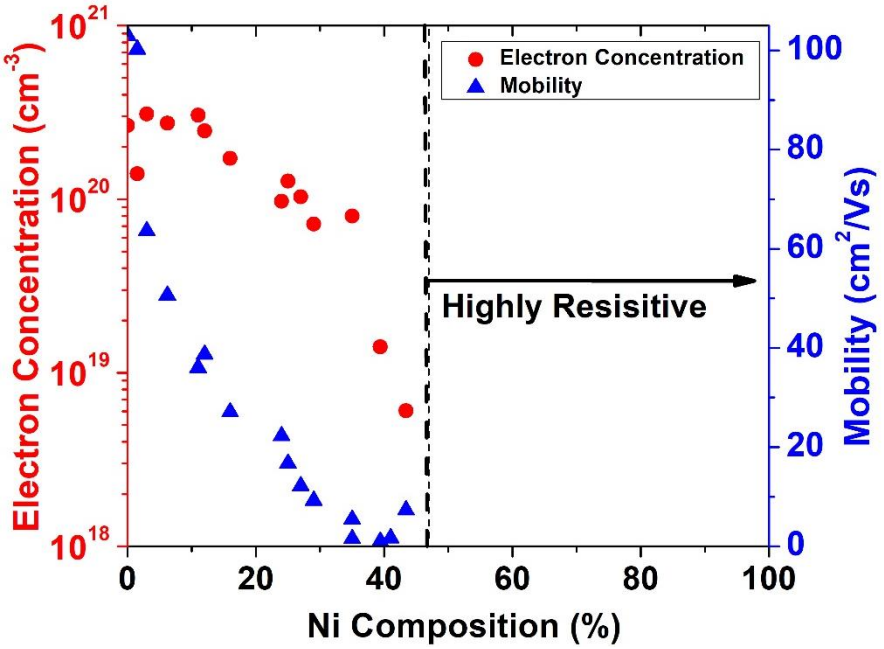

Figure 9: Room temperature electron concentration and electron mobility of Ni_x-$Cd_{1-x}O$ films as a function of Ni content. Highly resistive behavior was observed for films with x>43.4% Ni.

Table 2: Summary of as-grown electrical transport properties for Ar sputtered $Ni_xCd_{1-x}O$ films.

Ni Composition (%)	*Electron concentration, n (cm^{-3})*	*Electron mobility, μ ($cm^2/V{\cdot}s$)*	*Resistivity, ρ (Ω-cm)*
97	--	--	--
90	--	--	--
80.8	--	--	--
72	--	--	--
58	--	--	--
51	--	--	--
41	$3.54x10^{17}$	1.6	10.99
43.4	$6.04x10^{18}$	7.3	0.143
39.4	$1.41x10^{19}$	0.99	0.444
35	$4.18x10^{19}$	5.4	0.028
35	$8.00x10^{19}$	1.5	0.053
29	$7.19x10^{19}$	9.2	0.010
27	$1.03x10^{20}$	12.2	0.001
24	$9.73x10^{19}$	22.3	0.003
24	$1.27x10^{20}$	16.7	0.003
16	$1.72x10^{20}$	27.1	0.002
12	$2.48x10^{20}$	38.7	$1.72\ x10^{-4}$
11	$3.05x10^{20}$	36.0	$7.57\ x10^{-4}$
6.2	$2.74x10^{20}$	50.6	$1.18\ x10^{-4}$
3	$3.09x10^{20}$	63.6	$4.80\ x10^{-4}$
1.5	$1.40x10^{20}$	100.2	$4.44\ x10^{-4}$
0	$2.66x10^{20}$	103	$2.78\ x10^{-4}$

The Cd-rich alloys are n-type and increase resistivity with added Ni. The films become insulating (resistivity ρ >1000 Ω·cm) for Ni content greater than 43.4% Ni. Both the electron concentration (red circles) and mobility (blue triangles) decrease rapidly from n ~$2.7x10^{20}$ cm^{-3} and μ=103 $cm^2/V{\cdot}s$ at CdO to n~ $6.0x10^{18}$ cm^{-3} and μ~ 1 $cm^2/V{\cdot}s$ at 43.4% Ni respectively. The decrease in electron concentration with increasing Ni content can be understood by the large conduction band offset of ~4.4 eV between CdO and NiO as previously shown in Figure 5. As the NiO content increases in the alloy, the CBM shifts from ~5.8 eV in CdO to ~1.4 eV below the vacuum level [43, 49, 75, 96, 140-142]. Assuming a linear dependence of the band edges on the alloy composition, the CBM is expected to cross the E_{FS}, which is located at 4.9 eV below the vacuum level, of approximately 20% Ni. This upward shift of the CBM reduces the propensity of the material for n-type doping. As the CBM moves towards E_{FS}, the formation energy of donor- and acceptor-like native defects becomes similar, leading to significant compensation and reduction of the electron concentration and mobility.

4.3 Optical characterization via absorption measurements

Figures 10-12 summarizes the optical properties of the alloys. The optical absorption coefficient, α, for these alloys was calculated using the measured reflectance and transmission spectra and the Beer-Lambert law as described in Section 3.3. The result is plotted for select films in **Figure 10 (a)**. The E_{AE} was then obtained through a linear extrapolation of the α^2 plots to the baseline. These α^2 versus energy plots are shown in

Figure 10 (b). The extrapolated E_{AE}, as shown **Figure 11**, increases with increasing Ni content from 2.6 eV at CdO to 3.63 eV at NiO.

It is also important to note that the thicknesses of the films range from ~100-250 nm. Therefore a large α, of the order of 10^4-10^6 cm^{-1}, can only be measured. On the other hand, any indirect bandgap absorption manifested as typical α of two orders of magnitude smaller ~10^3 cm^{-1} are not seen. There are many materials, such as GaAsP, AlGaAs, GaInP with a crossover from indirect to direct gap without any observed effects on the direct band gap.

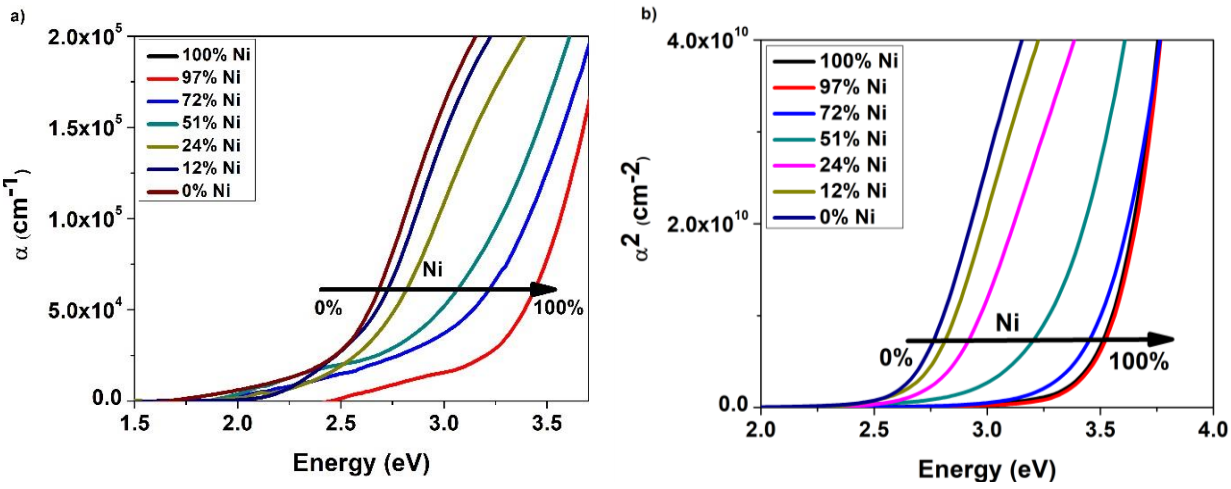

Figure 10: (a) The optical absorption coefficients, α, and (b) the squared optical absorption coefficients, α^2, as a function of photon energy in $Ni_xCd_{1-x}O$ for selected films across the composition range.

4.3.1 Optical characterization via absorption measurements: Carrier Filling effects in $Ni_xCd_{1-x}O$

Extrapolation of **Figure 10 (b)** to the energy axis provides an indication of the material's E_{AE}. However, a distinction exists between E_{AE} and bandgap (E_g). It would be erroneous to only report the E_{AE} data because those values do not represent intrinsic gaps of the alloys—especially the films containing high Cd compositions. The intrinsic E_g of any highly conducting semiconductor material requires corrections for the carrier filling effects, Burstein-Moss shifts and additional Coulombic interactions, that take place and are pronounced in materials with high carrier concentrations [34-35, 168-170]. Generally, high carrier concentrations cause the material's Fermi level (E_F) to shift into CB (due to electrons) or VB (due to holes) of a semiconductor. Owing to carrier filling in the CB of these alloys, the next available state to be occupied by an excited electron is now shifted and related to the E_g plus an additional energy. Since electrons cannot occupy the same state, in accordance with Pauling's rules, the electron must now occupy the next available state [165]. This state will be located at a state positioned higher than the E_F. This upward shift is called the Burstein-Moss shift [34-35]. It is most impactful is in semiconductors with low carrier effective masses because the resulting high curvature leads to significant rises in E_F when significant carrier concentration increases occur.

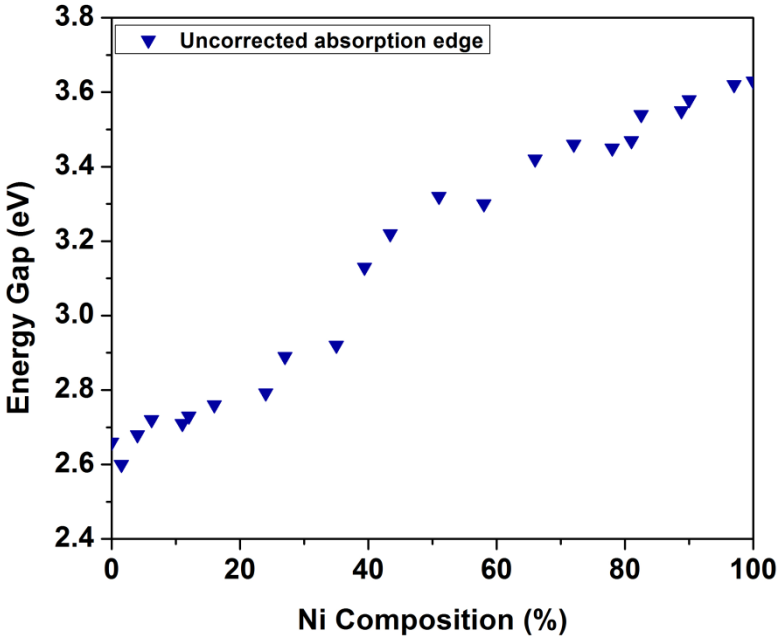

Figure 11: The E_{AE} as a function of Ni composition varies from 2.6 eV (CdO) to 3.6 eV (NiO).

The Burstein-Moss shift is obtained by calculating the energy difference between the E_F and the CBM. This accounting technique is carrier-dependent; with higher concentrations, the energy of the lowest unoccupied state in the CB shifts upward and is no longer at CBM. This is a standard procedure that has been used for many material systems [49, 52, 74, 100, 171-172]. The E_F is related to the electron concentration, $n(E_f)$, by the following expression:

$$n(E_f) = \frac{1}{3\pi^2}\int_0^{\infty} \frac{exp(z-\frac{E_F}{k_{BT}})}{\left[1+exp(\frac{E_F}{k_BT})\right]^2} k^3(z)dz\,, \tag{13}$$

in which $z=E_c/k_BT$. E_c is the electron energy with respect to the conduction band edge [35, 168-170]. The wavevector, k, is determined from a nonparabolic dispersion, derived from Kane's two-band **k·p** model:

$$E_c(k) = \frac{\hbar^2 k^2}{2m_0} - \frac{E_g}{2} + \sqrt{\left(\frac{E_g}{2}\right) + \left(\frac{E_g \hbar^2 k^2}{2m^*_e}\right)}, \tag{14}$$

in which E_g is the intrinsic bandgap and m_e^* is the band edge effective mass [170]. As a first approximation, the electron effective mass for these Cd-rich films was estimated by using the literature value for CdO ($m_e^*=0.21m_0$) [74]. For example, InN, which has a 0.7 eV bandgap and effective mass of about 0.07 m_0 experiences a Burstein-Moss shift of around 0.2 eV [173]. In $Ni_xCd_{1-x}O$, it has been determined that such a shift occurs in films with high carrier concentrations, with an especially pronounced effect in the Cd-rich range. When the carrier concentrations exceed a threshold amount, typically 10^{19} cm^{-3}, there are Columbic

attractions between electrons and positively ionized donors as well as many-body correlation effects.

The bandgap renormalization effects due to electron-electron correlation and electron-ion interactions are calculated using expressions from References [168] and [169] These electron-electron, electron-ion correlation effects work to shift the overall bandgap value downwards. The electron-electron correlation is calculated by the equation [168]:

$$E_{e-e}(n) = -\frac{2e^2 k_F}{\pi_0} - \frac{e^2\lambda}{2\varepsilon_0}\left[1 - \frac{4}{\pi}\tan^{-1}\left(\frac{k_F}{\lambda}\right)\right]. \quad (15)$$

This correlation works to decrease the conduction band energy since the concentration, n is contained in the Fermi wavevector k_F [168]:

$$\lambda = 2\sqrt{\frac{k_F}{\pi a_B}} \text{ and } a_B = a_H\left(\frac{\varepsilon_r}{m_e^*}\right), \quad (16)$$

where a_B is the Bohr radius of the electron.

Columbic interactions between electrons and ionized impurities also decreases the CB energy. This interaction is represented by the equation [168]:

$$E_{e-i}(n) = -\frac{e\hbar}{2}\left[\frac{\pi^3 n}{m_e^* \varepsilon_r}\right]^{\frac{1}{2}}. \quad (17)$$

Like the Burstein-Moss shifts, they are especially significant for films with high carrier concentrations. To determine the intrinsic E_g the method of References [49] and [74] that collectively accounts for the conduction band filling effects as well as electron-electron and electron-ion interactions for highly n-type Cd-rich $Ni_xCd_{1-x}O$ alloys were adopted. [8]Overall, the intrinsic, carrier-free E_g, is expressed as:

$$E_{AE-}E_{BM}(n) + E_{el-el}(n) + E_{el-i}(n) = E_g\,, \quad (18)$$

in which $E_{BM}(n)$ is the Burstein-Moss effect, $E_{el-el}(n)$ and $E_{el-i}(n)$ are energy shifts caused by electron-electron correlation and electron-ion interactions, respectively.

The intrinsic bandgap, E_g, of the alloy thin films calculated using Equation 18 are represented by the red circles in **Figure 12** and shown to increase from 2.2 eV at CdO to 3.63 eV at NiO. Since alloys with greater than 43.4% Ni are highly resistive both the upward and downward shifts are negligible to E_{AE}. As is seen in Figure 12, the E_g of $Ni_{1-x}Cd_xO$ alloys shows unusual composition dependence. Typically, the composition dependence of the bandgap can be expressed in terms of bowing equation:

$$E_g^{Ni_{1-x}Cd_xO}(x) = E_g^{NiO}x + E_g^{CdO}(1-x) - bx(1-x). \quad (19)$$

[8] A Mathematica code that executes Equations 13-18 is attached in Appendix E.

In standard semiconductor alloys, the bowing parameter is negative which is a manifestation of the repulsive interaction between the CBM and higher conduction bands as well as between the VBM and the lower valence bands. However, fitting of the composition dependence of the bandgap gives a positive bowing parameter b=1.26. This behavior may be attributed to a repulsive interaction between the unoccupied, extended conduction band states and the occupied, acceptor-like *d*-levels of Ni located at about 6.1 eV below the vacuum level or 0.2 eV below the CBM of CdO [174]. The occupied localized *d*-levels do not contribute to the optical absorption plots seen in Figures 9-10, but they affect the location of the unoccupied CB states that are ultimately responsible for the extrapolated optical E_{AE} values. The mixing of the extended CB states with highly localized *d*-states could be also responsible for the drastic reduction of the electron mobility with increasing Ni content for Cd-rich alloys. An initial study of the absorption behaviors of select compositions with larger thicknesses yielded no absorption from these *d*-levels. Confirmation of this model, specifically the origin and the effects on the materials properties of the unusual positive bowing of the E_g, requires further investigation which is performed and reported in Chapter 5.

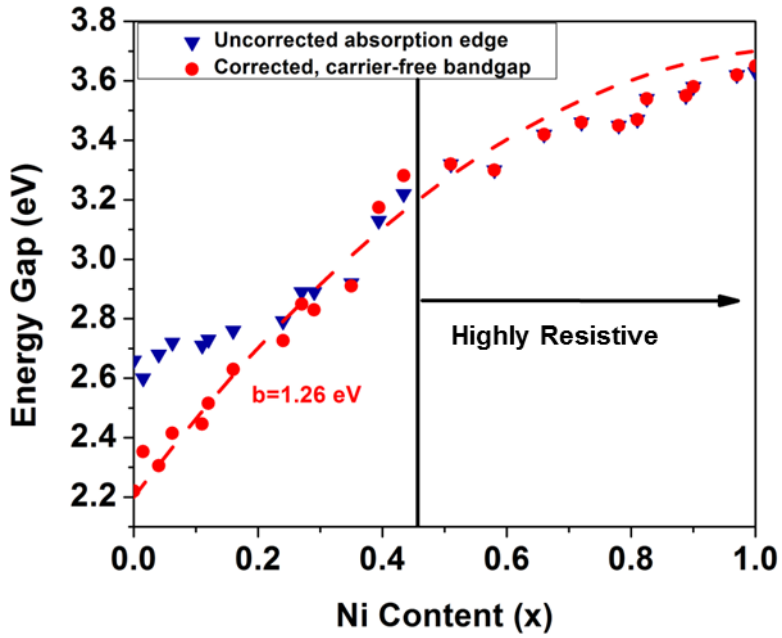

Figure 12: The uncorrected optical absorption edge (blue triangles) and the intrinsic bandgap (red circles) corrected for the free electron effects determined using equation 18 and fitted with equation 19.

In this chapter, the structural, optical and electrical properties of $Ni_xCd_{1-x}O$ alloys synthesized by radio frequency magnetron co-sputtering were reported. Cd-rich alloys exhibit a rapid decrease in electron mobility from 103 $cm^2/V{\cdot}s$ to 7 $cm^2/V{\cdot}s$ and electron concentration (from $2.7x10^{20}$ cm^{-3} to $6.x10^{18}$ cm^{-3}) with increasing Ni content up to 43.4%. The decreases in electron concentration and mobility are consistent with the movement of the CBM from below to above E_{FS} with increasing Ni content. The direct intrinsic E_g of the alloys can be tuned continuously from 2.2 eV (CdO) to 3.63 eV (NiO) with increasing Ni. The observed unusual composition dependence of the intrinsic bandgap with a positive bowing

parameter is attributed to a repulsive interaction between the conduction band and the localized *d*-states of Ni. The mechanisms behind these results are explored and explained further in Chapter 5.

Chapter 5
Effects of Ni *d*-levels on the electronic structure of $Ni_xCd_{1-x}O$ alloys

The anomalous optical and electrical transport behaviors $Ni_xCd_{1-x}O$ are the basis for this chapter. The electron concentration and mobility respectively decreases rapidly from ~$2.7x10^{20}$ cm^{-3} and 103 $cm^2/V{\cdot}s$ for CdO to $6.0x10^{18}$ cm^{-3} and 1 $cm^2/V{\cdot}s$ for 43.4% Ni. A super linear bowing behavior occurs for the measured bandgap. The addition of Ni, a transition metal with partially filled *d*-orbitals to CdO leads to localized donor-like and acceptor-like states near its band edges. Correlations between these states and the measured properties exist. And, the underlying physics behind these behaviors should be investigated. The electronic structure evolution is probed with Band Anticrossing (BAC) modeling, ion irradiation, and X-ray Photoelectron Spectroscopy-Ultraviolet Photoelectron Spectroscopy (XPS-UPS) measurements.

5.1 Ion irradiation theory

Native defects are intentionally introduced using high energy particle irradiation with ions. Previous studies have shown that the effects of irradiation on the properties of CdO, InN, $Cd_xZn_{1-x}O$, and ZnO as well as topological insulators such as Bi_2Se_3 and Bi_2Te_3 can be understood in terms of the amphoteric defect model (ADM) [52, 91, 96, 175]. To recap, this model relates the electrical behavior of a material's native point defects to the location of the Fermi level, E_F, relative to the Fermi Stabilization energy, E_{FS}. Thus, donor-like (acceptor-like) native defects are formed for the condition in which $E_F<E_{FS}$ ($E_F>E_{FS}$) [42, 44].

These irradiation studies used a key parameter to track the changes in their materials: the carrier concentration. The concentration indicates extent of state filling by carriers. Assuming a material with a low CBM, the point defects introduction increases its electron concentration. As the concentration increases in the material, CB states are filled and the E_F shifts to higher positions. At high irradiation fluencies, E_F stabilizes at

E_{FS} when the formation energies of donor-like and acceptor-like native defects are equal. The defect-induced stabilization or saturation of the E_F leads to saturation of the electron (hole) concentration and enables the determination of CB (VB) edges relative to the E_{FS}. This is indicated by saturation in concentration (n_{sat}) at a specific value for each film composition—at which, point defect generation does not increase the concentration.

The E_F corresponding to the saturated electron concentration n_{sat} (E_F) condition is then calculated by the following expressions, which resemble the Burstein-Moss filling effects mentioned in Chapter 4:

$$n_{sat}(E_F) = \frac{1}{3\pi^2}\int_0^{\infty} \frac{\exp(z-\frac{E_F}{k_BT})}{\left[1+\exp(\frac{E_F}{k_BT})\right]^2} k^3(z)dz, \quad (20)$$

where $z=E/k_BT$. E is the electron energy with respect to the conduction band edge [34, 35]. Once again, the wavevector, k, is determined from a non-parabolic dispersion, derived from Kane's two-band **k·p** model:

$$E_c(k) = \frac{\hbar^2k^2}{2m_0} - \frac{E_g}{2} + \sqrt{\left(\frac{E_g}{2}\right) + \left(\frac{E_g\hbar^2k^2}{2m^*_e}\right)}, \quad (21)$$

where E_g is the intrinsic bandgap and m_e^* is the band edge effective mass [170]. As a first approximation, the electron effective mass for Cd-rich alloy was assumed to be equal to the band edge electron effective mass of CdO ($m_e^*=0.21m_0$) [49, 74, 97]. Then, the CBM was calculated with E_F under the condition that E_{FS} is always located at 4.9 eV below the vacuum level. **Figure 13** shows a step-by-step graphical representation of the theory behind ion irradiation and the procedure for calculating the film's CBM.

In CdO the ADM predicts the formation energy for donor defects to be low and high electron concentrations to be achievable because its E_{FS} is in the CBM. The high measurable carrier densities for films with up to 43.4% Ni suggests E_{FS} to be at the CBM of $Ni_xCd_{1-x}O$. Therefore, probing the band offsets through irradiation is appropriate. The band offsets of the endpoint compounds NiO and CdO are well understood and studied. However, the band offsets of $Ni_xCd_{1-x}O$ with intermediate amounts of Ni are unknown. The shifts occur for both the CBM and VBM positions with increasing Ni. This upward shift in position is believed to increase the formation energy of donor defects and cause fewer donors to fill the CB. **Figure 14** graphically displays the proposed band offset movement with Ni composition.

The selection of ions and implantation depth were determined by Monte Carlo simulations from the Stopping and Range of Ions in Matter (SRIM) program. SRIM uses the binary collision approximation, which models the interaction for a sequence of binary collisions between an incoming ion and a target atom [176]. The collisions are assumed to neglect interactions between nearest neighbors and the nuclei of atoms. Instead, the ions experience the electronic stopping power of the target's electron cloud. The stopping power refers to the amount of force imposed on the ion to slow the ion after colliding with the material. The traversing ion inelastically scatters with the electron cloud of the atom and loses energy. The amount of collisions with electrons is very large. But a binary collision between one ion and one electron is used to simplify the case.

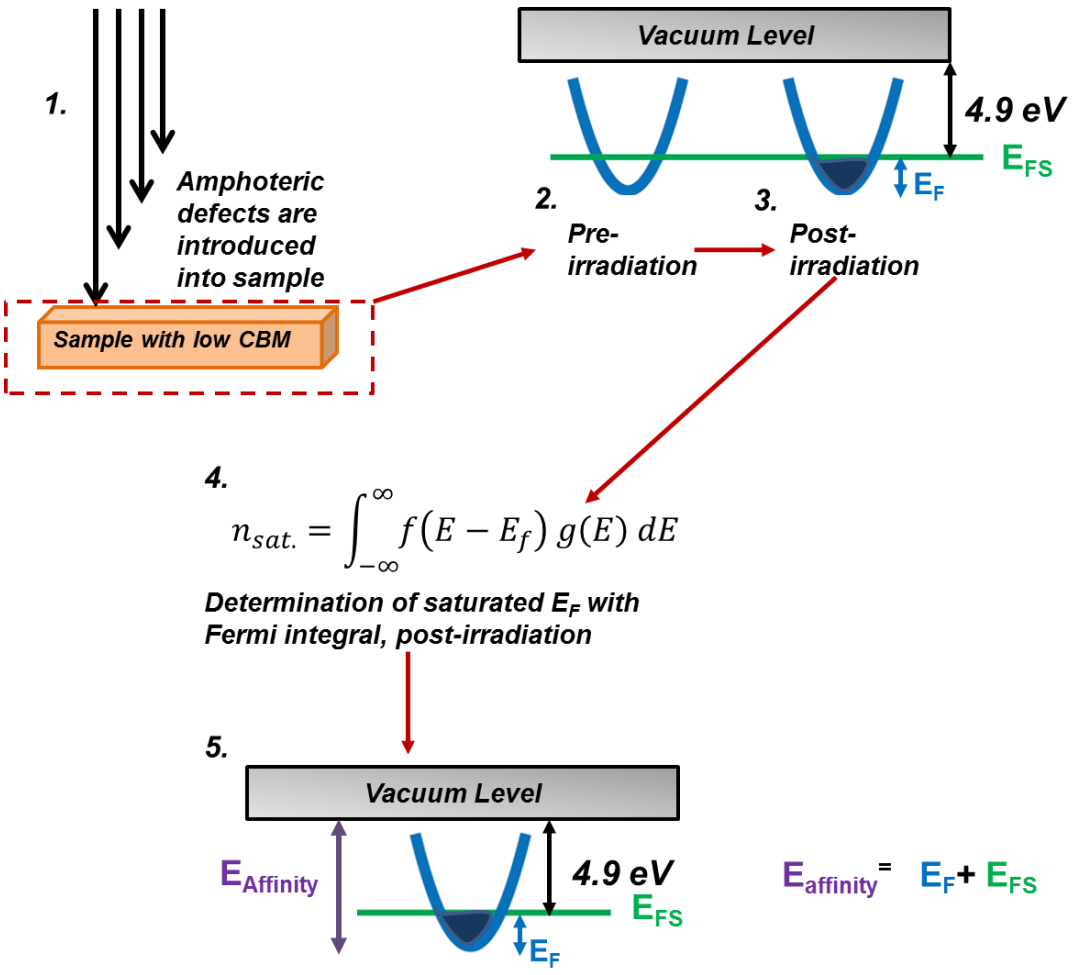

Figure 13: Schematic of native defect generation and band offset determination via ion irradiation. This method is useful for determining the CBM position of materials with low CBM positions such as CdO, InN, and ZnO as well as their alloys. Irradiation is a multi-step procedure. Amphoteric defects, which are typically oxygen vacancies for n-type metal-oxide semiconductors, donate electrons that occupy states within the CB. The change in state filling pre- and post-irradiation are depicted in steps 2 and 3. The filling ceases when a unique saturated electron concentration for the film, n_{sat}, is measured by the Hall effect. At this point, the CB states are filled with carriers and the E_F has been raised into alignment with the E_{FS}. When E_F=E_{FS}, the donor defect formation is no longer favored. With n_{sat}, the condition that E_F=E_{FS}, and knowledge that E_{FS} is located at 4.9 eV below the vacuum level for all semiconductors, the energy between the pinned E_F and the material's CBM can be determined using the integral in step 4, which calculates the carrier density from a Fermi-Dirac distribution function and the density of states. Finally using E_F and E_{FS} the electron affinity, $E_{Affinity}$,, and consequently the CBM can be determined, shown in step 5.

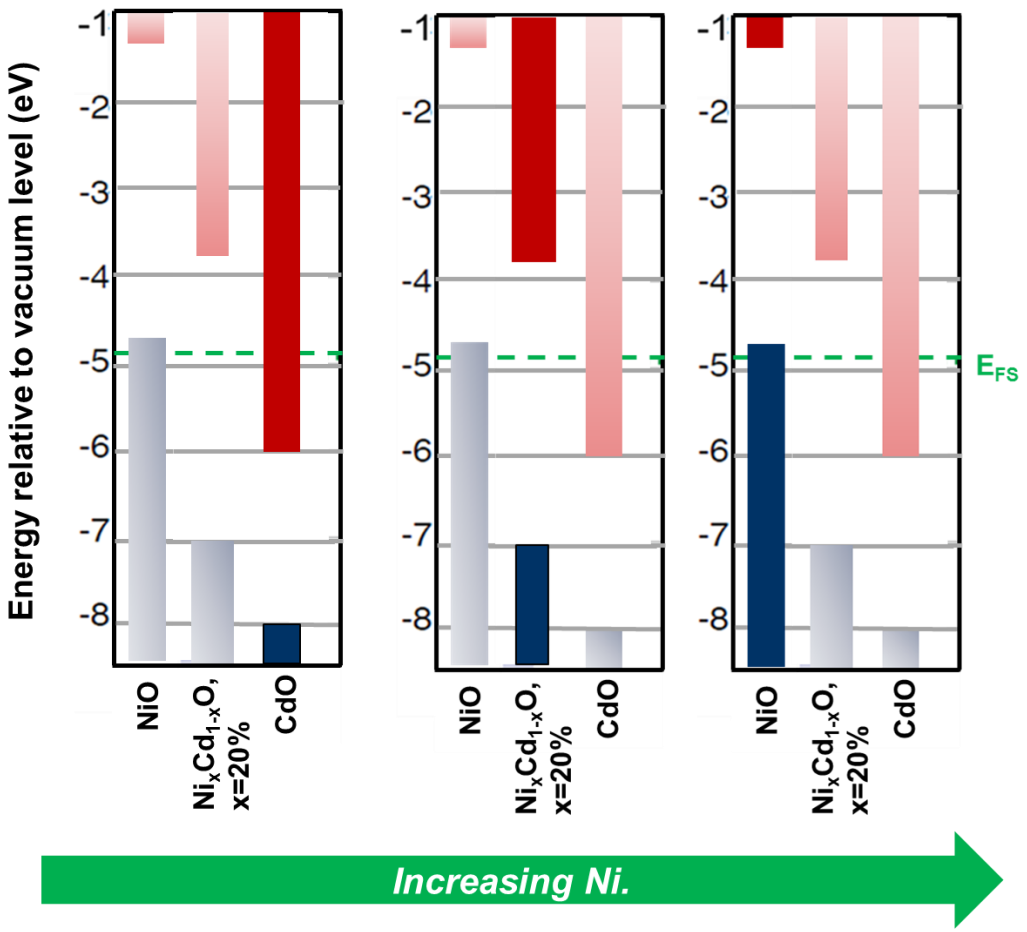

Figure 14: (From left to right), the proposed band offset movements for $Ni_xCd_{1-x}O$. Beginning with the well-known band offsets of CdO (left), the addition of Ni induces an upward shift of both the CBM and VBM. Using the E_g values from Section 4.3.1 as well as interpolated band edge values from a virtual crystal approximation of the endpoint compounds the shifts are supposed to result in the subsequent band offset for $Ni_xCd_{1-x}O$ for x= 20% Ni (middle). The continuous addition of Ni creates drastic, rapid upward shifts of the VBM and CBM, to that of NiO (right).

Previous literature shows that heavier Ne^+ ions are appropriate for intentional defect incorporation in CdO- based films over lighter ions, such as He^+, because Ne^+ creates a larger density of defects and minimizes any self-healing effects that confound measurements [52]. By determining these parameters, uniform point defect generation in the film and the end of range damage occurs in the substrate.[9] If the end of range damage is in the film, then the ions would be implanted—creating unintended consequences and changing the film's microstructure. For $Ni_xCd_{1-x}O$ films, a spatially uniform damage was generated with 150 keV Ne^+ beam introduced in sequential flux increments of $1x10^{13}$ cm^{-2}. The room-temperature electron concentration and mobility were determined by Hall effect after each irradiation cycle until reaching n_{sat}.

[9] Appendix F shows the results of a SRIM simulation performed on a film prior to ion irradiation.

5.2 Ion irradiation results

The electrical transport properties as functions of irradiation fluence are presented in **Figure 15 (a) and 15 (b).** The results in Figure 15 (a) show that the electron concentration increases with increasing irradiation fluence for films with lower than 10% Ni and decreases for films with higher Ni content. On the other hand, as is shown in Figure 15 (b), the mobility decreased with increasing irradiation fluence for the Cd-rich alloys and becomes almost independent of the irradiation for alloys with higher Ni content. Note that both electron concentration and mobility saturate at the highest irradiation fluence of $5x10^{13}$ cm^{-2} are plotted in **Figure 16.** For CdO, the electron concentration saturates at $3.7x10^{20}$ cm^{-3}. This agrees with previous studies of the effects of irradiation on the electrical properties of CdO [49, 52, 96]. However, adding NiO results in a monotonic decrease of the saturated electron concentration to $2.5x10^{16}$ cm^{-3} at 41% Ni content. The observed decrease in the electron mobility with increasing irradiation fluence is attributed to an increase of the scattering from ionized defect centers. **Table 3** summarizes the electrical transport properties measured via Hall effect, E_F and $E_{Affinity}$ for this ion irradiation study.

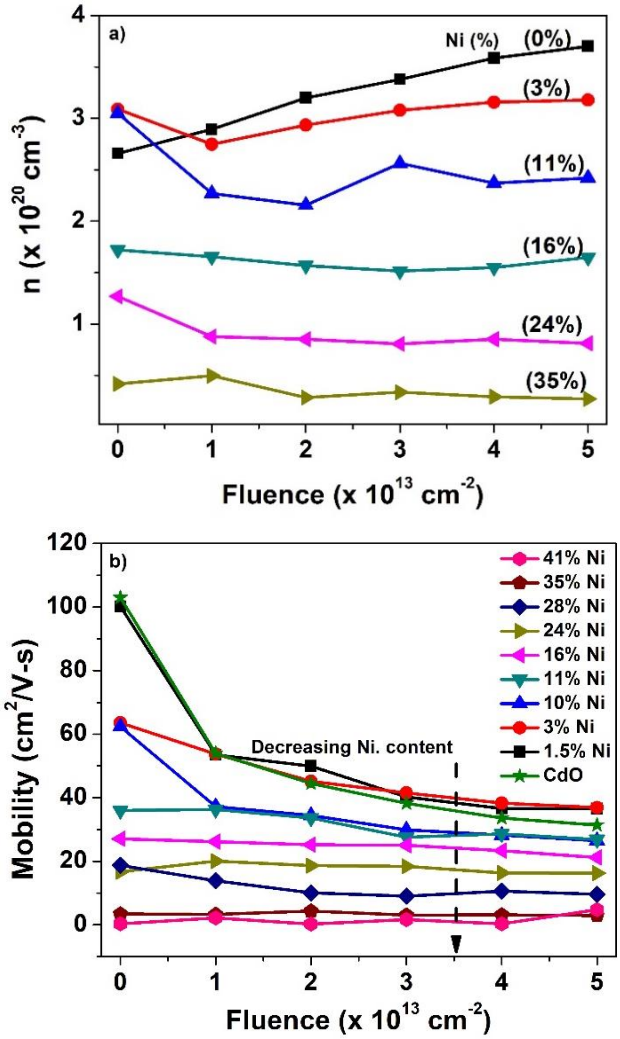

Figure 15: (a) Electron concentration and (b) electron mobility as functions of the irradiation fluence for films with different alloy composition.

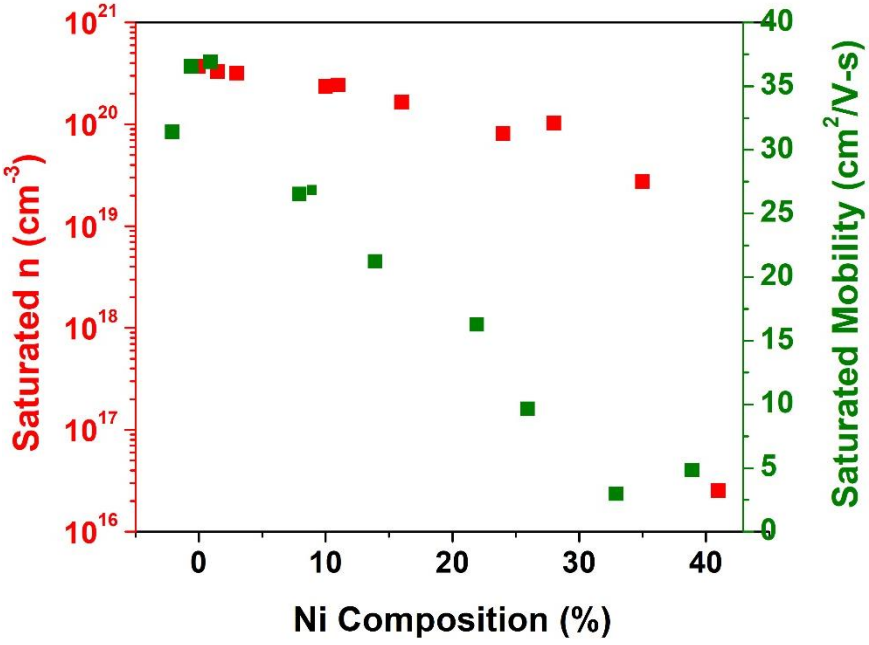

Figure 16: Saturated electron concentration and mobility for $Ni_xCd_{1-x}O$ films with different alloy composition.

Table 3: Summary of obtained data from ion irradiation experiments.

Ni Composition (%)	*As-grown electron concentration, (cm^{-3})*	*Saturated electron concentration, (cm^{-3})*	*Saturated electron mobility, ($cm^2/V{\cdot}s$)*	*Saturated Fermi level, (eV)*	*Electron affinity, (eV)*
0	$2.66x10^{20}$	$3.70x10^{20}$	31.4	0.943	5.84
1.5	$1.40x10^{20}$	$3.28x10^{20}$	36.5	0.730	5.63
3	$3.09x10^{20}$	$3.18x10^{20}$	36.9	0.878	5.78
10	$7.19x10^{19}$	$2.35x10^{20}$	26.5	0.487	5.39
11	$3.05x10^{20}$	$2.42x10^{20}$	26.9	0.546	5.44
16	$1.72x10^{20}$	$1.65x10^{20}$	21.2	0.324	5.22
24	$1.27x10^{20}$	$8.13x10^{19}$	16.3	0.159	5.06
28	$8.40x10^{19}$	$1.02x10^{20}$	9.64	0.184	5.08
35	$4.18x10^{19}$	$2.73x10^{19}$	2.97	0.062	4.96
41	$1.60x10^{18}$	$2.53x10^{16}$	4.82	-0.151	4.75

5.3 Discussion of ion irradiation results

Figure 17 shows the composition dependent location of E_F relative to the CBM, as calculated from Equation 20. The saturated E_F shifts from almost 1 eV above the CBM for CdO to slightly below the CBM for the alloy with 41% Ni. Since the value of E_F corresponding to n_{sat} is located at E_{FS}, the CBM energy relative to the vacuum level is given by $E_{Affinity}=E_{FS}+E_F$. **Figure 18** shows the composition dependence of the CBM relative to the vacuum level.

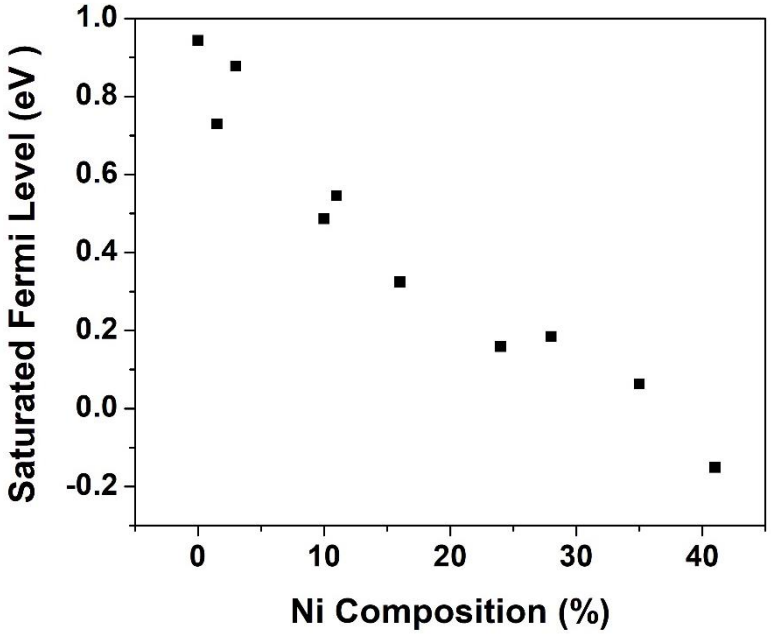

Figure 17: Composition dependence of the saturated E_F values with respect to the CBM.

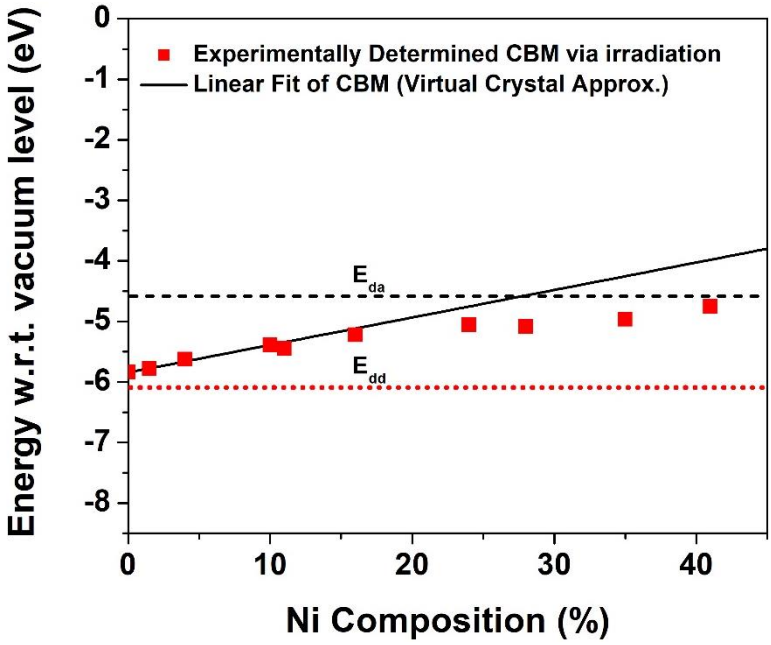

Figure 18: Composition dependence of the CBM for $Ni_xCd_{1-x}O$ alloys calculated from the E_F pinning at high irradiation fluences presented in Figure 17. The solid line represents linear extrapolation between CBM of CdO and NiO and the dashed line corresponds to E_{FS}.

It is interesting to note that initially, for compositions lower than 24% Ni, the CBM shifts upward at the rate close to that anticipated from the CBM offsets between CdO and NiO. However, it is also quite evident that the CBM shows a much weaker dependence for the compositions higher than 24% Ni. To understand this unusual dependence of the CBM on the Ni content, the effects of the partially occupied *d*-shell of Ni on the electronic band structure of the alloy need to be considered. Previous studies have shown that 3*d* transition metals (TM) can act as either acceptors or donors in standard group III-V or II-VI semiconductor compounds [174]. Hence, when a TM atom with the d^n ($1 \leq n \leq 9$) electronic configuration is introduced into a semiconductor, it can act as a donor assuming the d^{n-1} electron configuration by dropping a *d*-electron into the conduction band of the host material. It can also act as an acceptor by taking electron from the valence band and transferring into d^{n+1} configuration. The salient feature of the *d*-donor and *d*-acceptor states is that, independently of the semiconductor host, their charge transition energy is constant relative to the vacuum level [174].This behavior has been attributed to the highly localized nature of these states. In the case of Ni, the d^8/d^7 (d^8/d^9) *d*-donor (*d*-acceptor) charge transition state is located 6.1 eV (4.7 eV) below the vacuum level [174]. This places the Ni *d*-donor level at about 0.2 eV below and the *d*-acceptor level at 1.2 eV above the CBM of CdO–which is located at 5.9 eV below the vacuum level. Therefore, replacing Cd with Ni atoms in CdO introduces two highly localized states inside or in a vicinity of the conduction band of the CdO host. The system resembles a highly mismatched alloy (HMA), whose electronic band structure is determined by a BAC interaction between highly localized and extended states [177]. The BAC model has previously been used to explain the optical and electrical properties of V-doped ZnO [172]. In that case, the electronic band structure of the conduction band was determined by the interaction of the localized V *d*-donor level with the conduction band of the ZnO host.

In all previously considered cases of HMAs, the electronic band structures have been described in terms of the "two-level" BAC model in which localized states interact only with the energetically closest band of extended states [171, 178-181]. However, in the case of $Ni_xCd_{1-x}O$, this model must be modified to account for the fact that the two *d*-levels of Ni both lie near the CdO CBM and NiO VBM. Therefore, it is necessary to consider a quantum mechanical framework with three interacting energy levels: one associated with the extended states of the $Ni_xCd_{1-x}O$ matrix and two with the localized Ni acceptor and donor states. The quantum mechanical problem is depicted by a 3x3 Hamiltonian given by equation 22. By assuming that these interactions can be treated as perturbations, the following BAC Hamiltonian was developed and applied:

$$H = \begin{bmatrix} E_M(k) & C_{da}\sqrt{x} & C_{dd}\sqrt{x} \\ C_{da}\sqrt{x} & E_{da} & 0 \\ C_{dd}\sqrt{x} & 0 & E_{dd} \end{bmatrix}, \tag{22}$$

in which $E_M(k)$ is the energy dispersion of the $Ni_xCd_{1-x}O$ matrix conduction band and E_{da} and E_{dd} are, respectively, the energies of the Ni *d*-acceptor and *d*-donor levels relative to the

bottom of the conduction band. [10] The parameters C_{da} and C_{dd} describe the strength of the interaction between the respective localized Ni levels and the extended states of the $Ni_xCd_{1-x}O$ matrix. Here, it is assumed that there is no interaction between the localized *d*-donor and *d*-acceptor states. The three solutions of the eigenvalue problem for the Hamiltonian in equation 22 represent three conduction subbands. The composition dependencies of the subbands' minima and maxima are shown in **Figure 19 (a)** along with the experimentally determined conduction band edge energies from Figure 18. In the virtual crystal approximation, the coupling parameters linearly depend on the Ni content, x, and are given by, i.e. $C_{dd} = C_{dd0}$ (1-x) and $C_{da} = C_{da0}$ (1-x). The values of C_{dd0} = 1 eV and C_{da0} = 0.75 were used in these calculations based on the coupling parameters use in previous BAC studies [178].

As can be seen in **Figure 19 (a)**, the experimentally determined CBM is in excellent agreement with the calculated composition dependence of the minimum of the subband, E_{C2}. This is fully understandable since it should be noted that the *d*-donor derived, fully occupied subband, E_{C3}, as well as *d*-acceptor derived, completely empty subband, E_{C1}, do not contribute to the charge transport. Therefore, the electrical properties of Cd-rich $Ni_xCd_{1-x}O$ are fully determined by charge transport in the partially occupied subband E_{C2}. The three-level BAC model can also account for, as shown in Figure 15(b), the rapid reduction of the electron mobility with increasing Ni content. The mobility in as-grown $Ni_xCd_{1-x}O$ decreases from about approximately 100 $cm^2/V{\cdot}s$ in CdO to approximately 2 $cm^2/V{\cdot}s$ in $N_{ix}Cd_{1-x}O$ with 31% Ni content [100]. The rapid mobility decrease can be attributed to changing character of the subband E_{C2} from delocalized for Cd-rich alloys to highly localized *d*-band like for higher Ni content. **Figure 20** shows the dispersions for the three conduction subbands calculated using our three-level BAC model. It is seen that the electron conducting subband evolves from a band of fully extended states in CdO, E_C, to an increasingly flat localized band for the higher Ni content alloy, E_{C2}.

The associated flattening of the subband, E_{C2}, dispersion leads to a rapid increase of the electron effective mass. This is expected to cause a reduction of the electron mobility. Interestingly, as is shown in **Figure 21**, the saturated electron mobility appears to be directly proportional to the width of the E_{C2} subband defined as E_{da} – E_{C2} (k=0). Figure 19 also shows that the VBM that is predominantly formed of O 2*p* orbitals that shift upward towards the Ni *d*-levels, leading to BAC interactions and a reconstruction of the valence band structure in NiO-rich alloys. The BAC interaction of the *d*-donor level with the valence band of $Ni_xCd_{1-x}O$ matrix leads to formation of two valence subbands—E_{V1} and E_{V2}. It is interesting to note that the close energetic proximity of the O 2*p* and *d*-donor band accounts for the well-known hybrid nature of the VBM of NiO and the low hole mobility in this material [134, 140-142, 148-149]. The above discussion also indicates that the electrical transport properties of $Ni_xCd_{1-x}O$ alloys can be explained by a BAC interaction between localized *d*-states of Ni and the extended bands of the $Ni_xCd_{1-x}O$ host matrix.

[10] A full description of the associated MATLAB code for the BAC framework is given in Appendix G. **Credit:** Maribel Jaquez for drafting and executing this code, and providing her BAC expertise.

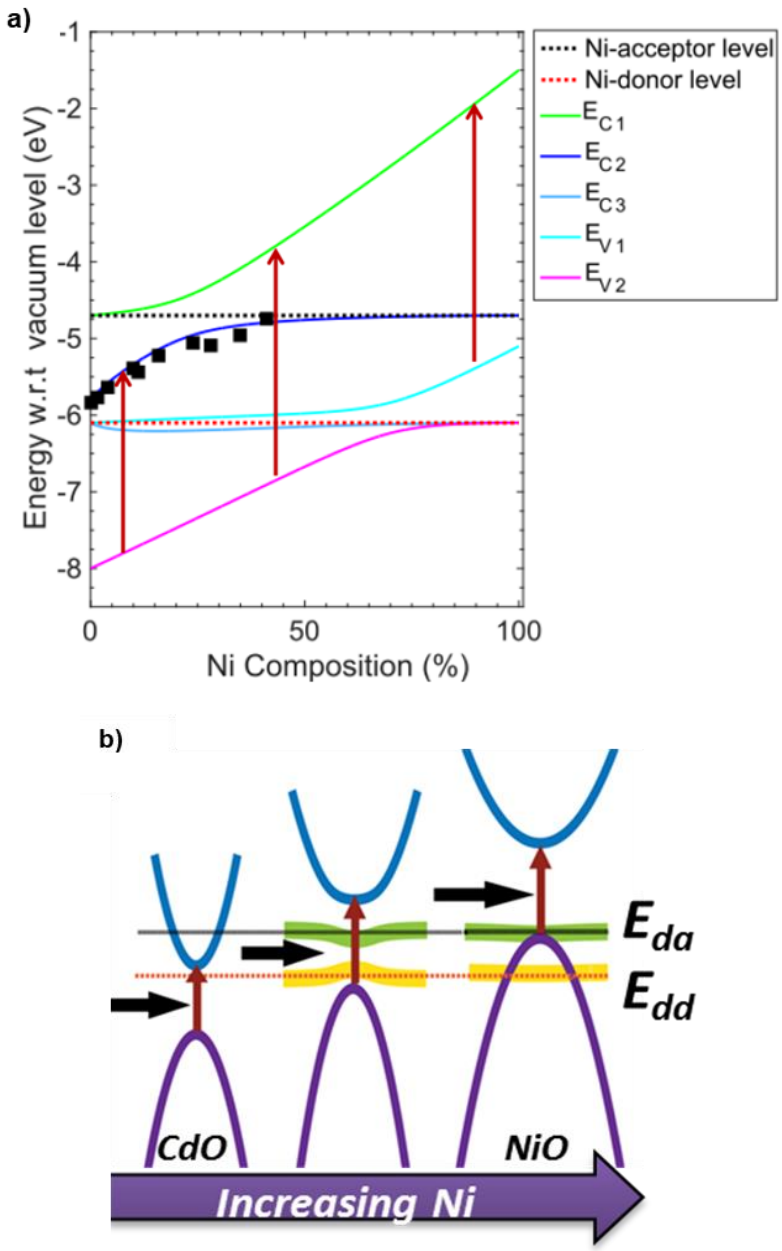

Figure 19: (a) Subband energies calculated for $Ni_xCd_{1-x}O$ calculated using the BAC model as a function of Ni content. The solid squares represent the experimentally determined CBM energies from Figure 17 and the red arrows indicate the dominant optical transitions at a given Ni composition. Part (b) shows a simplified schematic of the transitions and band edge changes in (a).

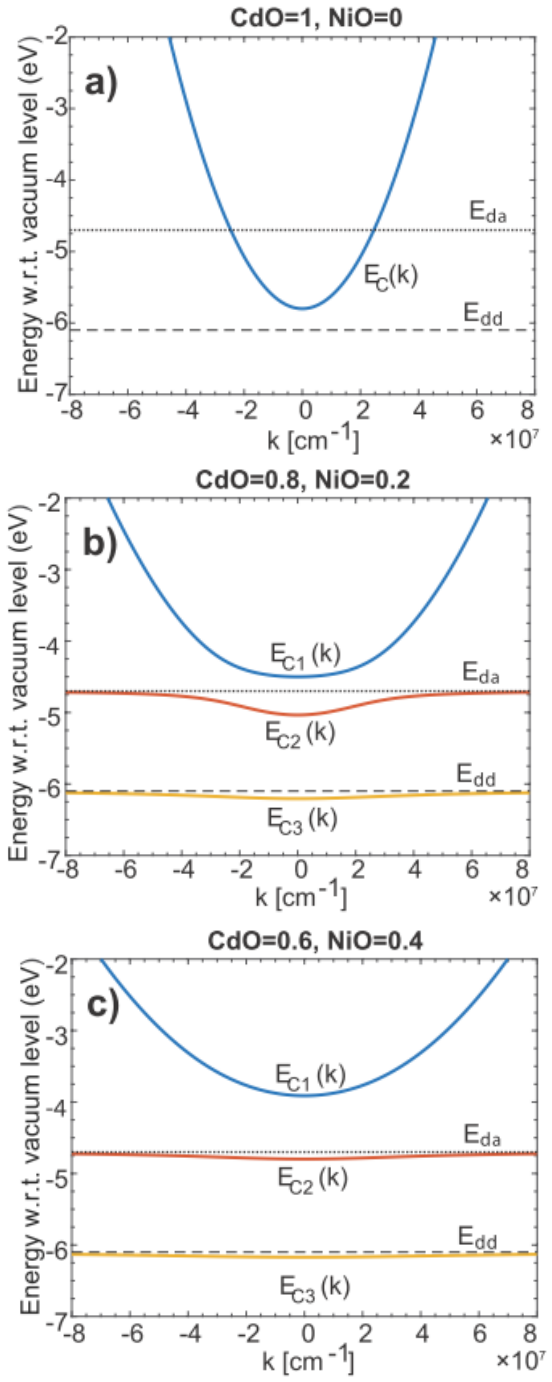

Figure 20: Dispersions for the three conduction subbands calculated using a three-level BAC model. Note the evolution in the CB electronic structure from one to two bands with added Ni.

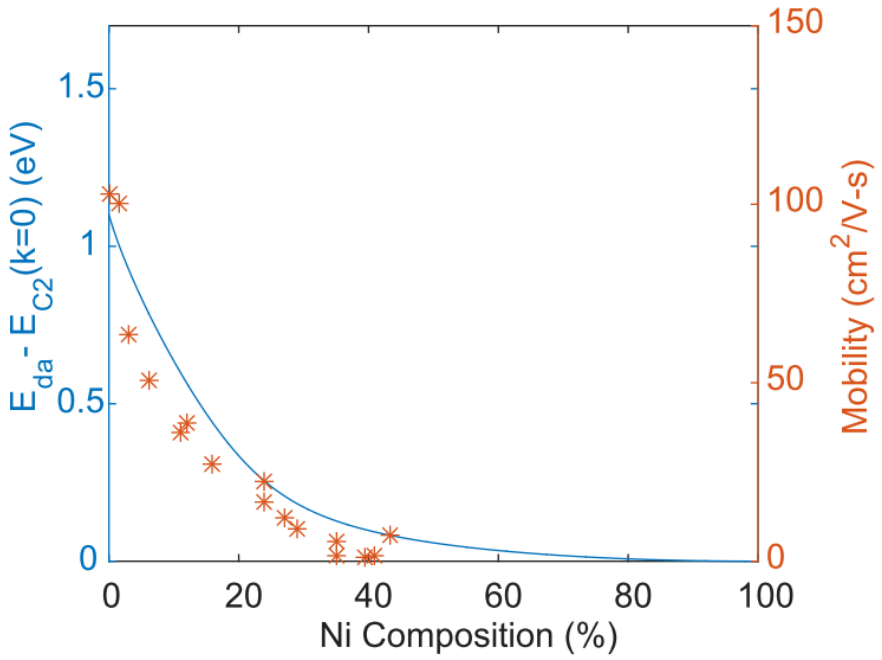

Figure 21: Calculated width of E_{C2} subband shown in Figure 20 and experimental mobility from Reference [100] plotted versus Ni composition.

In Chapter 4**,** the optical properties of this alloy displayed an unusual composition dependence of the E_g of this alloy. In contrast to all known cases of semiconductor alloys, the optical E_g of $Ni_xCd_{1-x}O$ shows a super linear behavior with an upward bowing [100]. To understand this unusual composition dependence of the band gap identification of the strongest optical transitions amongst all possible transitions between valence and conduction subbands shown in Figure 19 is needed. In general, the strength of optical coupling depends on the overlap of the wavefunctions of initial and final states. Therefore, the strongest coupling is expected between extended *s*-like and *p*-like bands and the weakest coupling is expected for transitions involving highly localized *d*-like states. The character of the wavefunction for a given subband can be discerned from the location of the subband relative to the unperturbed states. Hence the subbands closest to the Ni *d*-levels are highly localized and do not contribute to the optical absorption. Consequently, the optical absorption is dominated by three different transitions in three different composition ranges, as is shown in **Figure 22**.

The calculated composition dependence of the optical transition energies provides a good overall explanation for the evolution of the optical band gap with composition. The exceptions are the transition regions close to 25% and 75% Ni content where the localized *d*-levels intersect with the CBM and VBM, respectively. This is understandable as two different optical transitions from two subbands contribute to the optical absorption in these regions and the experimentally determined single absorption band edge is a sum of two broadened absorption edges.

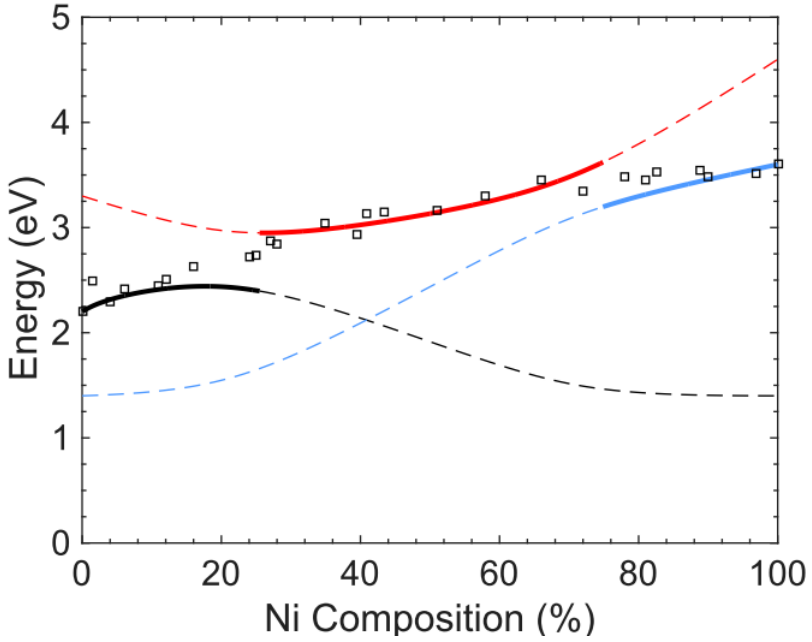

Figure 22: Subband energy transitions as a function of Ni content for $Ni_xCd_{1-x}O$ across the entire composition range using our 3x3 BAC Hamiltonian. The black squares represent the experimentally determined bandgap values as reported in Reference 96. Note that there are three regions, each of which corresponds to unique energy transitions.

The results in Figure 19 and Figure 22 provide a straightforward explanation for the origin of the upward bowing in the composition dependence of the bandgap of $Ni_xCd_{1-x}O$. As is seen in Figure 19, the absorption edge in the mid composition range is associated with optical transitions from E_{V2} to E_{C1} subband. However, as the E_{V2} subband is pushed down by the BAC interaction with the E_{dd} level and E_{C1} is pushed up by the BAC interaction with E_{da} level, the energy of this transition is larger than the energy expected from a linear interpolation of the virtual crystal approximation. Therefore, it can be argued that the *d*-levels play a role of "dark states" that affect the electronic band structure but do not contribute to optical transitions.

Furthermore, the effects of the Ni *d*-levels in other Group-II oxide alloys can now be explained. This is a novel breakthrough, one that gives context to the previously reported, but unexplained, electrical transport and optical behavior found in $Ni_xCd_{1-x}O$, $Ni_xMg_{1-x}O$ and $Ni_{1-x}Zn_xO$ alloys [150-155]. The interactions govern the measured electrical and optical properties of these alloys. A negative optical band bowing parameter for example has been recently found in $Ni_{1-x}Zn_xO$ [150]. This behavior is consistent with repulsive BAC interaction between *d*-acceptor level of Ni and the conduction band edge of the host matrix. Another recent study of the optical properties of $Ni_xMg_{1-x}O$ alloys has shown a large, more than 1.5 eV, reduction of the optical E_g energy of the alloy at low Ni content [155]. The effect has been explained by the onset of optical absorption originating from transitions between narrow band associated with Ni *d*-levels and the conduction band edge.

Overall, the behavior in $Ni_xCd\text{-}_{1-x}O$ contrasts sharply with the composition dependence of the E_g of standard semiconductor alloys, where the BAC interaction occurs between optically active states and always leads to band gap reduction and downward bowing.

5.4 Photoemission results and discussion

The distinct electronic structure of NiO and CdO, as discussed in Section 2.4 and later confirmed by ion irradiation and BAC modeling in Section 5.3 is expected to change the $Ni_xCd_{1-x}O$ core levels. The core levels take on a different character due to chemical shifts and changes in bonding with film composition. XPS analyzes core levels and VB changes. It is an extremely sensitive surface technique that utilizes a soft monochromatic source (1-2 keV) of X-ray photons to probe films [32]. The X-rays are absorbed by the film, electrons are excited from the core level to continuum, travelling for a few nm before being inelastically scattering [32]. The inelastically scattered electrons introduce a background effect called the Shirley background. With the X-rays energy and the kinetic energy of detected electrons, the core-electron binding energy, $E_{Binding}$ can be determined.

The binding energy is a unique identifier and its location is correlated to the charge state of the element. The relationship between these values is given by:

$$E_{Binding} = h\nu - (E_{KE} - \phi_{det}) \text{ and } \phi_{det} = (E_{vac}\text{-}E_F), \quad (23)$$

where ϕ_{det} is the detector work function, E_{KE} is the kinetic energy of ejected electrons and E_{vac} is the vacuum energy [32]. An energy analyzer then selects the energies of the photoelectrons and bends the electrons into a curve with a static electric field to [32]. The analyzer is hemispherical with parallel plates and a variable bias. Only electrons with the appropriate E_{KE} reaches the analyzer. The data obtained from photoemitted electrons indicate the amount that the VBM $E_{Binding}$ has shifted due to changes in composition. Furthermore, the core level change provides information into the bonding; specific to $Ni_xCd_{1-x}O$ are changes in the Cd-O and Ni-O bonds. Ultraviolet Photoelectron Spectroscopy (UPS) is used similarly to UPS but with photons in the hard-UV range (15 to 40 eV) [32]. Collectively, XPS-UPS measurements enable probing of the valence band density of states [32]. A graphic of XPS on a film is shown in **Figure 23**.

Measurements by UPS and XPS were performed on separate $Ni_xCd_{1-x}O$ films in an ultra-high-vacuum (UHV). Two UHV systems were used to measure the XPS results: an ESCALAB 210 Multi-analysis system (base pressure $1.0\text{x}10^{-10}$ mbar) from Thermo VG Scientific and an Omicron GmbH Mirco-analysis system equipped with a Sphera hemispherical analyzer (7-channel). For UPS measurements, photoelectrons were excited using a He lamp and the He II (40.8 eV) excitation line whereas for the XPS measurements photoelectrons were excited with both monochromatic Al-K_α and Mg-K_α lines. For the Al-K_α spectra, a low-electron-energy charge neutralizer was used on the high Ni-content alloys. Films were introduced in the analysis chamber and were first investigated as-loaded at two different take-off angles (TOA=30° and 90°). Each film was then sputtered using a low energy Ar^+ beam for 2 minutes, to clean the surface but minimizing the damage to the alloy. All spectra have been referenced to the E_F and charge corrected to the C *1s* core level for high resistivity. All the data have been adjusted using a Shirley-background subtraction, and then fitted with the appropriate number of peaks. Details of these experimental data analysis were presented in previous publications [58, 59, 60].

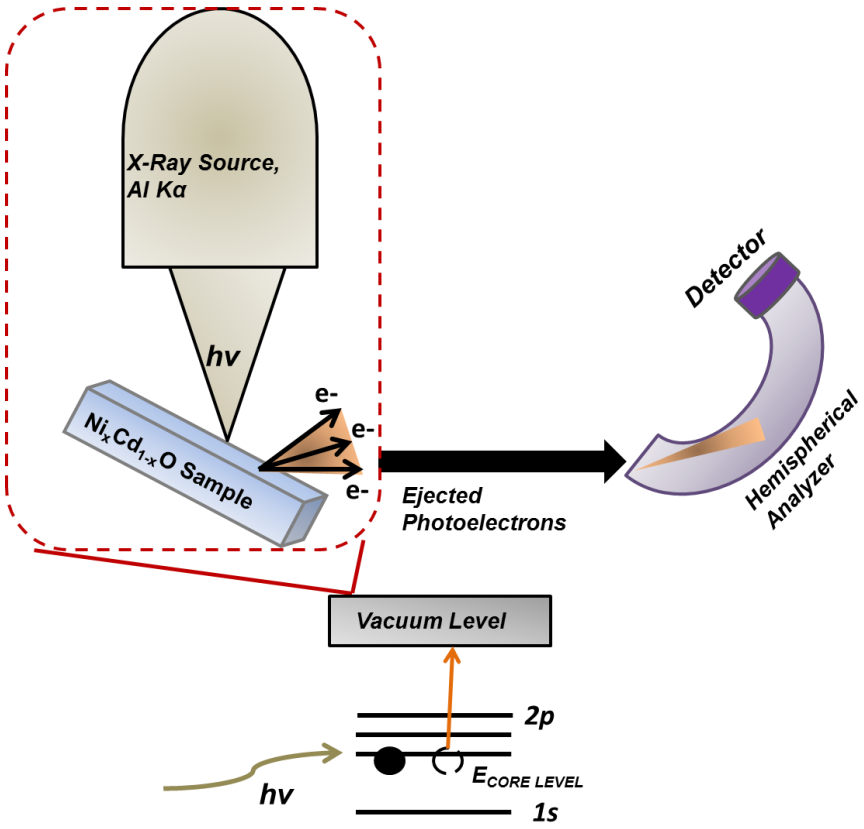

Figure 23: Principle of operation and photoemission physics for XPS-UPS experiments as adopted from References [32] and [49].

The UPS measurements provide information on the location of the highest VBM relative to the Fermi energy which, in the case of CdO, is the VBM at the L-point located at 1.1 eV below the CBM at Γ-point or at about 7 eV below the vacuum level. The results in **Figure 24** shows that the VBM L-point energy is decreasing only by about 0.1 eV with Ni content increasing from 0-41%. Since the position of the Fermi level on the absolute scale does strongly depend on the composition, this result suggests that the VBM energy at the L-point remains almost composition independent and well-separated from the Ni *d*-levels in the entire composition range. Consequently, the BAC interaction between L-point VBM and Ni *d*-level states remains negligible and does not affect electronic band structure of the valence band states responsible for the optical absorption spectra in $Ni_xCd_{1-x}O$ alloys. To reveal a composition induced shift of the Γ-point VBM UPS spectra associated with Cd 4*d* core level were measured for films with up to 41% Ni content.

The results shown in **Figure 25** indicates that adding Ni produces a pronounced shift of the photoemission peak of the Cd 4*d* core level relative to the O 2*p* VB edge. Assuming composition independent energy of the Cd 4*d* core level, the location of the O 2*p* VB edge energy in the Γ-point can be deduced. As is seen in **Figure 26**, the XPS measurements demonstrate a strong dependence of the Γ-point VBM on the composition. The overall shift deduced from the XPS is consistent with the large, about 3 eV shift of Γ-point valence band maximum shown in Figure 19.

The deeper Cd 3*d* core levels are shown in **Figure 27 (a)-(c)** through the two XPS set-ups used. Considering experimental resolution and that XPS is very sensitive to surface

conditions that may change from one experiment to other only by using different film preparation parameters, the results presented are consistent. Figure 27(a) demonstrates two features at distinct $E_{Binding}$. The first feature, at higher $E_{Binding}$, is attributed to surface contamination that leads to bonding between CdO and more electronegative species. These species include CdO_2 and $Cd(OH)_2$ and are observed in other literature. The lower $E_{Binding}$ feature at around 404 eV is attributed to Cd-O bonding. The binding energy fits within the accepted range of $E_{Binding}$, 403.7 ± 0.5eV, for the $3d_{5/2}$ level of CdO [44, 142, 158]. Similarly to the Cd 4*d* core level, the Cd $3d_{5/2}$ exhibits an upward shift but by an average of 0.6 eV to higher $E_{Binding}$. These results are supported in Figures 28 (b) and (c), which exhibits a similar shift two different TOA.

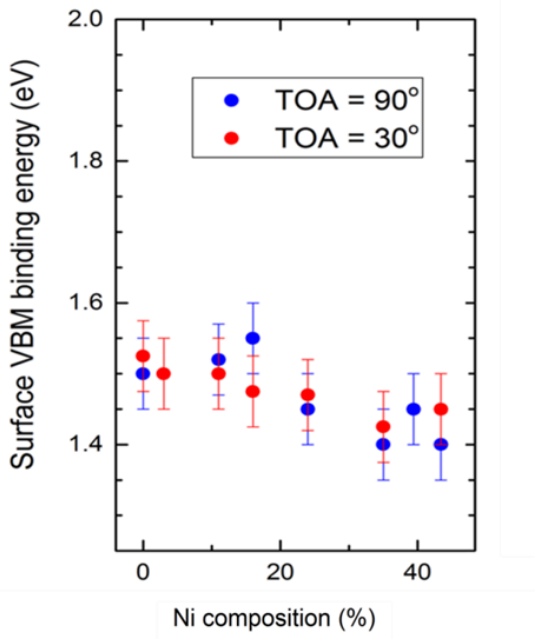

Figure 24: Composition dependence of the relative shift of the VBM at the L-point. The measurements were performed for two take off angles of 90° and 30°.

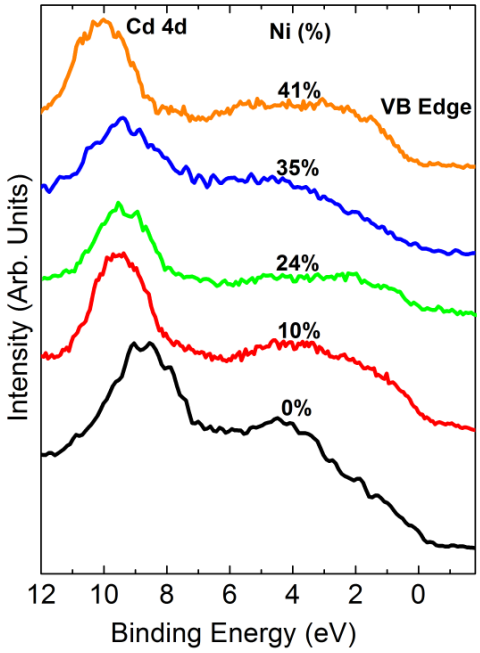

Figure 25: XPS spectra of the VB edge and Cd 4d level emission.

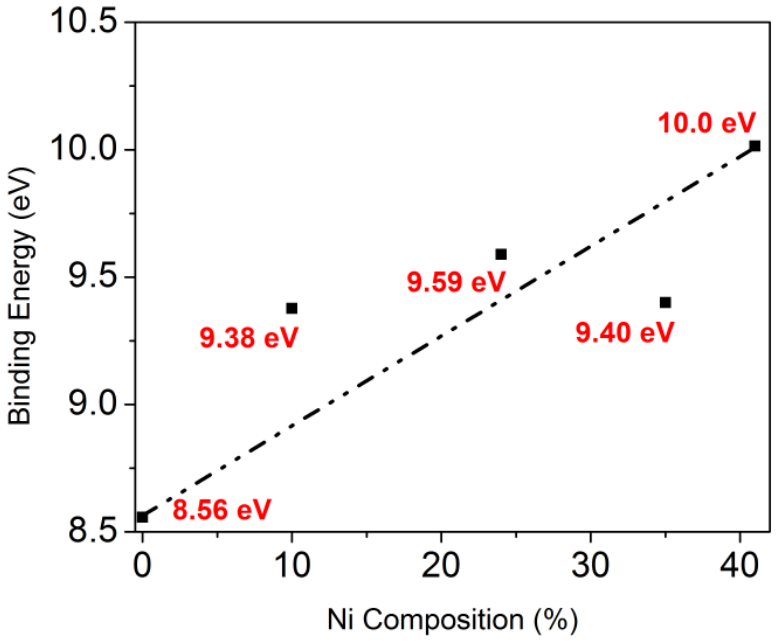

Figure 26: The VB edge shift relative to the Cd 4*d* core level.

Figure 28 shows the energy of a deconvoluted Ni 2*p* core level as a function of Ni composition due to intermixing ground level contributions from the $3d^8$, $3d^9\underline{L}$, and $3d^{10}\underline{L}^2$ configurations [182, 183, 184, 185]. The result of the intermixing is a convolution of multiple peaks in the photoemission spectra for the Ni 2*p* level. Identification of these peaks corresponds to the identification of different structures (for example, NiO, $Ni(OH)_2$, NiOOH) at different oxidation states (Ni^0, Ni^{2+}, N^{i3+}) [186-189]. These chemical states of Ni contribute to the XPS spectra by showing peaks near each other. Note that as the alloy becomes more NiO in character, the VB photoemission spectra fitting becomes more precise and the $E_{Binding}$ difference pre- and post-fitting is within roughly 0.2 eV. The most prominent deconvoluted peak for 3% Ni is attributed to the $Ni(OH)_2$ species, which is at 856.4 eV and 854.6 eV pre- and post-fit. This energy range agrees with literature, which assigns this species to a range of 854.9±1.8 eV. The identification of this species instead of NiO may be attributed to phase segregation in the CdO matrix at the surface and/or formation of new phases on a contaminated surface with addition of Ni. The $E_{Binding}$ of these characteristic peak shifts by 0.4 eV with Ni content up to roughly 855 eV at 88.8% Ni before being identified at 854.8 eV of NiO. Given that the main Ni 2p peak associated with NiO has been identified within an energy range of 853.7±1.3 eV, the peak is believed to correspond to the NiO 2*p* peak for higher Ni content [186-187, 190-193].

In Figures 24-26 the Ni inclusion shifts the Ni core levels by a small amount and the Cd core levels by a large amount. One should consider that the Ni $2p_{3/2}$ spectra attributed to NiO has a contribution of Ni 3*d* orbitals, which grows with added Ni. On the other hand, the Cd $3d_{5/2}$ peak appears at roughly 403 eV in pure CdO films and its VB is mainly formed from O 2*p* bands. As Ni is introduced into CdO, the Ni atoms tend to form Ni-O bonds, which are more covalent in character. These introduced Ni-O bonds attract electrons that may exist in the partially filled Ni 3*d* orbitals. As a result, there is less effective negative charges from the O-atoms' environment and the second neighbor Cd atoms are less surrounded by electrons. The environment around the Cd atoms is therefore less negative since there is a lower electron cloud surrounding the atoms. The $E_{Binding}$ of photoexcited electrons from the Cd core levels thus appears at progressively larger $E_{Binding}$ with increasing Ni.

Overall, this systematic study of the electronic band structure of $Ni_xCd_{1-x}O$ alloys bolstered our understanding of the mechanism behind the properties reported in Chapter 4. The E_F pinning at E_{FS} in high-energy irradiation-damaged materials determined the composition dependence of the CB edge energy relative to the vacuum level. The CBM behavior is explained in terms of a BAC interaction between localized 3*d* states of Ni and extended states of the $Ni_xCd_{1-x}O$ alloy host. The band structure is responsible for the composition dependence of the electrical transport properties and unique, previously observed, super linear band gap bowing. The UPS-XPS studies confirmed that the Γ- and L-point valence maxima of the Cd-rich alloys are not affected by the Ni *d*-states.

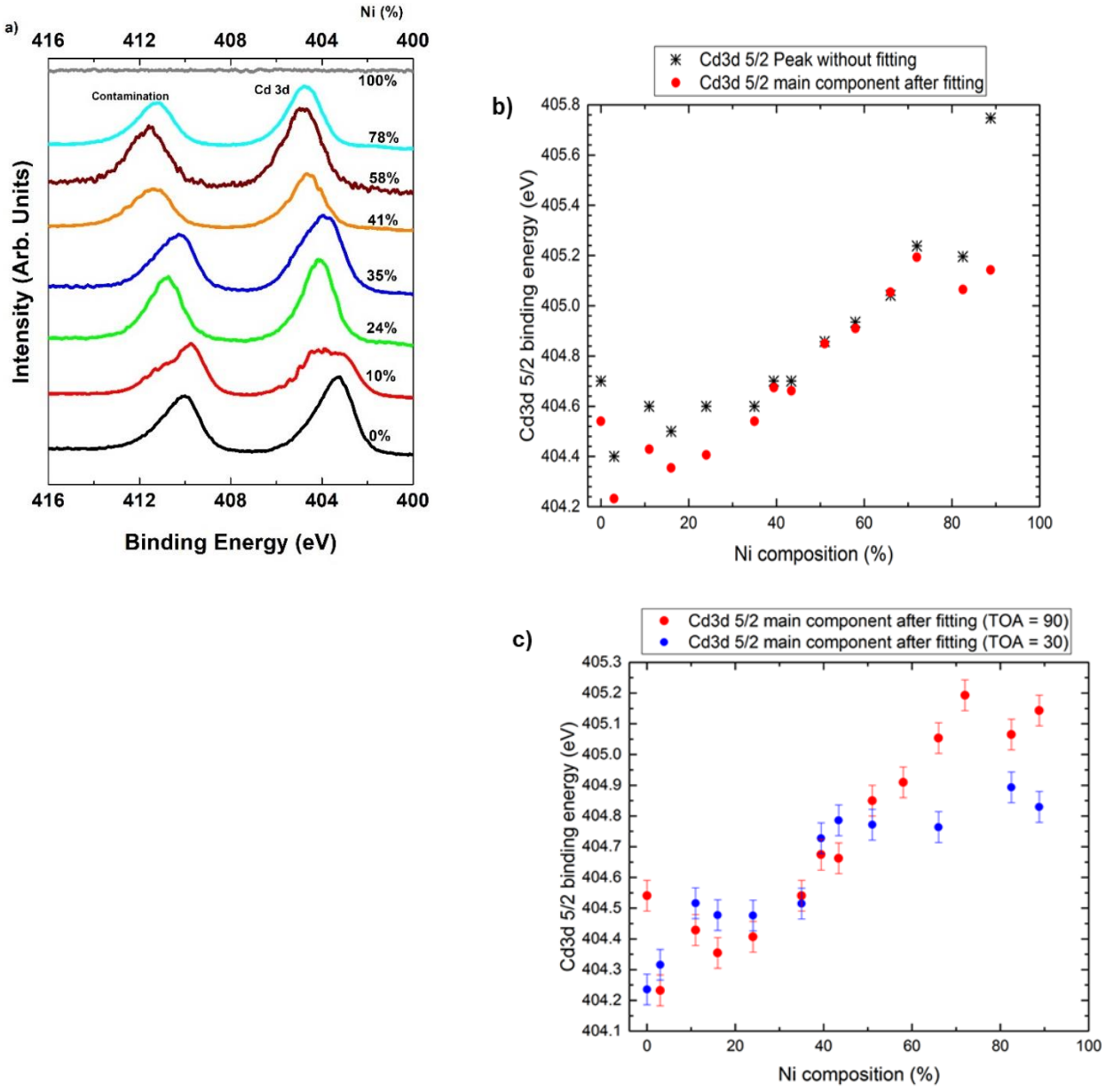

Figure 27: Cd 3*d* core-level spectra for alloys across the composition range as determined by XPS-UPS measurements. In (a) the higher binding energy features are attributed to contamination that is also seen in Reference [44], while the lower binding energy values are attributed to metal-oxygen (Cd-O) bonding across the composition range. Notice the shift to higher binding energies with Ni composition, indicating that the Cd-O chemical environment changes. These results are supported by plots (b) and (c), which displays the shift at different TOA.

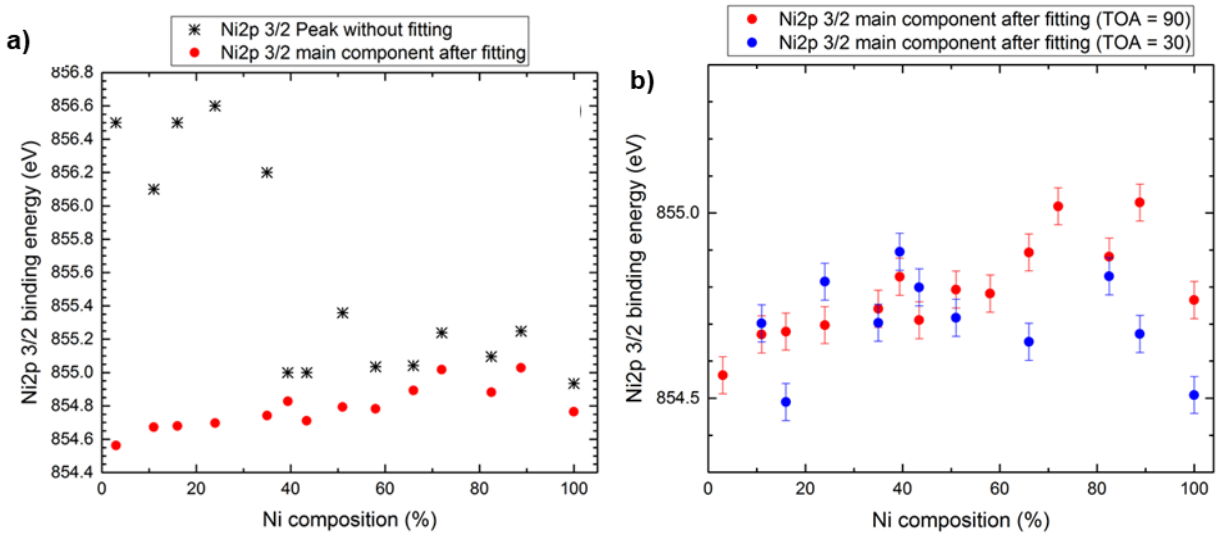

Figure 28: (a) Ni $2p_{3/2}$ core-level spectra with Ni composition as determined by XPS measurements with accompanying graph (b) showing the binding energy change as a function of Ni content for different electron TOA The results illustrate an identification of the $Ni(OH)_2$ peak, which shifts by roughly 0.3 eV with Ni content.

Chapter 6
Exploratory work on $Ni_xCd_{1-x}O$ alloys for application adoption

With greater understanding of the electrical transport, optical behavior, and electronic structure evolution in Ar sputtered $Ni_xCd_{1-x}O$, the alloys can now be tailored for applications. The efforts to modify $Ni_xCd_{1-x}O$ electrochemically, investigate the role of oxygen defects, and engineer p-type transport behavior for transparent electronics, photovoltaics, and electrochemical applications are reported. Among these applications for this material are hybrid water splitting devices, electrochromic windows, and heterojunction solar cells [52, 99, 193-194]. Component materials for water splitting devices should be conductive and should have band offsets that are near the water splitting potentials. A comparison between the band offsets of $Ni_xCd_{1-x}O$ and industrially relevant metal-oxides for water splitting following the results from Section 5.3 indicates that $Ni_xCd_{1-x}O$ with 20% and 35% Ni has comparable offsets.

6.1: Electrochemical modification of Ar sputtered $Ni_xCd_{1-x}O$

$Ni_xCd_{1-x}O$ could be attractive for many applications. For example, utilization of In or Ga as a dopant would bolster the electrical transport properties, especially for transparent conducting layers [52, 99]. Electrochromic windows, in which a window changes its transparency upon the application of a charge, is another example [31]. Globally, the inclusion of metal-oxides like $Ni_xCd_{1-x}O$ in these windows could prove critical in pursuit of low-heat and cost solutions in energy applications.

Films reported in Chapter 4 containing up to 30% Ni were electrochemically modified to determine the feasibility of redox reactions on these films [194]. Initially the films underwent coloration with a potassium phosphate dibasic treatment and then became biased at a constant potential. The electrical transport properties via Hall effect and resistivity measurements, optical properties using an optical photospectrometer, and structural properties via RBS, XRD, and XPS were then measured. Afterwards, a reverse positive potential was applied and the change in the electrical, optical, and structural properties were re-measured.

Figures 29 (a) and (b) show the transparency behaviors for several colored, bleached, and biased films taken from a $Ni_xCd_{1-x}O$ film of 24% Ni. An unbiased and uncolored film served as the control and was used as a benchmark. Relative to as-grown, unbiased, and colored films, the colored and positively biased (to +1.5 V and +3 V) films with 24% Ni do not decrease in transparency or change color. By contrast, the colored and negatively biased films (to -1.5 V and -3 V) of the same composition experience a marked decrease in transparency and change color—as shown by a change in film color to black and increase in absorption [194]. These changes compounded with increasing negative potential. Perhaps most striking is that a film that was negatively biased to -1.5 V and then subjected to a positive bias of +1.5 V recovered some of its transparency and color. A +3 V to -3 V potential swing does not reverse the color or transparency features of the films however. This result suggests for optimal reversibility in transparency for these films.

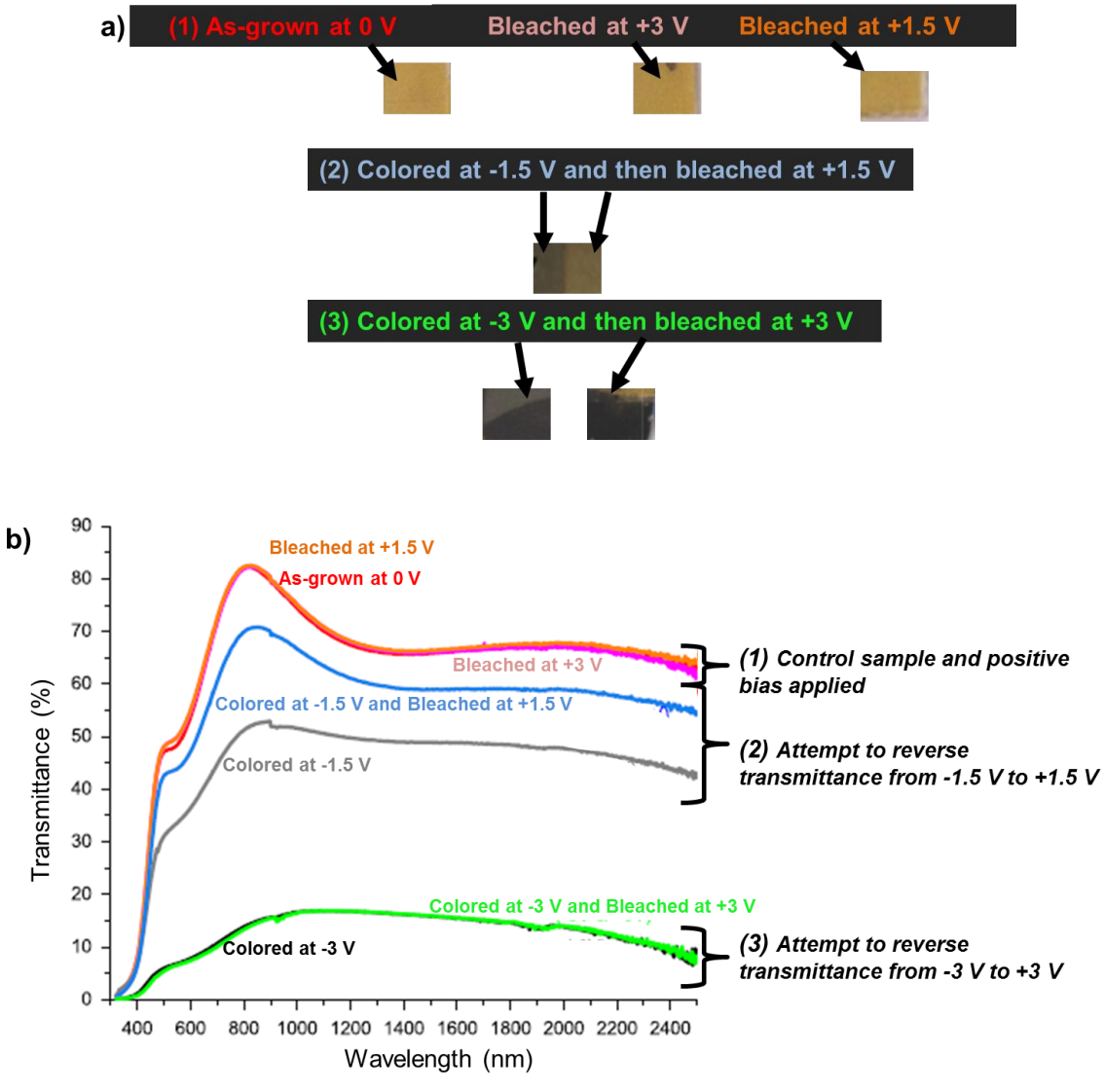

Figure 29: (a) Images and (b) corresponding measured transmittance versus photon wavelength for $Ni_xCd_{1-x}O$, 24% Ni, subjected to various coloration, bleaching, and biasing treatments. Adapted from Reference [194].

There is an increase in electron concentration and sharp decrease in mobility for treated films when compared to as-grown films. Collectively, the results hint at oxygen deficiencies, a behavior confirmed via structural results. RBS spectra, XRD patterns and XPS measurements showed that the films become oxygen deficient upon coloration and application of a negative bias and transform phase from CdO to CdO_2 and NiO to Ni_2O_3. These irreversible reactions are accompanied by significant reductions in the film transparency. Though the films do not demonstrate full reversibility in basic properties upon coloration and bias application, this study is a first step in the testing and adoption of $Ni_xCd_{1-x}O$ for applications.

Overall, this study continues the motif presented in other chapters that oxygen stoichiometry is essential to making industry ready $Ni_xCd_{1-x}O$. This will be probed in the following sections.

6.2: Realization and investigation of tunable n-and p-type $Ni_xCd_{1-x}O$ across the composition range

In recent studies, nonstoichiometric NiO gained attention as a candidate for p-type front-side transparent electrodes in c-Si PV schemes, hole transport/electron blocking layers in perovskites, hole injection layers in organic LEDs, and p-n junctions in future generation thin film PVs [195-201]. These studies point to the favorable band alignment, large E_g, and chemical stability of NiO over industrially relevant materials. However, NiO is typically limited by its relatively low, and non-reproducible, conductivity. $Ni_xCd_{1-x}O$, with known band offsets and the possibility of changing charge carrier type, can make NiO application-ready through improvement of its intrinsic properties by alloying. So far, measurable n-type behavior in $N_{ix}Cd_{1-x}O$ is achievable in a O_2 deficient ambient (100% Ar gas content); which promotes electrically active donor defects in the form of oxygen vacancies [48, 100]. Moreover, p-type electrical behavior is not measurable for Ar sputtered films.

Previous studies, however, argue that NiO processed under environments containing O_2 displays p-type conductivity due to Ni vacancies [46-48, 130, 136]. But the defects and mechanisms needed to induce p-type conductivity in $Ni_xCd_{1-x}O$ films are unknown. The literature presented in Chapter 2 and the findings from Chapters 4 and 5 serve as a starting point for the investigation of the mechanisms behind the $Ni_xCd_{1-x}O$ conductivity, development of p-type $Ni_xCd_{1-x}O$, and further enhancement of conductivity for applications. [11]

6.2.1: Rapid thermal annealing of Ar sputtered $Ni_xCd_{1-x}O$

Rapid thermal annealing (RTA) studies of Ar sputtered (gas content of Ar, 100%) $Ni_xCd_{1-x}O$ in pure O_2 and nitrogen (N_2) environments were performed to link O_2 content, annealing temperature, and electrical transport properties.[12] Films were annealed between 300 and 450^{0}C in 30 second increments and their electrical transport properties were measured with the Hall effect. Measurement of film stoichiometry by RBS showed that

[11] The defect formation under these conditions was discussed in Section 2.3.

[12] Please note the nomenclature differences: "oxygen" denotes film stoichiometry and O_2 denotes gas content of annealing or sputtering ambient.

films are O_2 deficient. Nevertheless, the annealing studies of these films elucidates the sensitivity of $Ni_xCd_{1-x}O$ to oxygen.

Figures 30 (a)-(c) show the electron concentration, mobility, and resistivity for O_2 annealed films. These figures show concentration and mobility decreases and a resistivity increase with Ni composition. The largest decrease occurs for films annealed at 450^0C[13] in O_2. As is shown in **Figures 31(a)-(c),** films annealed in O_2 or N_2 display the same trends as measurements of their pre-annealed versions. The sensitivity of these films to O_2 content however is significant. For N_2 annealed films up to 450^0C the electron concentration and mobility also decreases and the resistivity also increases with composition. And in both figures, the films become unmeasurable at 35% Ni. However, the magnitude of decrease for N_2 and O_2 annealed films differ.

The electron concentration difference, as shown in **Figure 31 (a)**, is approximately one to three orders of magnitude between the two conditions. This experimentally indicates the sensitivity of these metal-oxide films to oxygen. Although the annealing temperature supplies thermal energy for oxygen migration, and the band offsets in Chapter 5 predict low formation energies for donor defects, annealing in oxygen fills oxygen vacancy sites. Annealing in O_2 could, therefore, initiate oxygen inclusion at or below the film surface and reduce the number of available double donor sites[14]. These results motivated the subsequent growth of $Ni_xCd_{1-x}O$ in sputtering environments containing mixtures of pure O_2 and Ar gases for further investigation.

6.2.2: Processing and annealing of Ar+ O_2 sputtered $Ni_xCd_{1-x}O$

Moving forward from the initial RTA experiments, films were grown in environments containing gas mixtures of $Ar+O_2$. In the sputtering configuration used, the O_2 gas content was changed through manipulation of the gas flow rates[15] for pure Ar and O_2 gases. The amount of O_2 with the environment is expressed as the percentage of gas flow attributable to O_2. The mixtures varied from 0% to 100% O_2 content.

First, the endpoint compounds were grown and their measurable electrical transport properties were plotted versus the amount of O_2 growth ambient up to 20%. These processing conditions for CdO, as shown in **Figure 32**, exhibit concentration and mobility decreases and demonstrate that the optimal processing conditions for highly conductive CdO must be deficient in O_2.

By contrast the behavior for NiO films, as shown in **Figure 33**, is significant because there is a measurable resistivity at a gas mixture of Ar+2% O_2. This result is the opposite of NiO films grown with 0% O_2 (Ar gas content= 100%), which has no measurable resistivity. The resistivity rises to when grown in mixtures of Ar+50% O_2, and decreases to its lowest value at 100% O_2 (Ar gas content=0%)—further demonstrating the film sensitivity to oxygen stoichiometry. Processing of NiO under O_2 rich gas ambients likely leads to Ni vacancy formation to accommodate the excess oxygen formed—leading to a measurable resistivity. The resistivity of 10^{-1} Ω-cm, though higher than an n-type film, is significant for p-type conducting films.

---

[13] Subsequent film annealing at 500^0C converged to similar values as 450^0C before degrading at 550^0C.

[14] Recall Equation 2.

[15] Expressed in units of standard cubic centimeter per minute, sccm.

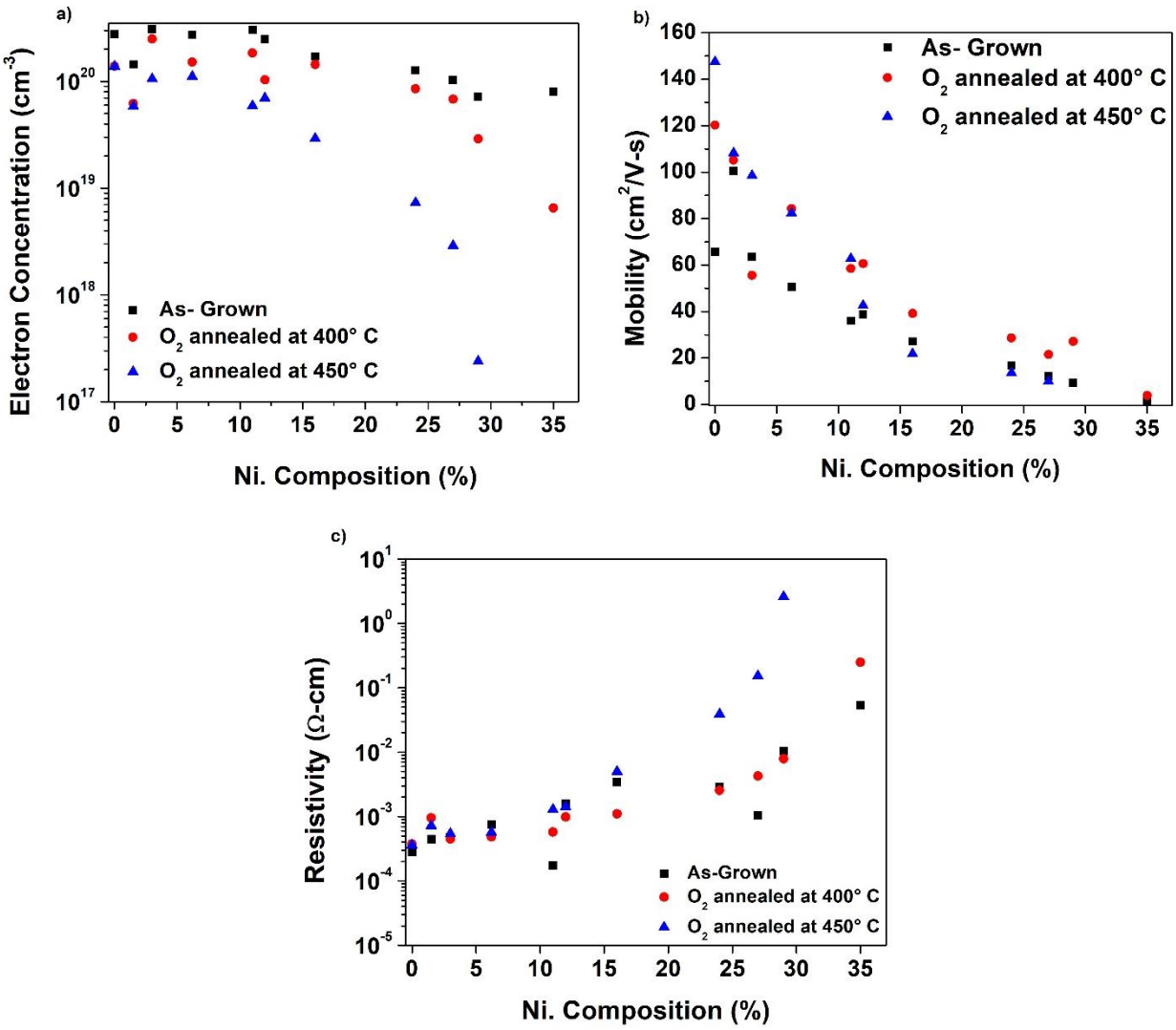

Figure 30: Comparison of the (a) electron concentration, (b) mobility, and (c) resistivity of Ar sputtered $Ni_xCd_{1-x}O$ pre- and post-RTA in pure O_2 at 400^0C and 450^0C. Films containing 35% Ni became unmeasurable upon annealing at 450^0C.

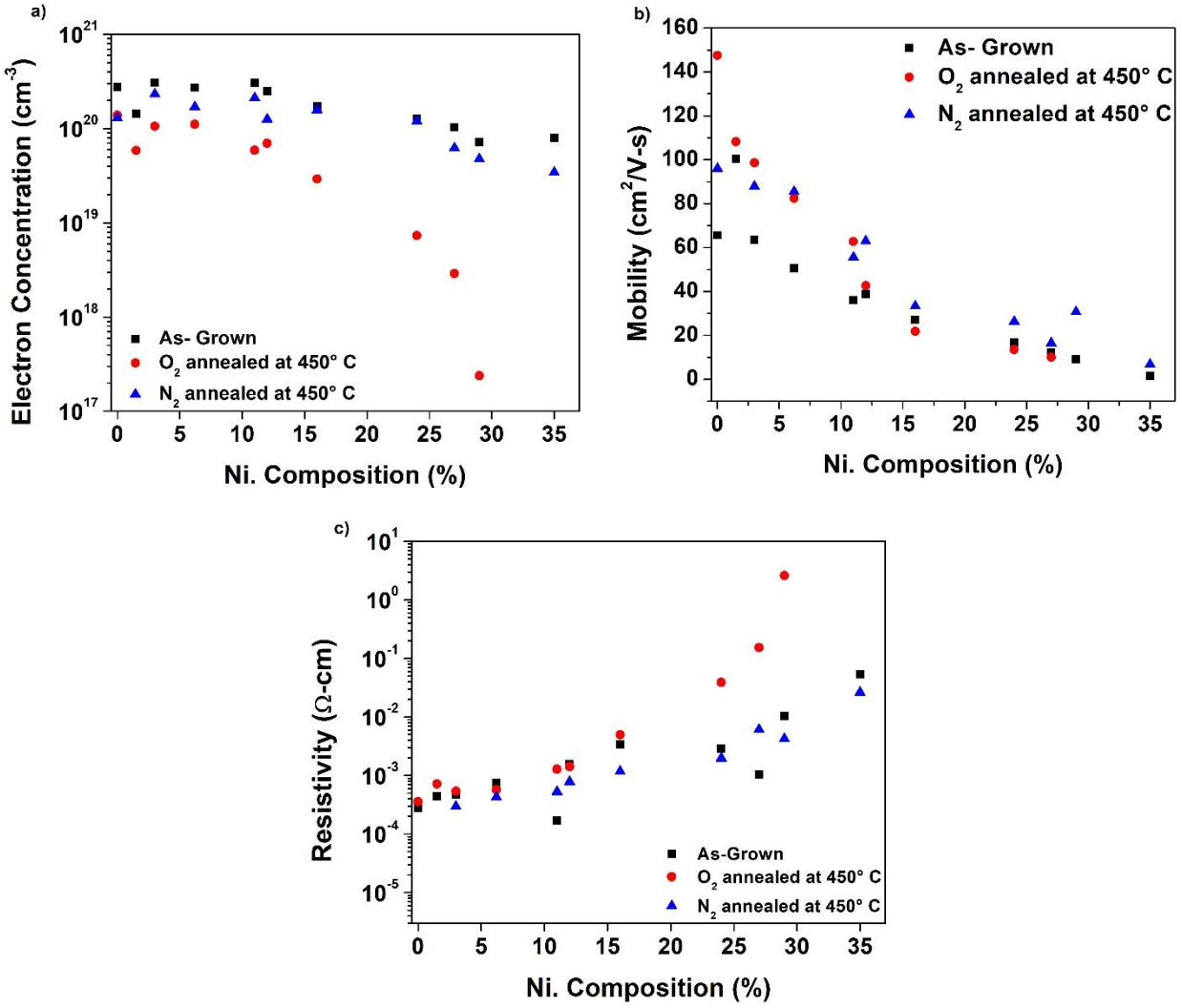

Figure 31: Comparison of the (a) electron concentration, (b) mobility, and (c) resistivity of Ar sputtered $Ni_xCd_{1-x}O$ films pre- and post-RTA in pure O_2 and N_2. Films containing 35% Ni became unmeasurable upon annealing at 450^0 C.

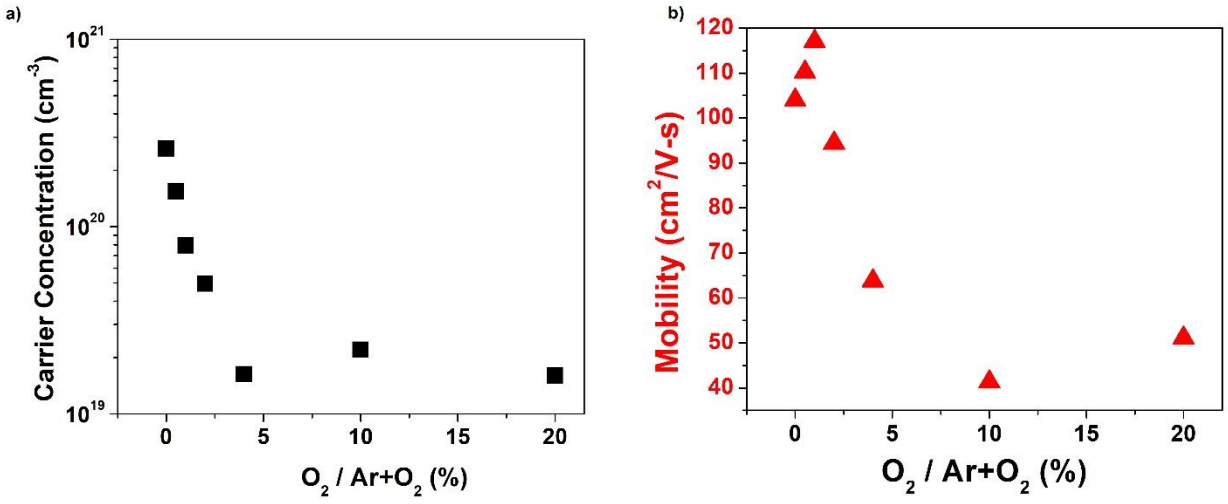

Figure 32: Comparison of the (a) electron concentration and (b) mobility of CdO grown in sputtering environments containing mixtures of O_2:Ar gas content.

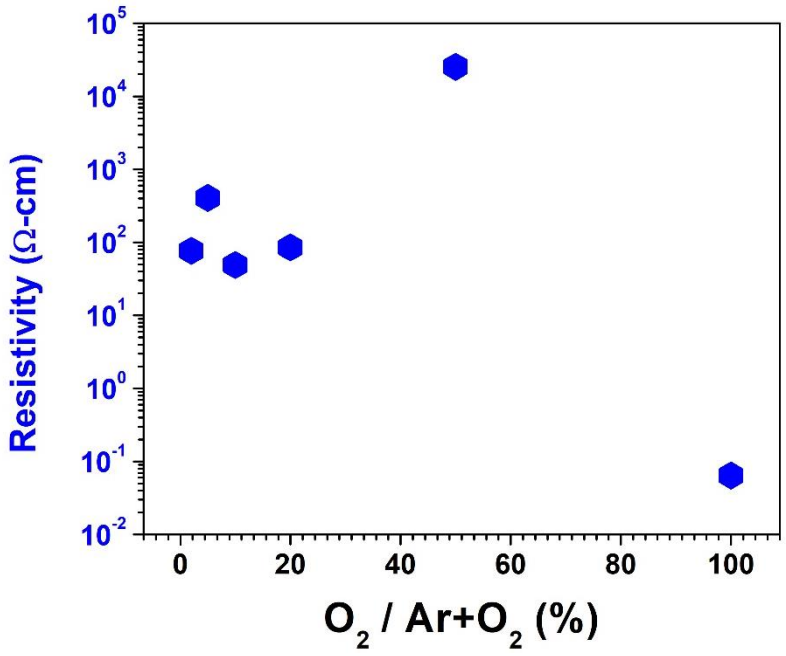

Figure 33: Resistivity of NiO grown in sputtering environments containing mixtures of O_2:Ar gas content.

Films with intermediate Ni composition range were then grown in Ar+O_2 ambients containing different O_2 gas contents and their electrical transport properties were measured. The properties were measurable across the entire composition range for films grown in an ambient of Ar+20% O_2. When compared to films grown in an ambient of 0% O_2, as is shown in Chapter 4, there is a clear difference in the composition ranges that display measurable electrical behavior. This comparison is shown in **Figure 34.** While the films grown under 0% O_2 (Ar gas content=100%) are measurable up to 43.4% Ni (red circles) and become highly resistive, the films grown in Ar+20% O_2 are measurable across the entire composition range (black squares). Beyond 43.4% Ni the resistivity ranges from

10^1 to 10^3 Ω-cm. To determine the charge type of these films, thermopower measurements were employed. The results, plotted in **Figure 35 (a)**, showed that films containing >48% Ni are p-type and films containing <48% Ni are n-type. These results show that the tunability in charge type for $Ni_xCd_{1-x}O$ is measurable and reproducible across the composition range; these are the first such results are reported for this alloy. This behavior can be explained with the band edges, reported in Chapter 5 and reproduced in **Figure 35 (b)**. Films containing <48% Ni are strongly n-type because the E_{FS} is positioned within or near their CBM. At these compositions, donor defect formation is strongly favored but the maximum electron concentrations achievable are not reached—for reasons explained by Figure 32. Above 48% Ni, the E_{FS} is increasingly further away from the CBM and closer to the VBM, increasing the formation energy of donors and, conversely, decreasing the formation energy of acceptors. Consequently p-type conductivity, which is possible in a sputtering gas mixture containing O_2 and gets stronger with added Ni, occurs.

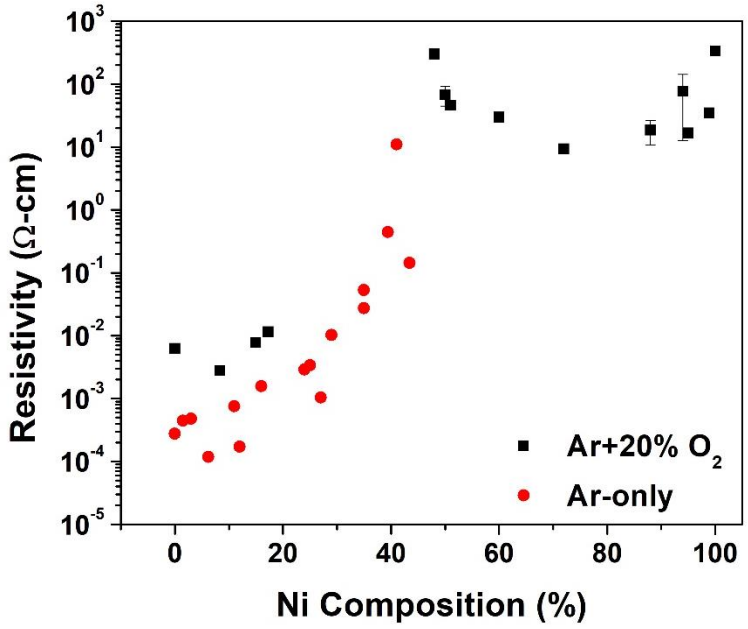

Figure 34: Juxtaposition of resistivity of $Ni_xCd_{1-x}O$ films sputtered in ambients containing in 0% O_2 (Ar only, red circles) and Ar+20% O_2 gas mixtures. The comparison indicates a link between oxygen stoichiometry and electrical transport behavior across the composition range.

The sensitivity of these films to annealing temperature was then explored. Films were annealed in pure N_2 from 200^0 to 500^0C and electrical properties were measured as a function of annealing temperature. The plot shown in **Figure 36,** with initial and final values documented in **Table 4**, shows the resistivity as a function of temperature. For films with > 62% Ni, the resistivity increases with annealing temperature. But in films with 25% Ni and above, the resistivity decreases. A film containing 62% Ni becomes immeasurable at 500^0C. In a film with 51% Ni, the resistivity remains relatively unchanged with temperature. This film, which was initially determined to be p-type with thermopower, is n-type post-RTA with an electron concentration of $\sim 10^{17}$ cm^{-3} and a mobility of ~1 $cm^2/V{\cdot}s$. Given the band edges of a film with 51% Ni, it is possible that

annealing this film creates changes in defect formation energies, and therefore, carrier type. Thermopower measurements as a function of annealing temperature were not possible on these annealed films due to film geometry. Nevertheless, thermopower changes with RTA on films with larger geometry are needed to shed more light on the carrier stability of these annealed films.

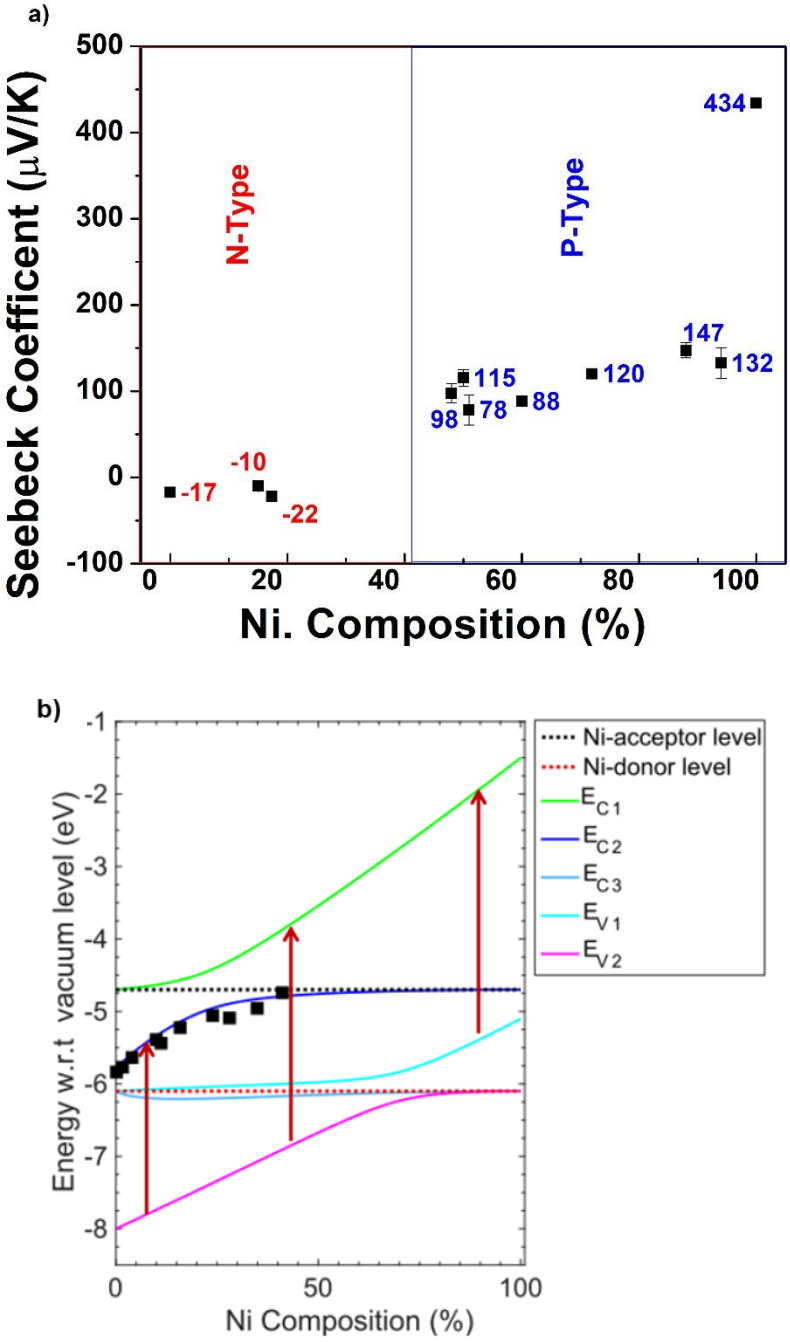

Figure 35: (a) Seebeck coefficient as a function of composition for the films sputtered in Ar+20% O_2 from Figure 34. The comparison indicates a link between oxygen stoichiometry and p-type behavior for Ni-rich films, a rarity amongst metal-oxides. These results are explainable with the determined band edges, shown in Figure 19 and reproduced in (b).

The trends for rich and dilute Ni indicates an increase in oxygen vacancy sites with annealing temperature and an overall decrease in the film's oxygen content. To confirm this explanation 25% Ni and CdO were further probed. These films, which exhibited decreases in their resistivity, also exhibited increases in their electron concentrations with annealing temperature as is shown in **Figure 37 (a)**. But their mobility trends deviate—CdO's mobility increases from ~50 to 137.2 $cm^2/V{\cdot}s$ and 25% Ni's mobility decreases from ~40 to 16.7 $cm^2/V{\cdot}s$ at 500^0C. Remarkably, these final measured electrical transport properties converge to values of their unannealed versions grown only in Ar. A comparison of these values is shown in **Table 5**. Further structural measurements by RBS of these films before and after annealing, shown in **Table 6,** reveal that the total O_2 content decreases. The stoichiometric amount of O_2 decreases for CdO and 25% Ni grown in Ar+20% O_2 versus their annealed versions, confirming that the films shift towards oxygen deficiency. Under annealing conditions, an oxygen species is migrating out of the structure, leaving compensating double donors behind. The location of these migrating O_2 is currently unknown and requires further study. Grain boundary analysis via TEM can be used to further investigate this behavior.

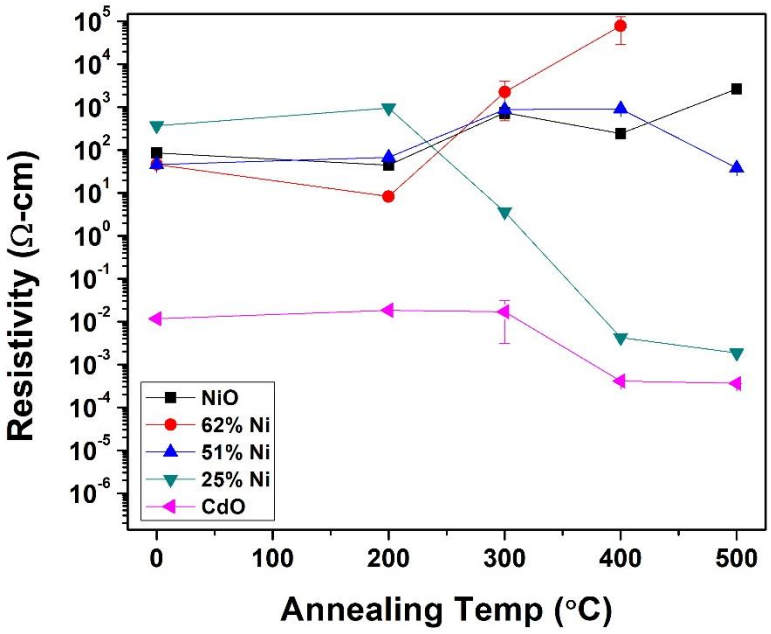

Figure 36: Resistivity as a function of annealing temperature for select $Ni_xCd_{1-x}O$ films sputtered in Ar+20% O_2 and subsequently annealed in N_2.

Table 4: Comparisons of resistivity for select Ar+20% O_2 films, pre- and post-anneal.

Annealing Temp (^0C)	***Resistivity (Ω-cm)***				
	NiO	**62% Ni**	**51% Ni**	**25% Ni**	**CdO**
0, As-Grown	8.54×10^1	4.61×10^1	4.61×10^1	3.71×10^2	1.17×10^{-2}
500	2.69×10^3	--, Highly resistive	3.80×10^1	1.85×10^{-3}	3.63×10^{-4}

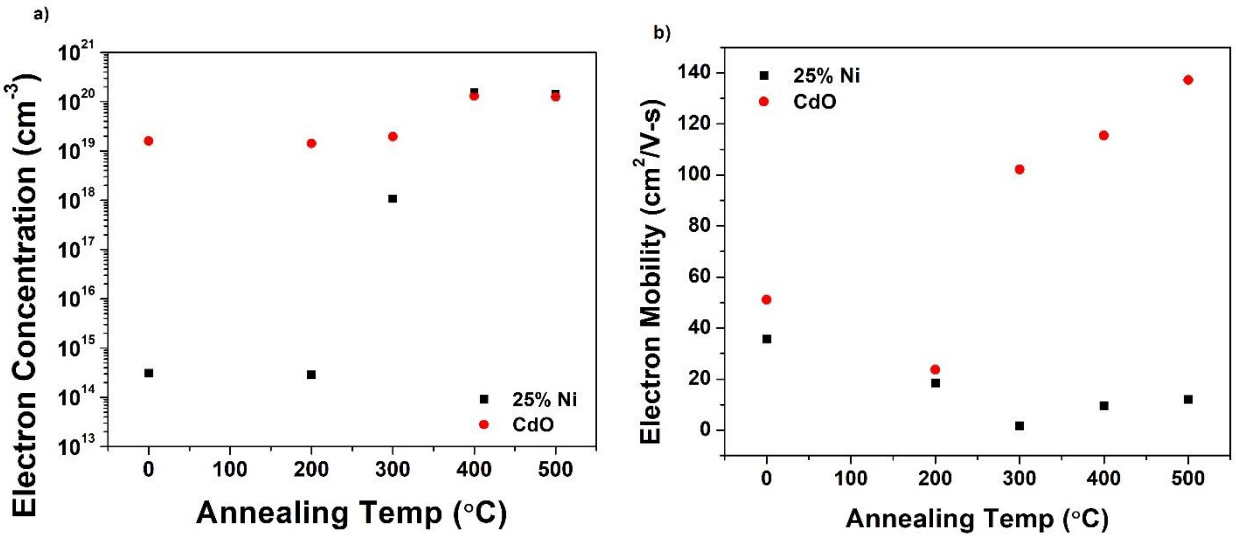

Figure 37: (a) Electron concentration and (b) mobility as a function of annealing temperature for CdO and 25% Ni films sputtered in a Ar+20% O_2 gas mixture and subsequently annealed in N_2.

Table 5: Comparison between a post-annealed version of CdO and 25% Ni grown in Ar+20% O_2 and its unannealed, Ar grown versions.

Film	*Annealing Temperature (^{0}C)*	*Growth Ambient*	*Electron Concentration (cm^{-3})*	*Electron Mobility (cm^2/V·s)*	*Resistivity (Ω-cm)*
CdO	500	Ar+ 20% O_2	1.25×10^{20}	137.2	3.63×10^{-4}
CdO	0 (As-Grown)	Ar + 0% O_2	2.66×10^{20}	103.0	3.63×10^{-4}
25% Ni	500	Ar+ 20% O_2	1.40×10^{20}	12.0	1.85×10^{-2}
25% Ni	0 (As-Grown)	Ar + 0% O_2	1.27×10^{20}	16.7	1.85×10^{-2}

Table 6: Comparison of stoichiometry for CdO and 25% Ni grown in Ar+20% O_2 and annealed at 500^{0}C in N_2.

Film	*Anneal Temperature (^{0}C)*	*Growth Ambient*	*Stoichiometry*
CdO	0	Ar+ 20% O_2	Cd 0.52 O 0.48
CdO	500	Ar+ 20% O_2	Cd 0.54 O 0.46
25% Ni	0	Ar+ 20% O_2	Cd 0. 35 Ni 0.10 O 0.53
25% Ni	500	Ar+ 20% O_2	Cd 0. 41 Ni 0.13 O 0.46

A key result from these RTA studies is that, in sputtering conditions containing ~20% O_2, measurable and tunable electrical transport behavior is possible in $Ni_xCd_{1-x}O$. To date, this is the first report of such findings for this and other metal-oxide systems. Resistivity measurements of the films demonstrate that the films become O_2 deficient upon

annealing in pure N_2, likely due to the removal of oxygen species. Overall, the resistivity measurements show the stability in carrier type and a method to control this stability. Though the formation of Ni vacancies in response to excess oxygen remains unexplored in Ni-rich films, there are opportunities in the future to investigate the density of such defects. This will be explained in Chapter 7.

Chapter 7
Conclusions and next steps

Understanding and controlling the electronic structure of materials are longstanding endeavors in semiconductor physics and technology, especially in the transparent conducting oxide community. This dissertation contributes to this endeavor by reporting studies on the development and characterization of RF magnetron co-sputtered $Ni_xCd_{1-x}O$ alloys. Overall, synthesis of isostructural $Ni_xCd_{1-x}O$ with tunable band edges, E_g and charge type with carrier composition is realized.

The rocksalt $Ni_xCd_{1-x}O$ Cd-rich alloys exhibit a rapid decrease in electron mobility from 103 $cm^2/V{\cdot}s$ to 7 $cm^2/V{\cdot}s$ and electron concentration (from $2.7x10^{20}$ cm^{-3} to $6.0x10^{18}$ cm^{-3}) with up to 43.4% Ni. This decrease in electron concentration and mobility is consistent with the movement of the CBM from below to above E_{FS} with increasing Ni content. The intrinsic E_g of the alloys can be tuned continuously from 2.2 eV (CdO) to 3.63 eV (NiO) with increasing Ni. After speculating that Ni introduces TM-impurity levels into the electronic structure of CdO and is responsible for the properties measured, a systematic study of the electronic band structure of $Ni_xCd_{1-x}O$ alloys across the composition range was then executed.

Irradiation of films leads to a saturation in the electron concentration associated with pinning of the E_F at the E_{FS}, the common energy reference located at 4.9 eV below the vacuum level. The composition dependence of the pinned E_F enabled determination of the CBM energy relative to the vacuum level. The unusually strong deviation of the CBM energy observed from the virtual crystal approximation is explained by a BAC interaction between localized 3*d* states of Ni and the extended states of the $Ni_xCd_{1-x}O$ alloy host. The resulting band structure explains the dependence between the composition and the electrical and optical properties of the alloys—the rapid reduction of the electron mobility as well as previously observed positive band gap bowing parameter. XPS-UPS studies confirm that the Γ- and L-point valence band maxima in the Cd-rich alloys are unaffected by the interaction with Ni *d*-states. As well, they resolve changes in the Cd 3*d* and Ni 2*p* core levels.

Overall, the results add context to the previously reported, but unexplained, electrical transport and optical behavior found in $Ni_xCd_{1-x}O$, $Ni_xMg_{1-x}O$ and $Ni_{1-x}Zn_xO$ alloys.

The interactions govern the measured electrical and optical properties of these alloys. The information from this dissertation is also transferable to metal-oxide based semiconducting alloys with TM acting as dopant, acceptor, or alloy agents such as V-doped ZnO.

With a foundation for the structure, properties, and behavior of Ar sputtered $Ni_xCd_{1-x}O$, the electrochemical and stoichiometric modification of the alloy was then completed. This study probed the mechanisms and discusses the processing conditions that induced reproducible and measurable p-type conductivity in $Ni_xCd_{1-x}O$. This is the first study to demonstrate a change in charge type from n to p with composition on a Group-II oxide or metal-oxide. These results demonstrate its attractiveness for applications and explain the future processing steps needed to engineer broad spectrum $Ni_xCd_{1-x}O$ with tunable electrical transport properties and charge type.

Building on the knowledge from this dissertation, we can gain an even better understanding of the defect and scattering mechanisms at play in future experiments.

7.1: Future Steps: Identification of defects

Formation and introduction mechanisms of defects are important to the control of semiconductor properties. Electrical measurements, optical spectroscopy, particle beam methods, and theoretical calculations are typically used to determine defects in semiconductors. However electrical measurements such as deep-level transient spectroscopy and variable-temp Hall effect do not directly identify defects. Additionally, OAS cannot determine defect concentrations. One technique that directly probes the nature and abundance of vacancy type defects is Positron annihilation spectroscopy (PAS). The PAS technique relies on the electrostatic attraction between positions and its environment to probe the local electron density and atomic structure of the material.

In PAS, a positron of similar mass and charge of an electron emanates from a decaying ^{22}Na isotope source and enters the film for picoseconds [32]. As it travels through the film, the positron loses energy and interacts with negatively charged defects, annihilating the positron in reactions that conserve energy and momentum. Then, two gamma rays with energy of 511 keV emit in opposite directions [32]. The positron annihilation lifetime spectroscopy and Doppler broadening spectroscopy features are used to identify vacancies [202]. The parameters that are related to the structure of the material are the time and energy of the annihilation spectra [32, 202]. Negatively charged vacant lattice sites are attractive locations that the positron can interact with. With larger open volume (i.e. more vacancies), the positron lifetime becomes high. Annihilated electrons cause a deviation from the 180° straight angle from the two gamma rays and this deviation corresponds to a Doppler shift in energy.

Groups II-VI and III-V compounds that have successfully used PAS have constituent atoms that are large. This requirement, at first, may show that PAS is not optimal for analysis of Group II-oxides since in these materials, the anion size of O, is small. However, PAS is still an effective technique and has been previously shown to be effective on alloys $Al_xGa_{1-x}N$ and $In_xGa_{1-x}N$ as well as on ZnO films in which cation vacancy complexes can be determined [202-205]. Overall, the body of work of defect spectroscopy on II-oxides is small and limited to ZnO. In ZnO, Zn-O vacancy complexes were identified in as-grown films. Furthermore, the studies of high resistance of ZnO under irradiation with subsequent annealing show that the irradiation stems from the sublattice damage (Zn vacancies) [202,

206]. Nevertheless, this alloy system could be an ideal candidate for such studies and there are many ways with which to investigate this fascinating material system.

7.2: Future Steps: Identification of scattering mechanisms

The total mobility of CdO is result of multiple contributions. These contributions include acoustic, optical, ionized impurity, piezoelectric scattering [49, 157]. We can account for each of these mechanisms through Matthiessen's rule, which takes the sum of the inverse of each of these mobilities. The impact of adding NiO to these scattering mechanisms is unknown but the mobility of films decreases with added Ni composition; it is therefore important to study the scattering mechanisms across the composition range and identify the presence of new or disappearance of existing mechanisms.

There may be another scattering mechanism, namely alloy disorder scattering present. The strength of alloy scattering mechanism is related to the fluctuations of the CBM due to random atom distribution as well as the difference in atom size. Given that the endpoint compounds CdO and NiO have a CBM of > 3.3 eV, this effect could be very significant. Furthermore, the cation size difference between Cd^{2+} and Ni^{2+} suggests that this type of scattering will occur. The cation size and known scattering mechanisms of CdO are believed to be working in concert and give rise to contributions from scattering from phonons, alloy disorder, and ionized impurities.

It is necessary, and possible through variable temperature Hall effect experiments, to identify the present mechanisms through known mobility vs T relationships. The goal of such experiments would be to identify the scattering mechanism in $Ni_xCd_{1-x}O$ across the composition range through an analysis of dependence of the mobility on the temperature. This technique has been useful for identifying scattering mechanisms in systems such as CdO and ZnO amongst others [157].

7.3: Future Steps: Creation of application ready $Ni_xCd_{1-x}O$

Exploratory work on $Ni_xCd_{1-x}O$ paves the way for future experiments with an application basis. Experiments to address the enhanced absorption with the application of a negative bias and continued absorption with application of positive bias for example, could make $Ni_xCd_{1-x}O$ promising for electrochromic windows. Moreover, the films' stability in water could be investigated. The attractive location of CdO near the H^+/H_2 redox potential and the potential neutralization of surface charges in irradiated $Ni_xCd_{1-x}O$ make such studies interesting. And, p-type $Ni_xCd_{1-x}O$ could be incorporated into future p-n junction research.

The proposed studies are illustrative of an opportunity space rife with future studies on $Ni_xCd_{1-x}O$. Grounded in a foundation of basic properties and advanced knowledge of the physics behind this system, we can now begin to improve its electrical transport properties, manipulate its optical properties, and modify its electronic structure for applications. This dissertation ultimately moves $Ni_xCd_{1-x}O$ closer to being an industrially relevant metal-oxide.

Appendix A
Band offsets for semiconductors

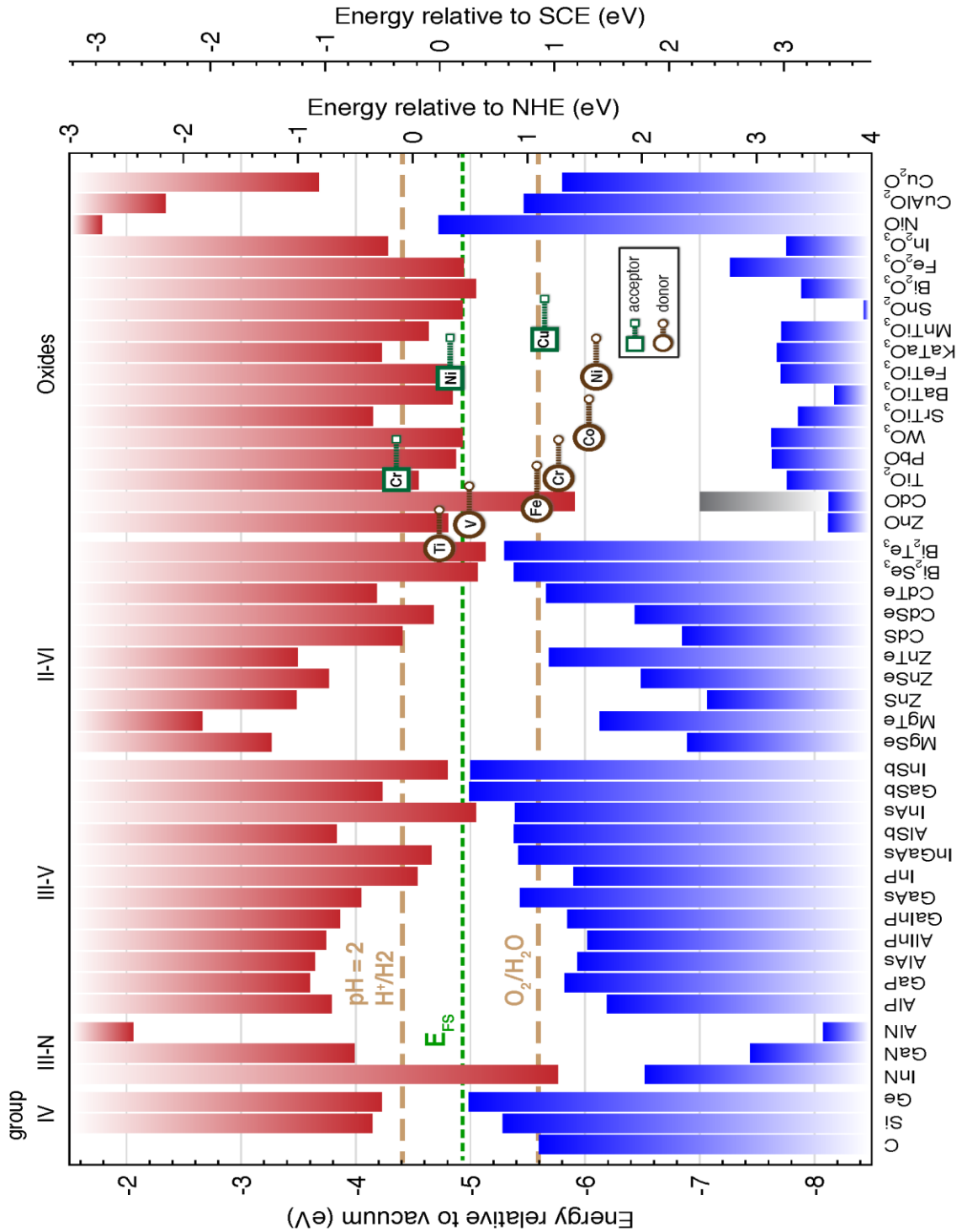

Figure A1: Band offsets for Groups IV, III-V, II-VI, and metal-oxide semiconductors with d *d*-level locations for TM-impurities and water splitting redox potentials. Adapted from References [19, 41, 42, 43, 49, 50, 52-53, 174, 180, and 211-213].

Appendix B

List of RF magnetron sputtered $Ni_xCd_{1-x}O$ films

RF magnetron sputtered films used for the initial structural, electrical transport, and optical characterization of $Ni_xCd_{1-x}O$												
Film Name	**Chemical Compound**	**Ambient**	**Heater %**	**T [C]**	**CdO**		**NiO**		**time [min]**	**thick [nm]**	**%Ni**	**%Cd**
709	NiO (Glass and Sapphire)	Ar	60	270	13	0	3	140	30	98	100	0
710	$Ni_xCd_{1-x}O$ (Glass and Sapphire)	Ar	60	270	13	15	3	140	30	104	95	5
711	$Ni_xCd_{1-x}O$ (Glass and Sapphire)	Ar	60	270	13	30	3	140	30	110	88.8	11.2
712	$Ni_xCd_{1-x}O$ (Glass and Sapphire)	Ar	60	270	13	45	3	140	30	123	82.5	17.5
713	$Ni_xCd_{1-x}O$ (Glass and Sapphire)	Ar	60	270	13	60	3	140	30	140	78	22
343	$Ni_xCd_{1-x}O$	Ar	60	270	13.5	10	3.5	140	60	178	97	3
327	$Ni_xCd_{1-x}O$	Ar	60	270	12	20	3.5	140	60	180	90	10
328	$Ni_xCd_{1-x}O$	Ar	60	270	12	40	3.5	140	60	220	80.8	19.2
329	$Ni_xCd_{1-x}O$	Ar	60	270	12	60	3.5	140	60	207	72	28
330	$Ni_xCd_{1-x}O$	Ar	60	270	6	60	3.5	140	40	203	58	42
331	$Ni_xCd_{1-x}O$	Ar	60	270	6	80	3.5	140	30	180	51	49
360	$Ni_xCd_{1-x}O$	Ar	60	270	6	90	3.8	140	30	216	43.4	56.6
332	$Ni_xCd_{1-x}O$	Ar	60	270	4	80	3.5	120	30	210	39.4	60.6
333	$Ni_xCd_{1-x}O$	Ar	60	270	4	100	3.5	120	30	244	35	65
334	$Ni_xCd_{1-x}O$	Ar	60	270	4	100	3.5	100	20	160	29	71
362	$Ni_xCd_{1-x}O$	Ar	60	270	4	100	3.5	110	25	240	27	73
335	$Ni_xCd_{1-x}O$	Ar	60	270	4	100	3.5	80	20	150	25	75
336	$Ni_xCd_{1-x}O$	Ar	60	270	4	100	3.5	60	20	134	16	84
361	$Ni_xCd_{1-x}O$	Ar	60	270	4	100	3.5	50	25	192	12	88
337	$Ni_xCd_{1-x}O$	Ar	60	270	4	100	3.5	40	20	130	10	89
363	$Ni_xCd_{1-x}O$	Ar	60	270	4	100	5	40	25	190	6.2	93.8
338	$Ni_xCd_{1-x}O$	Ar	60	270	4	100	3.5	20	20	110	3	97
278	CdO	Ar	60	270		100			30	135		100
733	$Ni_xCd_{1-x}O$	Ar	60	270	4	100	6	20	30	122	1.5	98.5
734	$Ni_xCd_{1-x}O$	Ar	60	270	4	100	6	40	20	160	29	71
735	$Ni_xCd_{1-x}O$	Ar	60	270	13	90	3	140	30	130	66	34
158	CdO	Ar	60	270	4	140	--	--	30	~300	0	100

RF magnetron sputtered films for XPS-UPS study													
Film Name	**Chemical Compound**	**Ambient**	**P [mTorr]**	**Heater %**	**T [C]**	**CdO**		**NiO**		**time [min]**	**thick [nm]**	**%Ni**	**%Cd**
						dist. (cm)	power (W)	dist. (cm)	power (W)			by RBS	by RBS
709	NiO	Ar	5	60	270	13	0	3	140	30	98	1	0
713	$Ni_xCd_{1-x}O$	Ar	5	60	270	13	60	3	140	30	140	0.78	0.22
330	$Ni_xCd_{1-x}O$	Ar	5	60	270	6	60	3.5	140	40	203	0.58	0.42
1097	$Ni_xCd_{1-x}O$	Ar	5	60	270	6	90	3.5	140	15	115	0.41	0.59
1094	$Ni_xCd_{1-x}O$	Ar	5	60	270	4	80	3.5	120	15	103	0.35	0.65
1096	$Ni_xCd_{1-x}O$	Ar	5	60	270	4	100	3.5	110	15	131	0.24	0.76
337	$Ni_xCd_{1-x}O$	Ar	5	60	270	4	100	3.5	40	20	130	0.1	0.9
338	$Ni_xCd_{1-x}O$	Ar	5	60	270	4	100	3.5	20	20	110	0.03	0.97
278	CdO	Ar	5	60	270	4	100	-	-	30	135	0	1
RF magnetron sputtered films for ion irradiation study													
278	CdO	Ar	5	60	270	4	100	-	-	30	135	0	1
335	$Ni_xCd_{1-x}O$	Ar	5	60	270	4	100	3.5	80	20	150	25	75
336	$Ni_xCd_{1-x}O$	Ar	5	60	270	4	100	3.5	60	20	134	16	84
337	$Ni_xCd_{1-x}O$	Ar	5	60	270	4	100	3.5	40	20	130	0.1	0.9
338	$Ni_xCd_{1-x}O$	Ar	5	60	270	4	100	3.5	20	20	110	0.03	0.97
733	$Ni_xCd_{1-x}O$	Ar	5	60	270	4	100	6	20	30	122	1.5	98.5
734	$Ni_xCd_{1-x}O$	Ar	5	60	270	4	100	6	40	20	160	29	71
1094	$Ni_xCd_{1-x}O$	Ar	5	60	270	4	80	3.5	120	15	103	0.35	0.65
1095	$Ni_xCd_{1-x}O$	Ar	5	60	270	4	80	3.5	120	15	129	0.28	0.72
1096	$Ni_xCd_{1-x}O$	Ar	5	60	270	4	100	3.5	110	15	131	0.24	0.76
1097	$Ni_xCd_{1-x}O$	Ar	5	60	270	6	90	3.5	140	15	115	0.41	0.59
1094	$Ni_xCd_{1-x}O$	Ar	5	60	270	4	80	3.5	120	15	103	0.35	0.65

RF magnetron sputtered films for Ar+O_2 study													
Ar+20% O_2													
Film Run	**Chemical Compound**	**Ambient**	**P [mTorr]**	**Heater %**	**T [C]**	**CdO**		**NiO**		**time [min]**	**thick [nm]**	**Ni(x)**	**Cd(x)**
						dist. (cm)	power (W)	dist. (cm)	power (W)			by RBS	by RBS
1139	NiO	Ar+ 20%O_2		60	270	-	-	3	140	30	37.2	1	0
1140	NiO	Ar+ 20% O_2		70	300	-	-	3	140	30	53	1	0
962	$Ni_xCd_{1-x}O$	Ar+ 20% O_2		70	300			3.5	140	30	43.9	0.989	0.011
1141	$Ni_xCd_{1-x}O$	Ar+ 20% O_2		70	300	4.5	20	3	120	30		95	5
915	$Ni_xCd_{1-x}O$	Ar+ 20% O_2		70	300	1	0	2	140	30	62.5	0.94	0.06
916	$Ni_xCd_{1-x}O$	Ar+ 20% O_2		70	300	13	15	3	140	30	67.1	0.88	0.12
917	$Ni_xCd_{1-x}O$	Ar+ 20% O_2		70	300	13	30	3	140	30	91	0.72	0.28
918	$Ni_xCd_{1-x}O$	Ar+ 20% O_2		70	300	13	45	3	140	30	116	0.6	0.4
919	$Ni_xCd_{1-x}O$	Ar+ 20% O_2		70	300	13	60	3	140	30	163	0.51	0.49
920	$Ni_xCd_{1-x}O$	Ar+ 20% O_2		70	300	13	60	3	140	30	80	0.5	0.5
921	$Ni_xCd_{1-x}O$	Ar+ 20% O_2		70	300	13	75	3	140	30	244	0.48	0.52
922	$Ni_xCd_{1-x}O$	Ar+ 20% O_2		70	300	4.5	80	3	140	30	344	0.173	0.827
923	$Ni_xCd_{1-x}O$	Ar+ 20% O_2		70	300	4.5	100	3	120	30	493	0.15	0.85
965	$Ni_xCd_{1-x}O$	Ar+ 20% O_2		70	300	5	100	3	120	30	21.5	0.083	0.917
189	CdO	Ar+ 20% O_2		70	300	4	100	-	-	25	180	0	1
75% Cd, 25% Ni													
335	$Ni_xCd_{1-x}O$	Ar	5	60	270	4	100	3.5	80	20	150	25	75
1254	$Ni_xCd_{1-x}O$	Ar+ 50% O_2		60		6	90	3.1	140		120	0.204	0.796
1246	$Ni_xCd_{1-x}O$	10% O_2	5.8			6	90	3.1	140				
1245	$Ni_xCd_{1-x}O$	Ar+20%O2		60	270	6	3.1	90	140	30%	130	0.25	0.75
R1410	$Ni_xCd_{1-x}O$	100% O2											
NiO													
320	NiO	Ar+ 20% O_2	5	30	150	-	-	3.5	140	60	73	1	0
321	NiO	Ar+10% O_2	5	30	150	-	-	3.5	140	90	117	1	0
324	NiO	Ar	5	30	150	-	-	3.5	140	90	293	1	0
1326	NiO	100% O_2	5	60	270			4	140	30	31	1	0
1327	NiO	Ar+50% O_2	5	60	270			4	20	30	28.2	1	0
CdO													
278	CdO	Ar	5	60	270	4	100	-	-	30	135	0	1
232	CdO	Ar+10% O_2	5.1	60	270	4	100	-	-	30	242	0	1
189	CdO	Ar+ 20% O_2		70	300	4	100			25	180	0	1
R1363	CdO	Ar+ 50% O_2	5	60		6	120			20	5	0	1
1364	CdO	100% O_2	5	60		6	120			21	200	0	1
52% Ni, 48% Cd													
1328	$Ni_xCd_{1-x}O$	Ar	5	60	270	6	80	4	140	30	218	0.52	0.48
1366	$Ni_xCd_{1-x}O$	100% O_2	5	60	270	13	60	3	140	15	10	0.52	0.48
1412	$Ni_xCd_{1-x}O$	50% O_2	5	60	270	13	60	3	140	30		0.52	0.48
919	$Ni_xCd_{1-x}O$	20% O_2	5	70		13	60	3	140	30	163	0.52	0.48
1411	$Ni_xCd_{1-x}O$	50% O_2				6	32.25	4	140	30		0.52	0.48
1366	$Ni_xCd_{1-x}O$	100% O_2				13	60	3	140	30		0.52	0.48
62% Ni, 38% Cd													
1349	$Ni_xCd_{1-x}O$	20% O_2		60	270	6	32.25	4	140	30	10	0.62	0.38
1417	$Ni_xCd_{1-x}O$	50% O_2		60	270	13	48.5	3	140	30		0.62	0.38

Appendix C

SIMNRA determination of thickness and composition

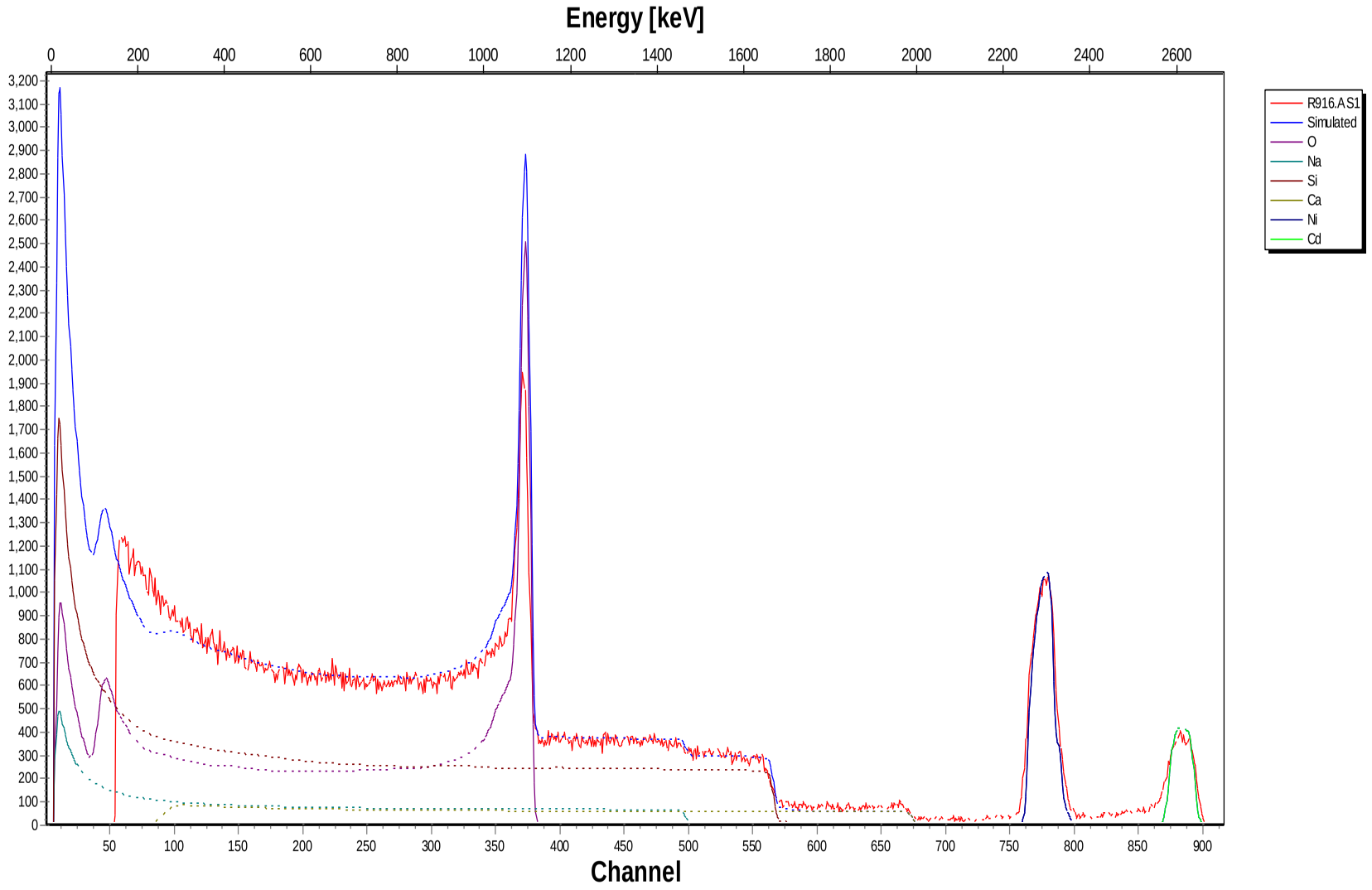

Figure A2: SIMNRA models raw data obtained from an RBS spectrum to determine film thickness and composition. In the following spectra, the height, width, and position of the peaks directly correspond to the composition, thickness, and element contained within an analyzed film. This example demonstrates a fitting for a film grown on a glass substrate. For R916, an Ar+20% O_2 sputtered $Ni_xCd_{1-x}O$ film probed with a 3.04 MeV He^{++} beam, the thickness, stoichiometry, and Ni: Cd in terms of percent are 67.1 nm, Ni 0.385 Cd 0.115 O 0.565, and 88% Ni: 12% Cd respectively.

Appendix D

Grain sizes, extended defects, and scattering mechanisms discussion for $Ni_xCd_{1-x}O$

D1: Discussion of extended defects in $Ni_xCd_{1-x}O$

The size mismatch between Ni^{2+} and Cd^{2+} and the small calculated grain size in $Ni_xCd_{1-x}O$ by XRD raises questions about each film's homogeneity and extended defects. These questions center on the presence of dislocations and grain boundaries to accommodate the film synthesis across the composition range. While this dissertation primarily discusses the impact of point defects it is believed that extended defects, such as dislocations and grain boundaries, introduce unintended consequences on the electrical transport and optical properties reported in Chapter 4. [16]

Dislocations form to mitigate the strain on the system due to the lattice constant differences between the film and substrate [32, 38]. In $Ni_xCd_{1-x}O$ films deposited on glass, dislocations could accommodate the cation size difference between Ni^{2+} and Cd^{2+} and thus lower the strain energy in the system. Generally, these dislocations can act as scattering centers. Furthermore, given that dislocations can act as trap centers, it is believed to influence the states in the midgap for a material. The dangling bonds in dislocations can act as electron acceptors and reduce the number of free carriers. Grain boundaries can also introduce midgap trap states and the cation mismatch can lead to segregation of a solute species to the grains.

The scattering from extended defects is typically observed in the Group-III nitrides, a system that is, as described in Chapter 2, analogous to the Group-II oxides. Typically, scattering mechanisms are governed by a film's measured electron concentration. In InN and GaN films, dislocation densities on the order of 10^9 cm^{-2} are the most prevalent scattering mechanisms at low electron concentrations of 10^{16} cm^{-3}. This mechanism is believed to contribute background electrons that are responsible for the inability to reach higher theoretical concentrations.

By comparison, the electron concentrations of $Ni_xCd_{1-x}O$ films are 2-4 orders of magnitude (10^{18} cm^{-3} -10^{20} cm^{-3}) higher than that of InN films. As a result, dislocation scattering is neither an essential scattering mechanism in CdO nor $Ni_xCd_{1-x}O$. At these concentrations other mechanisms, such as phonon (acoustic and optical) and ionized impurity scattering, that can be measured (Section 7.2) dominate. **Table A1** shows the electron concentrations from several studies vis a vis this study.

Table A1: Comparison of the electron concentrations for InN, GaN, and $Ni_xCd_{1-x}O$ films in relation to extended defect scattering in each film.

Films	*Electron Concentration, n (cm^{-3})*
InN on GaN	10^{16} -10^{17}- Ref. [207]
n-type GaN on Sapphire	10^{16}- 10^{17} –Ref. [208]
$Ni_xCd_{1-x}O$ on Glass	10^{18}-10^{20}- This study

The mean free path of a carrier with respect to grain size is a measure of grain boundary scattering in a transparent and conducting oxide thin film. If the mean free path is less than the grain size, then the effects of scattering due to grain boundaries are less important compared to other scattering mechanisms. This mean free path, l, is calculated

[16] It is important to note that there is no room temperature phase diagram for this system and therefore no working prediction for how this system will behave upon the addition of Ni.

with a threshold electron concentration, n, and the corresponding mobility at this concentration, μ, through the equation [37, 157]:

$$l = \left(\frac{h}{2e}\right)\left(\frac{3n}{\pi}\right)^{\frac{1}{3}}\mu\,. \qquad \text{(A1)}$$

However, grain boundary scattering was found not to be a dominant scattering mechanism in several TCO thin films. Previously, the mean free path for ZnO, ZnO:Al, CdO, and ITO thin films were all less than the calculated grain size. The threshold concentration for CdO has not been experimentally determined, but it has been determined for other materials. It has been determined from Al-doped ZnO (1-3 at %) that the carrier mean free path is significantly less (l=5nm) than that of a grain (45 nm) and is thus an extremely small contributor to the scattering [209]. Ionized defects and neutral defects in the intermediate temperature ranges are believed to be responsible for limiting mobility in these films. This result has also been found in other articles that showed that the mean free path of electrons is lower than the grain size [210]. The most relevant studies to a CdO system are those on CdO that also concluded that grain boundary scattering is not a factor for polycrystalline films.

A prominent study by Metz *et al.* studied the scattering mechanisms in CdO thin films. There were three film sets: grown on glass, MgO (100) and slow growth on MgO (100) through the slow release of Ar gas into the MOCVD chamber [157]. All three film sets were grown with different substrate temperatures ranging from 300°C to 412°C. Three types of factors explain the difference between CdO grown on MgO and glass thin films:

1. crystallinity difference
2. grain boundary scattering, which scales with the grain size
3. a difference in electron concentration

An analysis between the glass and fast-growth films on MgO shows that both have similar grain size and that the electrical transport properties for the MgO grown set were enhanced. The difference between the two films were shown to be a difference in crystallinity—the ones grown on glass had voids, which limit carrier transport, which the MgO-grown films have dense microstructures. The mean free path of films is 18 nm, much less than the 100 nm for CdO on MgO. **Table A2** shows the carrier mean free path versus the grain size for the Tahar and Metz studies.

Table A2: Comparison of the mean free path with the grain size for Al-doped ZnO and CdO films.

Material	*Mean free path (nm)*	*Grain Size (nm)*
ZnO:Al [209]	~5.5	~45
CdO [157]	~18	~100

In $Ni_xCd_{1-x}O$, a similar calculation was conducted and the results are displayed in **Table A3** with AFM determinations of grain size included. The mean free path of each film with respect to the grain size is lower—the carriers will not reach the grain boundaries and will be scattered by other mechanisms instead. The oxygen vacancies that are ionized and scatter carriers strongly are compensated, resulting in neutral defects, can scatter carriers for example. Neutral impurities from inactivated impurities or activated holes could also

be at play. Another mechanism could be the alloy disorder scattering stemming from the size difference in cation radius. An additional mechanism could be the change in the dielectric constant from CdO to NiO, which reduces the ability to screen charges.

Table A3: Comparison of the mean free path with the grain size for $Ni_xCd_{1-x}O$ films.

Ni composition (%)	*Mean Free Path (nm)*	*Grain Size by XRD (nm)*	*Grain Size by AFM (nm)*
40	~0.05	~19	~40
35	~0.13	~20	~40
27	~12	~19	~40
17	~17	~18	~40
0	~13	~15	~25

D2: Discussion of element segregation in $Ni_xCd_{1-x}O$

The segregation of elements at grain boundaries is another issue that could occur given the small grain sizes and non-equilibrium method of growing these films. Typically, this is expected to would manifest itself in my XRD, Hall effect, and optical absorption data. These data would show distinct regions—NiO and CdO—in cases of extreme segregation. However, the data received on these films show no such features.

During evaluation of my XRD patterns I looked for three features: phase separation, peak shift deviations from Vegard's law, and the FWHM of each peak. Some of these findings are reported in Chapter 4. First, two peaks corresponding to two distinct regions are unobserved –thus I can rule out phase separation in my films. This feature is seen in $Cd_XZn_{1-x}O$ films however [74]. And this is of importance because once the phase transition from rocksalt to wurtzite occurs, the mobility and electron concentration both decrease. Secondly, the alloy's (220) peak, which shifts monotonically with Ni composition to higher 2θ angles, are within agreement of Vegard's Law. Thirdly, the (220) peaks for pure NiO and CdO phases reside at 62.5° and 54.9° respectively according to the literature, which is later confirmed by my experimental data. Furthermore, each 220 peak is distinct and identified at positions within the range of 54.9° and 62.5°. The Lorentizan and Gaussian fits to the FWHM of each (220) peak shows that the width is within the range of 0.5 to 0.6 degrees. If the film was not a solid solution for instance, then I would identify a peak with a FWHM that exceeds this value. The MgO-CdO system, by comparison, which has a similar cation size mismatch to the NiO-CdO system has a monotonic shift in the (220) peaks but also becomes amorphous with added Mg [75]. The accumulation of evidence from XRD patterns suggest that $Ni_xCd_{1-x}O$ is a solid solution across the composition range and the study of extended defects was therefore not pursued.

Overall, a comparison with literature, investigation of XRD peaks, and calculations demonstrate that homogeneity and extended defects are less important issues within $Ni_xCd_{1-x}O$ films. Nevertheless, experimental methods such as TEM to investigate phase segregation, SEM to further probe the crystalline grain size, and variable-temperature Hall effect to identify the scattering mechanisms present could be employed in future studies to confirm the conclusions drawn in this investigation.

Appendix E

Mathematica code for modeling carrier filling effects

Options

```
ClearAll["Global`*"]
```

Data Import

```
SetDirectory["/Users/Christopher
Francis/Desktop/Research/Corrections for Shifts in Energy"];
ntable =Import["CdNiOdata.txt","TSV"]
```

Constants

General

```
charge =1.6 10^-19;
c = 2.997 10^8; (*cgs units*)
masse=9.109 10^-28 (*g*);
chargeerg=4.8 10^-10 (*charge on electron in ergs*);
eVerg=1.602 10^-12; (*converts eV to erg*)
hbar= 1.0546 10^-27 (* erg-s *);
kbeV=8.617 10^-5;(*Boltzmann constant,eV/K*)
kb=1.38 10^-16;(*Boltzmann constant,erg/K*)
T=300;(* K *)
```

Materials-specific constants for CdO and NiO

```
ε0CdO=21.9;(*static dielectric constant*);
ε0NiO=11.7;(*static dielectric constant*);
mcCdO=0.21;
mcNiO=2;

ab=ε0/mc 0.5*10^-8;(*bohr radius, in cm*);

mh=100;(*hole effective mass/mass electron*)
 abNiO=ε0NiO/mcNiO 0.5*10^-8
 2.925×10^-8
 abCdO=ε0CdO/mcCdO 0.5*10^-8
 5.21429×10^-7
```

Equations to calculate carrier-filling effects

Fermi level integral to determine Burstein-Moss Shifts

```
kdisp[z_]:=Sqrt[(egap eVerg masse)/hbar^2+((egap eVerg
masse)/(hbar^2 mc))+((2 kb masse T z)/hbar^2)-1/(hbar^4 mc)
Sqrt[egap eVerg hbar^4 masse^2 (egap eVerg+2 egap eVerg mc+egap
eVerg mc^2+4 kb mc T z)]];
(*z is energy in ergs*)
nequation[efermi_,limit_]:=Re[1/(3Pi^2) NIntegrate[(Exp[x-
efermi/(kbeV T)]/(1+Exp[x-efermi/(kbeV T)])^2)
kdisp[x]^3,{x,0,limit}]];
(*x is reduced energy*)
```

Correlation and Renormalization Effects

```
k[n_]:=(3*Pi^2 n)^1/3
λ[n_]:=2√(3 Pi^2 n^1/3 / Pi ab)
(*thomas fermi screening parameter*)

EErenorm[k_,λ_]:=(-((2*chargeerg^2 *k)/(Pi*ε0))-(chargeerg^2
*λ)/(2*ε0) (1-4/Pi Tanh[k/λ])) 1/eVerg(*electron-electron
correlation shift*)

IErenorm[n_]:=(-((chargeerg*hbar)/2) √(Pi^3 n / 0 mc masse) )
1/eVerg(*ion-electron renormalization shift*)

vb[k_]:=(hbar^2*k^2)/(2 (mh masse)) 1/eVerg
(*Absorption edge energy shift due to v.b. dispersion*)
```

Calcuation & Output

This loop takes each concentration value and calculates Fermi level, e-e and i-e renormalization parameters, and conc-induced energy shift in abs edge due to v.b. dispersion

```
 outputtable={};
For[dd=1,dd≤Length[ntable],dd++,{comp=ntable[[dd,1]],egap=ntable[
[dd,2]],n=ntable[[dd,3]],ε0=ε0NiO(1-
comp)+ε0CdO*(comp),mc=mcNiO(1-comp)+mcCdO*(comp)};
 (*Finding the Fermi energy from n*)
 elow=0;(*low guess for Fermi energy,in eV*)
 ainc=0.50;(*energy difference between high and low guesses,in
eV*)
 ehigh=elow+ainc;(*high guess,in eV*)
 nlow=nequation[elow,600];
 nhigh=nequation[ehigh,600];(*back calculations of n based on
elow and ehigh*)
 For[d=1,d<40,d++ If[nhigh<n,elow=ehigh;ehigh=ehigh+ainc/2];
  If[nlow>n,ehigh=elow;elow=elow-ainc/2];
  If[nlow<n&&nhigh>n,ainc=ainc/2;elow=elow+ainc/2;ehigh=ehigh-
ainc/2];nlow=nequation[elow,400];
  nhigh=nequation[ehigh,400];];
(*End loop to find Fermi energy from n*)

 Ef=(elow+ehigh)/2;
(*Fermi energy w.r.t c.b. edge, in eV*)

 ee=EErenorm[k[n],λ[n]];
```

```
(*e-e renormalization shift in eV, should be negative*)

 ie=IErenorm[n];
(*i-e renormalization shift in eV, should be negative*)
 (*Evb=vb[k[n]];(*shift in abs edge due to v.b. dispersion,
should be positive for normal, positive mass, hole
dispersion*)*)

 AppendTo[outputtable,{comp,egap,n,mc,Ef,ee,ie}];
 Print["comp: ",comp," n: ",n," Ef: ",Ef," ee: ",ee,"ie: ",ie];]
 Export["Outputtable.txt",outputtable,"TSV"];
```

Appendix F
SRIM modeling for ion irradiation

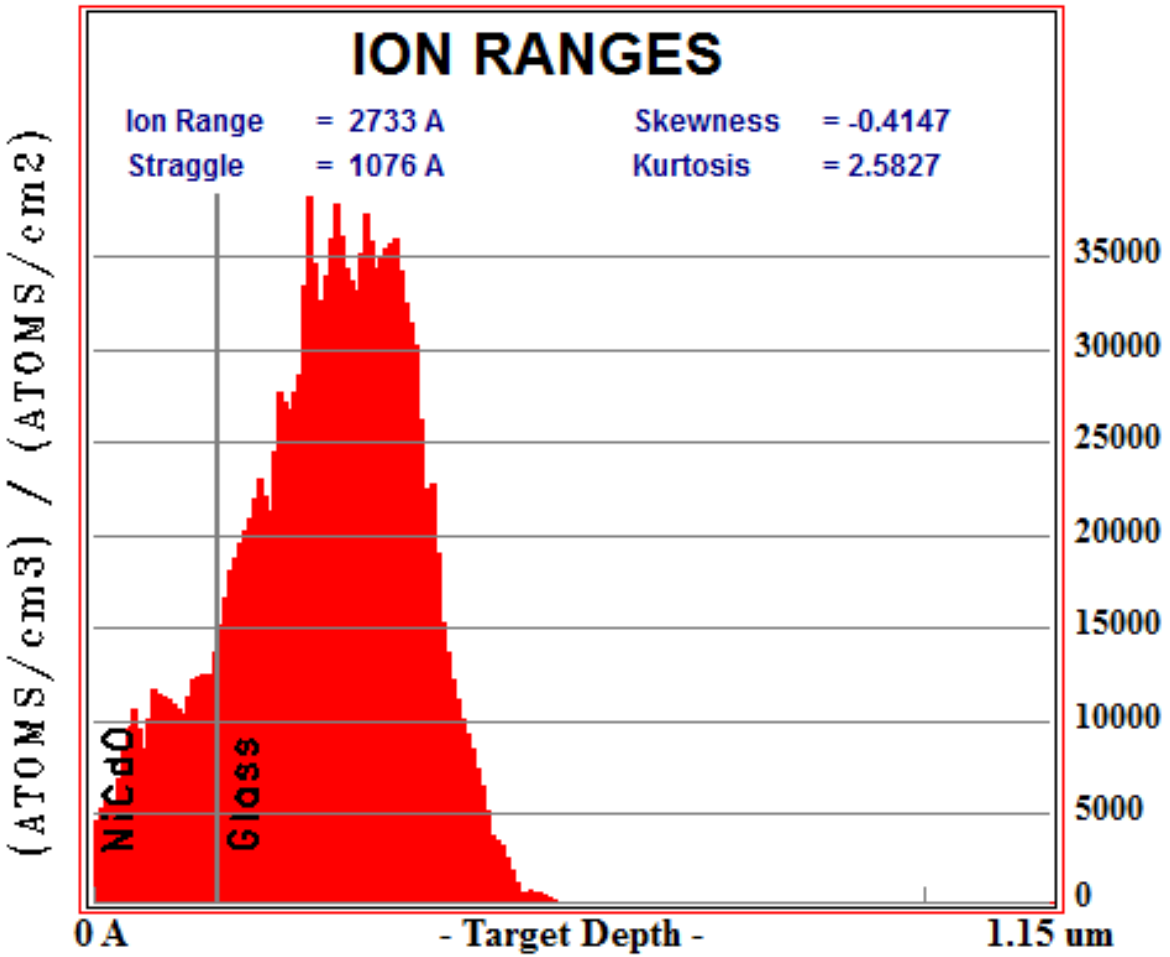

Figure A3: Predicted ion implanted depth for $Ni_xCd_{1-x}O$ sample with 24% Ni and 150 nm thickness. For every sample used for ion irradiation experiments, it is important to have a small thickness to avoid ion implantation within the sample. This graph shows that most of the ions hitting a sample will become implanted in the glass substrate. Thus we can be assured of uniform defect generation without implantation effects in given films.

Appendix G

MATLAB code for modeling band anticrossing behavior

Credit: Maribel Jaquez for drafting and executing BAC simulations

```
%%
clc
clear
dbstop if error
%% Ion irradiation data
ni = [0, 0.015, 0.04, 0.1, 0.11, 0.16, 0.24, 0.28, 0.35, 0.41];
energy =[-5.84341, -5.77776, -5.62958, -5.38704, -5.44579, -
5.22434, -5.05889,-5.08429,-4.96298, -4.7495];
%% Bandgap data
nieg= [0, 0.015, 0.04, 0.062, 0.11, 0.12, 0.16, 0.24, 0.25,
0.27, 0.28, 0.35, 0.394, 0.41, 0.434, 0.51, 0.58, 0.66, 0.72,
0.78, 0.81, 0.825, 0.888, 0.90, 0.97, 1];
bandgap=[2.2, 2.49, 2.30, 2.41, 2.45, 2.50, 2.63, 2.726, 2.73,
2.87, 2.84, 3.04, 2.94, 3.13, 3.15, 3.17, 3.30, 3.46, 3.35,
3.49, 3.46, 3.53, 3.55, 3.48, 3.51, 3.6];
%%
x=0.2;
Ec_CdO = -5.8;
Ec_NiO = -1.5 ;
Ev_CdO = -8.0;
Ev_NiO= -5.1;

Eni = Ec_CdO- 0.3;   %previously -0.2        % Ni donor level on
absolute scale with reference to CdO VBE
Eni_1 = Ec_CdO+ 1.1;   %previously +0.9        % Ni acceptor
level on absolute scale with reference to CdO CBE
mestarCdO = 0.21; %[#] electron effective mass of CdO: ROCKSALT
mhstarCdO= 0.5; %[#] light hole effective mass of CdO: ROCKSALT
mestarNiO = 2.0; %[#] electron effective mass of NiO: Rocksalt,
rough estimate
mhstarNiO= 0.86; %[#] hole effective mass of upper VB of  NiO:
Rocksalt

%Counpling parameter dependance of the Te concentration
C10 = .75;
% Coupling parameter for CdO
C20 = 1;
mat1_name = 'CdO';
mat2_name = 'NiO';
alloy_name = 'CdNiO';

C1= @(x) C10.*(1-x);
C2= @(x) C20.*(1-x);
%% applying all nio, cdo parameters
```

```
Ec_mat1 = Ec_CdO;
Ev_mat1 = Ev_CdO;

Ec_mat2 = Ec_NiO;
Ev_mat2 = Ev_NiO;

Ec_level = Eni;
Ec_level_1 = Eni_1;

mestar_mat1 = mestarCdO;
mhstar_mat1 = mhstarCdO;

mestar_mat2 = mestarNiO;
mhstar_mat2 = mhstarNiO;



%% constants
me = 9.109382e-31; %[kg] electron rest mass
hbar = 6.626e-34/(2*pi); %[J.s] Planck's Constant Reduced
eV = 1.6e-19; %[J] electron volt

%% Effective masses: x dependant
mestar = @(x) mestar_mat1.*(1-x) + mestar_mat2.*x;
mhstar = @(x) mhstar_mat1.*(1-x) + mhstar_mat2.*x;

hbarovermeffelectron =
@(x)(hbar).^2./(2.*me.*mestar(x))./eV.*(100^2);
hbarovermeffhole =
@(x)(hbar).^2./(2.*me.*mhstar(x))./eV.*(100^2);


E_k = @(k, x) Ec_mat1.*(1-x) + x.*Ec_mat2 ...
                + k.^2.*hbarovermeffelectron(x); %Econduction
Band, linear
% host Evalence band
Evalence = @(k, x) Ev_mat1.*(1-x) + x.*Ev_mat2 ...
            - k.^2.*hbarovermeffhole(x);         %Valence Band,
linear

% VBAC
Eminus_mat2 = @(k, C, x, Ex) .5.*((Ex+Evalence(k, x)) ...
    - sqrt((Evalence(k, x)- Ex).^2+4.*C.^2.*(x)));    %VBAC- for
Ec_lv & mat2
Eplus_mat2 = @(k, C, x, Ex) .5.*((Ex+Evalence(k, x)) ...
    + sqrt((Evalence(k, x) - Ex).^2+4.*C.^2.*(x)));   %VBAC+ for
Ec_lv & mat2
```

```
E_sol1= @(k,x, E1, E2) E1./3 + E2./3 + E_k(k,x)./3 ...
    + (((((E1 + E2 + E_k(k,x)).*(- x.*C1(x).^2 - x.*C2(x).^2 +
E1.*E2 + E1.*E_k(k,x)...
    + E2.*E_k(k,x)))/6 - (E1 + E2 + E_k(k,x)).^3./27 ...
    - (E1.*E2.*E_k(k,x))./2 + (C1(x).^2.*E2.*x)./2 +
(C2(x).^2.*E1.*x)./2).^2 ...
    - ((C1(x).^2.*x)./3 + (C2(x).^2.*x)./3 + (E1 + E2 +
E_k(k,x)).^2./9 ...
    - (E1.*E2)./3 - (E1.*E_k(k,x))./3 -
(E2.*E_k(k,x))./3).^3).^(1/2) ...
    + (E1 + E2 + E_k(k,x)).^3./27 - ((E1 + E2 + E_k(k,x)).*(-
x.*C1(x).^2 ...
    - x.*C2(x).^2 + E1.*E2 + E1.*E_k(k,x) + E2.*E_k(k,x))).*/6
...
    + (E1.*E2.*E_k(k,x))./2 - (C1(x).^2.*E2.*x)./2 -
(C2(x).^2.*E1.*x)./2).^(1/3)...
    + ((C1(x).^2.*x)./3 + (C2(x).^2.*x)./3 + (E1 + E2 +
E_k(k,x)).^2./9 ...
    - (E1.*E2)./3 - (E1.*E_k(k,x))./3 ...
    - (E2.*E_k(k,x))./3)./(((((E1 + E2 + E_k(k,x)).*(-
x.*C1(x).^2 ...
    - x.*C2(x).^2 + E1.*E2 + E1.*E_k(k,x) + E2.*E_k(k,x))).*/6
...
    - (E1 + E2 + E_k(k,x)).^3./27 - (E1.*E2.*E_k(k,x))./2 ...
    + (C1(x).^2.*E2.*x)./2 + (C2(x).^2.*E1.*x)./2).^2 -
((C1(x).^2.*x)./3 ...
    + (C2(x).^2.*x)./3 + (E1 + E2 + E_k(k,x)).^2./9 -
(E1.*E2)./3 ...
    - (E1.*E_k(k,x))./3 - (E2.*E_k(k,x))./3).^3).^(1/2) ...
    + (E1 + E2 + E_k(k,x)).^3./27 - ((E1 + E2 + E_k(k,x)).*(-
x.*C1(x).^2 ...
    - x.*C2(x).^2 + E1.*E2 + E1.*E_k(k,x) + E2.*E_k(k,x))).*/6
...
    + (E1.*E2.*E_k(k,x))./2 - (C1(x).^2.*E2.*x)./2 -
(C2(x).^2.*E1.*x)./2).^(1/3);
E_sol2= @(k,x, E1, E2) E1./3 + E2./3 + E_k(k,x)./3 -
(3.^(1/2).*(((((((E1 + E2 + E_k(k,x)).*(- x.*C1(x).^2 -
x.*C2(x).^2 + E1.*E2 + E1.*E_k(k,x) + E2.*E_k(k,x))).*/6 - (E1 +
E2 + E_k(k,x)).^3./27 - (E1.*E2.*E_k(k,x))./2 +
(C1(x).^2.*E2.*x)./2 + (C2(x).^2.*E1.*x)./2).^2 -
((C1(x).^2.*x)./3 + (C2(x).^2.*x)./3 + (E1 + E2 +
E_k(k,x)).^2./9 - (E1.*E2)./3 - (E1.*E_k(k,x))./3 -
(E2.*E_k(k,x))./3).^3).^(1/2) + (E1 + E2 + E_k(k,x)).^3./27 -
((E1 + E2 + E_k(k,x)).*(- x.*C1(x).^2 - x.*C2(x).^2 + E1.*E2 +
E1.*E_k(k,x) + E2.*E_k(k,x))).*/6 + (E1.*E2.*E_k(k,x))./2 -
(C1(x).^2.*E2.*x)./2 - (C2(x).^2.*E1.*x)./2).^(1/3) -
```

```
((C1(x).^2.*x)./3 + (C2(x).^2.*x)./3 + (E1 + E2 +
E_k(k,x)).^2./9 - (E1.*E2)./3 - (E1.*E_k(k,x))./3 -
(E2.*E_k(k,x))./3)./(((((E1 + E2 + E_k(k,x)).*(- x.*C1(x).^2 -
x.*C2(x).^2 + E1.*E2 + E1.*E_k(k,x) + E2.*E_k(k,x))).*/6 - (E1 +
E2 + E_k(k,x)).^3./27 - (E1.*E2.*E_k(k,x))./2 +
(C1(x).^2.*E2.*x)./2 + (C2(x).^2.*E1.*x)./2).^2 -
((C1(x).^2.*x)./3 + (C2(x).^2.*x)./3 + (E1 + E2 +
E_k(k,x)).^2./9 - (E1.*E2)./3 - (E1.*E_k(k,x))./3 -
(E2.*E_k(k,x))./3).^3).^(1/2) + (E1 + E2 + E_k(k,x)).^3./27 -
((E1 + E2 + E_k(k,x)).*(- x.*C1(x).^2 - x.*C2(x).^2 + E1.*E2 +
E1.*E_k(k,x) + E2.*E_k(k,x))).*/6 + (E1.*E2.*E_k(k,x))./2 -
(C1(x).^2.*E2.*x)./2 - (C2(x).^2.*E1.*x)./2).^(1/3)).*1i)./2 -
((((E1 + E2 + E_k(k,x)).*(- x.*C1(x).^2 - x.*C2(x).^2 + E1.*E2
+ E1.*E_k(k,x) + E2.*E_k(k,x))).*/6 - (E1 + E2 + E_k(k,x)).^3./27
- (E1.*E2.*E_k(k,x))./2 + (C1(x).^2.*E2.*x)./2 +
(C2(x).^2.*E1.*x)./2).^2 - ((C1(x).^2.*x)./3 + (C2(x).^2.*x)./3
+ (E1 + E2 + E_k(k,x)).^2./9 - (E1.*E2)./3 - (E1.*E_k(k,x))./3 -
(E2.*E_k(k,x))./3).^3).^(1/2) + (E1 + E2 + E_k(k,x)).^3./27 -
((E1 + E2 + E_k(k,x)).*(- x.*C1(x).^2 - x.*C2(x).^2 + E1.*E2 +
E1.*E_k(k,x) + E2.*E_k(k,x))).*/6 + (E1.*E2.*E_k(k,x))./2 -
(C1(x).^2.*E2.*x)./2 - (C2(x).^2.*E1.*x)./2).^(1/3)./2 -
((C1(x).^2.*x)./3 + (C2(x).^2.*x)./3 + (E1 + E2 +
E_k(k,x)).^2./9 - (E1.*E2)./3 - (E1.*E_k(k,x))./3 -
(E2.*E_k(k,x))./3)./(2.*((((E1 + E2 + E_k(k,x)).*(- x.*C1(x).^2
- x.*C2(x).^2 + E1.*E2 + E1.*E_k(k,x) + E2.*E_k(k,x))).*/6 - (E1
+ E2 + E_k(k,x)).^3./27 - (E1.*E2.*E_k(k,x))./2 +
(C1(x).^2.*E2.*x)./2 + (C2(x).^2.*E1.*x)./2).^2 -
((C1(x).^2.*x)./3 + (C2(x).^2.*x)./3 + (E1 + E2 +
E_k(k,x)).^2./9 - (E1.*E2)./3 - (E1.*E_k(k,x))./3 -
(E2.*E_k(k,x))./3).^3).^(1/2) + (E1 + E2 + E_k(k,x)).^3./27 -
((E1 + E2 + E_k(k,x)).*(- x.*C1(x).^2 - x.*C2(x).^2 + E1.*E2 +
E1.*E_k(k,x) + E2.*E_k(k,x))).*/6 + (E1.*E2.*E_k(k,x))./2 -
(C1(x).^2.*E2.*x)./2 - (C2(x).^2.*E1.*x)./2).^(1/3));
E_sol3= @(k,x, E1, E2) E1./3 + E2./3 + E_k(k,x)./3 +
(3.^(1/2).*((((((E1 + E2 + E_k(k,x)).*(- x.*C1(x).^2 -
x.*C2(x).^2 + E1.*E2 + E1.*E_k(k,x) + E2.*E_k(k,x))).*/6 - (E1 +
E2 + E_k(k,x)).^3./27 - (E1.*E2.*E_k(k,x))./2 +
(C1(x).^2.*E2.*x)./2 + (C2(x).^2.*E1.*x)./2).^2 -
((C1(x).^2.*x)./3 + (C2(x).^2.*x)./3 + (E1 + E2 +
E_k(k,x)).^2./9 - (E1.*E2)./3 - (E1.*E_k(k,x))./3 -
(E2.*E_k(k,x))./3).^3).^(1/2) + (E1 + E2 + E_k(k,x)).^3./27 -
((E1 + E2 + E_k(k,x)).*(- x.*C1(x).^2 - x.*C2(x).^2 + E1.*E2 +
E1.*E_k(k,x) + E2.*E_k(k,x))).*/6 + (E1.*E2.*E_k(k,x))./2 -
(C1(x).^2.*E2.*x)./2 - (C2(x).^2.*E1.*x)./2).^(1/3) -
((C1(x).^2.*x)./3 + (C2(x).^2.*x)./3 + (E1 + E2 +
E_k(k,x)).^2./9 - (E1.*E2)./3 - (E1.*E_k(k,x))./3 -
(E2.*E_k(k,x))./3)./(((((E1 + E2 + E_k(k,x)).*(- x.*C1(x).^2 -
```

```
x.*C2(x).^2 + E1.*E2 + E1.*E_k(k,x) + E2.*E_k(k,x))./6 - (E1 +
E2 + E_k(k,x)).^3./27 - (E1.*E2.*E_k(k,x))./2 +
(C1(x).^2.*E2.*x)./2 + (C2(x).^2.*E1.*x)./2).^2 -
((C1(x).^2.*x)./3 + (C2(x).^2.*x)./3 + (E1 + E2 +
E_k(k,x)).^2./9 - (E1.*E2)./3 - (E1.*E_k(k,x))./3 -
(E2.*E_k(k,x))./3).^3).^(1/2) + (E1 + E2 + E_k(k,x)).^3./27 -
((E1 + E2 + E_k(k,x)).*(- x.*C1(x).^2 - x.*C2(x).^2 + E1.*E2 +
E1.*E_k(k,x) + E2.*E_k(k,x)))./6 + (E1.*E2.*E_k(k,x))./2 -
(C1(x).^2.*E2.*x)./2 - (C2(x).^2.*E1.*x)./2).^(1/3)).*1i)./2 -
(((((E1 + E2 + E_k(k,x)).*(- x.*C1(x).^2 - x.*C2(x).^2 + E1.*E2
+ E1.*E_k(k,x) + E2.*E_k(k,x)))./6 - (E1 + E2 + E_k(k,x)).^3./27
- (E1.*E2.*E_k(k,x))./2 + (C1(x).^2.*E2.*x)./2 +
(C2(x).^2.*E1.*x)./2).^2 - ((C1(x).^2.*x)./3 + (C2(x).^2.*x)./3
+ (E1 + E2 + E_k(k,x)).^2./9 - (E1.*E2)./3 - (E1.*E_k(k,x))./3 -
(E2.*E_k(k,x))./3).^3).^(1/2) + (E1 + E2 + E_k(k,x)).^3./27 -
((E1 + E2 + E_k(k,x)).*(- x.*C1(x).^2 - x.*C2(x).^2 + E1.*E2 +
E1.*E_k(k,x) + E2.*E_k(k,x)))./6 + (E1.*E2.*E_k(k,x))./2 -
(C1(x).^2.*E2.*x)./2 - (C2(x).^2.*E1.*x)./2).^(1/3)./2 -
((C1(x).^2.*x)./3 + (C2(x).^2.*x)./3 + (E1 + E2 +
E_k(k,x)).^2./9 - (E1.*E2)./3 - (E1.*E_k(k,x))./3 -
(E2.*E_k(k,x))./3)./(2.*(((((E1 + E2 + E_k(k,x)).*(- x.*C1(x).^2
- x.*C2(x).^2 + E1.*E2 + E1.*E_k(k,x) + E2.*E_k(k,x)))./6 - (E1
+ E2 + E_k(k,x)).^3./27 - (E1.*E2.*E_k(k,x))./2 +
(C1(x).^2.*E2.*x)./2 + (C2(x).^2.*E1.*x)./2).^2 -
((C1(x).^2.*x)./3 + (C2(x).^2.*x)./3 + (E1 + E2 +
E_k(k,x)).^2./9 - (E1.*E2)./3 - (E1.*E_k(k,x))./3 -
(E2.*E_k(k,x))./3).^3).^(1/2) + (E1 + E2 + E_k(k,x)).^3./27 -
((E1 + E2 + E_k(k,x)).*(- x.*C1(x).^2 - x.*C2(x).^2 + E1.*E2 +
E1.*E_k(k,x) + E2.*E_k(k,x)))./6 + (E1.*E2.*E_k(k,x))./2 -
(C1(x).^2.*E2.*x)./2 - (C2(x).^2.*E1.*x)./2).^(1/3));

% test plot inputs
k = -8e7:20e4:8e7;
%x = 0.0; % mat2 concentration

% Econduction and valence bands for ZnOTe
% Evalence band
Ep_val_mat2 = Eplus_mat2(k,C1(x), x, Ec_level);     %E+ Vband
Em_val_mat2 = Eminus_mat2(k, C1(x), x, Ec_level);   %E- Vband
Ec_level_val = Ec_level*ones(1,length(k));          %Defect
acceptor level of ni

%Econduction band
Econd = E_k(k,x);
Ecband1 = E_sol1(k,x, Ec_level_1, Ec_level);   %E1 Cband
Ecband2 = E_sol2(k,x, Ec_level_1, Ec_level);   %E2 Cband
Ecband3 = E_sol3(k,x, Ec_level_1, Ec_level);   %E3 Cband
```

```
Ec_level_con1 = Ec_level_1*ones(1,length(k));          %Defect
donor level of ni
Ec_level_con2 = Ec_level*ones(1, length(k));
% levels for plotting
Ev_level_plot = Ec_level * ones(1, length(k));
Ec_level_plot = Ec_level_1 * ones(1, length(k));

figure(1);

plot(k, Ecband1, 'linewidth', 3);
hold on
plot(k, Ecband2, k, Ecband3, 'linewidth', 3);
plot(k,Ec_level_con1,'k:','linewidth', 2);
plot(k,Ec_level_con2,'k--','linewidth', 1);
%plot(k, Ep_val_mat2+8, k, 'linewidth', 3);
%plot(k, Em_val_mat2+8, 'linewidth', 3);

hold off

%legend('E1 for Cb','E2 for CB', 'E3 for CB', 'Ni acceptor
level', 'Ni donor level',  ...
 %   'E+ for VB', 'E- for VB','location', 'bestoutside');

titlestr = [mat1_name '=' num2str(1-x) ', ' ...
            mat2_name '=' num2str(x)];

% titlestr = [alloy_name ' with ' ...
%             mat1_name '=' num2str(1-x) ', ' ...
%             mat2_name '=' num2str(x)];
title(titlestr)
axis([-8e7 8e7 -7 -2]);

xlabel('k [cm^{-1}]')
ylabel('Energy Relative to Vacuum [eV]');

set(gca,'XMinorTick','on','YMinorTick','on');
set(gca, 'fontsize', 18, 'fontname','Arial');

%x=0.15
figure(2)

%plot(k, Econd, 'linewidth', 3);
%hold on
plot(k, Ecband1, 'linewidth', 3);
hold on
plot(k, Ecband2,  'linewidth', 3);
plot(k, Ecband3, 'linewidth', 3);
```

```
hold on
plot(k,Ec_level_con1,'k:','linewidth', 2);
hold on
plot(k,Ec_level_con2,'k--','linewidth', 1);

%plot(k, Evalence(k,x), 'linewidth', 3);
plot(k, Ep_val_mat2, 'linewidth', 3);
plot(k, Em_val_mat2, 'linewidth', 3);
plot(k, Evalence(k,x), 'linewidth', 3);
hold off
titlestr = [mat1_name '=' num2str(1-x) ', ' ...
            mat2_name '=' num2str(x)];

% titlestr = [alloy_name ' with ' ...
%             mat1_name '=' num2str(1-x) ', ' ...
%             mat2_name '=' num2str(x)];
title(titlestr)
axis([-8e7 8e7 -9 0]);

xlabel('k [cm^{-1}]')
ylabel('Energy Relative to Vacuum [eV]');

set(gca,'XMinorTick','on','YMinorTick','on');
set(gca, 'fontsize', 18, 'fontname','Arial');


% %% Valence and Econduction band over whole COmposition range
% VBAC_val_min = @(k,x) [Eminus_mat2(k(1:end-1), C1(x(1:end-1)),
...
%             x(1:end-1), Ec_level), Ec_mat2]; % E valence band
% VBAC_val_plus = @(k,x) [Eplus_mat2(k(1:end-1), C1(x(1:end-1)),
...
%             x(1:end-1), Ec_level), Ec_mat2]; % E valence band
VBAC_val_min = @(k,x) Eminus_mat2(k, C1(x), ...
            x, Ec_level); % E valence band
VBAC_val_plus = @(k,x) Eplus_mat2(k, C1(x), ...
            x, Ec_level); % E valence band
E conduction band
CBAC_1 = @(k,x) E_sol1(k, ...
            x, Ec_level_1,Ec_level); % E conduction band
E conduction band
CBAC_2 = @(k,x) E_sol2(k, ...
            x, Ec_level_1,Ec_level); % E conduction band
% CBAC_3 = @(k,x) [E_sol3(k(1:end-1), ...
%             x(1:end-1), Ec_level_1,Ec_level), Ec_mat2]; % E
conduction band
CBAC_3 = @(k,x) E_sol3(k, ...
```

```
            x, Ec_level_1,Ec_level); % E conduction band
%
%% To calculate the width of E_sol2 as a function of composition

x = linspace(0,1, length(k));
k = zeros(1, length(x));
%
% To calculate the width of E_sol2 as a function of composition
width2= Ec_level_1 - E_sol2(k,x,Ec_level_1, Ec_level);
figure(3)

%plot(x, width2)

x2= [0.41 0.434 0.394 0.35 0.35 0.29 0.27 0.24 0.24 0.16 0.12
0.11...
    0.062 0.03 0.015 0];
mobil=[1.64 7.3 0.9935 5.433 1.5 9.23 12.18 22.26 16.7 27.1...
    38.7 36 50.6 63.6 100.2 103];

 [hAx,hLine1,hLine2]=plotyy(x.*100,width2,x2.*100,mobil,'plot');
% string

%set(gca, 'fontsize', 22);
xlabel('Ni Content (%)','fontsize',22);
ylabel(hAx(1),'E_d_a- E_2(k) [eV] ','fontsize', 22) % left y-
axis
ylabel(hAx(2),'Mobility (cm^2/V-S)','fontsize', 22) % right y-
axis
set(gca, 'fontsize', 16, 'fontname','Arial');
%ax.YAxis(2).LabelFontSizeMultiplier = 1.5
%ax.YAxis(2).FontSize=22;
set(hAx(2), 'fontsize', 16);
%set(ax,'FontSize',12)

%%

figure(4)

width=[1.1,1.00663517073649, 0.928267734588733, 0.7840,0.5998,
0.5652...
    0.4391,0.2540,0.2540,0.2078 ,0.1828,0.1281,0.1281,0.1009,
0.0820, 0.0928];

mobility=[103, 100.2, 63.6, 50.6, 36, 38.7, 27.1,16.7, 22.26,
12.18,...
    9.23, 1.5, 5.433, 0.9935, 7.3, 1.64];
plot(mobility, width,'*','linewidth', 1);
```

```
xlabel(['Mobility (cm^2/V-S)']);
ylabel('E_d_a- E_2(k) [eV]');
%title('Width of E_2(k)')

set(gca,'XMinorTick','on','YMinorTick','on');
set(gca, 'fontsize', 22, 'fontname','Arial');

%% Calculate band edges
x = linspace(0,1, length(k));
k = zeros(1, length(x));


figure(9);

O = Ec_level*ones(1,length(x));
I = Ec_level_1*ones(1,length(x));
P3=plot(x.*100, CBAC_1(k,x),'-','linewidth', 2,
'Color',[0,1,0]);
hold on
P4=plot (x.*100, CBAC_2(k,x),'-', 'linewidth', 2,
'Color',[0,0,1]);
P5=plot (x.*100, CBAC_3(k,x),'-', 'linewidth', 2,
'Color',[0.3,0.7,1]);
P6=plot(x.*100, VBAC_val_plus(k,x),'-', 'linewidth', 2,
'linewidth', 2, 'Color',[0,1,1]);

hold on
P7=plot(x.*100, VBAC_val_min(k,x),'-','linewidth', 2,
'linewidth', 2, 'Color',[1,0,1]);
P1=plot(x.*100,O,'k:','linewidth', 3, 'Color',[1,0,0]);
P2=plot(x.*100,I,'k:','linewidth', 3, 'Color',[0,0,0]);
scatter(ni.*100, energy, 'ks')
hold off
axis([-0.005 1.01*100 -8.5 -1]);

legend([P2 P1 P3 P4 P5 P6 P7],'Ni-acceptor level','Ni-donor
level', ...
    'E_C_1','E_C_2','E_C_3', 'E_V_1','E_V_2', 'location',
'bestoutside');

xlabel('Ni Content (%)');
ylabel('Energy with respect to vacuum level[eV]');

set(gca,'XMinorTick','on','YMinorTick','on');
set(gca, 'fontsize', 22, 'fontname','Arial');

%% calculate band gap
```

```
Eg_val1 = CBAC_1(k,x) - VBAC_val_min(k,x);
Eg_val2 = CBAC_2(k,x) - VBAC_val_min(k,x);
Eg_val3 = CBAC_3(k,x) - VBAC_val_min(k,x);
%Eg_val32 = CBAC_2(k,x) - VBAC_val_plus(k,x);
Eg_p1 = CBAC_1(k,x) - VBAC_val_plus(k,x);

figure(10)
h01 = plot(x(1:205)*100, Eg_val1(1:205),'m--', 'linewidth', 1,
'Color',[1,0,0]);
hold on
h02 = plot(x(205:600)*100, Eg_val1(205:600),'m-', 'linewidth',
3, 'Color',[1,0,0]);
hold on
h03 = plot(x(205:end)*100, Eg_val1(205:end),'m--', 'linewidth',
1, 'Color',[1,0,0]);
h11 = plot(x(1:205)*100, Eg_val2(1:205),'r-', 'linewidth', 3,
'Color',[0,0,0]);
h12 = plot(x(205:end)*100, Eg_val2(205:end),'r--', 'linewidth',
1, 'Color',[0,0,0]);
%h3 = plot(x, Eg_val3,'r-', 'linewidth', 1, 'Color',[0,1,1]);
h41 = plot(x(1:600)*100, Eg_p1(1:600),'r--', 'linewidth', 1,
'Color',[0.3,0.6,1]);
h42 = plot(x(600:end)*100, Eg_p1(600:end),'r-', 'linewidth', 3,
'Color',[0.3,0.6,1]);
%h5 = plot(x, Eg_val32,'r-', 'linewidth', 1,
'Color',[1,0.5,0.5]);
scatter(nieg*100, bandgap, 'ks')
hold off
axis([-0.02 100 0 5]);
xlabel(['Ni Composition (%)']);
ylabel('Energy [eV]');

%legend([h0,h1,h3],'Bandgap VB E- to CB E-', 'Bandgap VB E- to
CB E+', 'Bandgap VB E+ to CB E+', 'experimental Eg');
set(gca,'XMinorTick','on','YMinorTick','on');
set(gca, 'fontsize', 22, 'fontname','Arial');
```

References

[1] W. Shockley.United States of America Patent 2, 569 347., 1951.

[2] H. Kroemer, *RCA Rev.,* vol. 18, p. 332, 1957.

[3] H. Kroemer, *Prc. IEEE,* vol. 51, p. 1782, 1963.

[4] Z. I. Alferov, V. M. Andreev, D. Z. Garbuzov, Y. V. Zhilyaev, E. P. Morozov, E. L. Portnoi and V. G. Trofim, *Soviet Physics Semiconductors,* vol. 9, no. 4, pp. 1573-1575, 1971.

[5] I. Hayashi, M. B. Panish, P. W. Foy and a. S. Sumski, *Applied Physics Letters,* vol. 17, p. 109, 1970.

[6] F. Capasso, *Science,* vol. 235, pp. 172-176, 1987.

[7] H. Föll, "Wavelength Engineering," University of Kiel, [Online]. Available: http://www.tf.uni kiel.de/matwis/amat/semi_en/kap_5/backbone/r5_1_4.html.

[8] A.-Y. Cho and J. Arthur, Progress in Solid-State Chemistry, vol. 10, New York: Pergamon, 1975, p. 157.

[9] M. Panish, *Science,* vol. 209, p. 916, 1980.

[10] K. Seeger, Semiconductor Physics, Berlin: Springer, 1991.

[11] D. Norris and M. Bawendi, *Physical Review B,* vol. 53, p. 24, 1996.

[12] G. Dohler, "Journal of Vacuum Science and Technology B," vol. 1, p. 278, 1983.

[13] I. Vurgaftman, J. Meyer and L. Ram-Mohan, *Applied Physics Review,* vol. 89, p. 5815, 2001.

[14] J. A. V. Vechten and T. K. Bergstresser, *Physical Review B,* vol. 1, p. 3351, 1970.

[15] A. Rockett, The Materials Science of Semiconductor, Springer U.S., 2008.

[16] M. Grundmann, The Physics of Semiconductors, 2 ed., Berlin: Springer-Verlag, 2010.

[17] S. Nakamura, *Journal of Vacuum Science and Technology A,* vol. 13, p. 705, 1995.

[18] H. Hove and J. Cuomo, *Applied Physics Letters,* vol. 20, p. 71, 1972.

[19] J. Wu and W.Walukiewicz, "Superlattices and Microstructures," vol. 34, p. 63, 2003.

[20] H. Morkoc, Nitride Semiconductor and Devices, Heidelberg: Springer, 1999.

[21] Y. Lam, J. P. Loehr and J. Singh, *IEEE Journal of Quantum Electronics,* vol. 28, p. 1248, 1992.

[22] A. W. Mabbitt, "Solid State Communications," vol. 9, p. 245, 1971.

[23] F. Fuchs, U. Weime, W. Pletschen, J. Schmitz, E. Ahlswede, M. Walther, J. Wagner and P. Koidl, *Applied Physics Letters,* vol. 71, p. 3251, 1997.

[24] I. Vurgaftman, J. R. Meyer and L. R. Ram-Mohan, "IEEE Photonics Technology Letters," vol. 9, p. 170, 1997.

[25] H. Xie and W. I. Wang, "Applied Physics Letters," vol. 63, p. 776, 1993.

[26] M. Afzaal and P. O'Brien, *Journal of Materials Chemistry,* vol. 16, p. 1597, 2006.

[27] G. Neumark, *Materials Science and Engineering,* vol. R21, p. 1, 1997.

[28] T. Minami, *Semiconductor Science and Technology,* vol. 20, p. S35, 2005.

[29] R. G. Gordon, *MRS Bulletin ,* vol. 25, p. 52, 2000.

[30] C. G. Granqvist, *Solar Energy Materials and Solar Cells,* vol. 91, p. 1529, 2007.

[31] D. C. Paine, B. Yaglioglu and J. Berry, Handbook of Transparent Conductors, Boston: Springer U.S., 2010.

[32] M. McCluskey and E. Haller, Dopants and Defects in Semiconductors, Taylor and Francis CRC Press, 2012.

[33] E. Fortunato, D. Ginley, H. Honoso and D. Paine, *MRS Bulletin ,* vol. 32, p. 242, 2007.

[34] E. Burstein, *Physical Review,* vol. 92, p. 632, 1954.

[35] T. S. Moss, Optical Properties of Semiconductors, London: Butterworths, 1961.

[36] J. I. Pankove, Optical Processes in Semiconductors, Courier Dover Publications, 2012.

[37] M.Chen, Z. Pei, X. Wang, Y. Yu, X. Liu, C. Sun and L. Wen, *Journal of Physics D: Applied Physics,* vol. 33, p. 2538, 2000.

[38] Y-M.Chiang, D. Birnie and W. Kingery, Physical Ceramics-Principles for Ceramic Science and Engineering (The MIT Series in Material Science and Engineering), New York: Wiley, 1996.

[39] J. Tersoff, "Journal of Vacuum Science and Technology B," vol. 4, p. 1066, 1986.

[40] V. I. Kuznetsov, T. Logvinenko, P. Lugakov and U. Tkachev, *Soviet Physics Semiconductors,* vol. 9, p. 491, 1975.

[41] W. Walukiewicz, " Physical Review B," vol. 37, p. 4760, 1988.

[42] W. Walukiewicz, *Applied Physics Letters,* vol. 54, p. 5094, 1989.

[43] W. Walukiewicz, *Physica B,* vol. 123, pp. 302-303, 2001.

[44] P. King, T. Veal, P. H. Jefferson, J. Zuñiga-Pérez, V. Muñoz-Sanjosé and C. McConville, *Physical Review B,* vol. 79, p. 035203, 2009.

[45] D. S. Ginley and C. Bright, *MRS Bulletin,* vol. 25, p. 15, 2000.

[46] B. J. Ingram, B. Gonzalez, D. R. Kammle, M. I. Bertoni and T. O. Mason, *Journal of Electrochemistry,* vol. 13, p. 164, 2004.

[47] T. Mason, G. Gonzalez, D. Kammler, N. Mansourian-Hadavi and B. Ingram, *Thin Solid Films,* vol. 411, p. 106, 2005.

[48] M. Burbano, D. Scanlon and G. Watson, *Journal of the American Chemical Society,* vol. 133, p. 15065, 2011.

[49] D. Detert, *Bandgap Engineering and Doping of CdO, Ph.D Dissertation,* Berkeley, 2014.

[50] W. Walukiewicz, *Journal of Crystal Growth,* vol. 159, p. 244, 1996.

[51] S. Zhang, S.-H. Wei and A. Zunger, *Journal of Applied Physics,* vol. 83, p. 6, 1998.

[52] D. T. Speaks, M. Mayer, K. Yu, S. Mao, E. Haller and W. Walukiewicz, *Journal of Applied Physics,* vol. 107, p. 113706, 2010.

[53] S. X. Li, K. M. Yu, J. Wu, R. E. Jones, W. Walukiewicz, J. W. Ager, W. S. III, E. E. Haller, H. Lu and W. Schaff, *Physical Review B,* vol. 71, p. 161201, 2005.

[54] P. King and T. Veal, *Journal of Physics: Condensed Matter,* vol. 23, p. 334214, 2011.

[55] F. Allen and G. Gobeli, *Physical Review,* vol. 127, p. 150, 1962.

[56] W. Monch, P. Koke and S. Kruege, *Journal of Vacuum Science and Technology,* vol. 19,

p. 313, 1981.

[57] S. Svensson, T. A. J. Kanski and P. Nilsson, *Journal of Vacuum Science and Technology B,* vol. 2, p. 235, 1984.

[58] W. Spicer, I. Lindau, P. Gregory, C. Garner, P. Pianetta and P. Chye, *Journal of Vacuum Science and Technology,* vol. 13, p. 780, 1976.

[59] P. King, T. Veal, D. Payne, A. Bourlange, R. Egdell and C. McConville, *Physical Review Letters,* vol. 101, p. 116808, 2008.

[60] P. King, T. D. Veal, F. Fuchs, C. Y. Wang, D. J. Payne, H. Z. G. R. B. V. C. A. Bourlange, O. Ambacher, R. G. Egdell, F. Bechstedt and C. F. McConville, *Physical Review B,* vol. 79, p. 205211, 2009.

[61] J.Wu, *Journal of Applied Physics ,* vol. 106, p. 011101, 2009.

[62] P. King, T. Veal and C. McConville, *Journal of Physics: Condensed Matter,* vol. 21, p. 174201, 2009.

[63] P. D. C. King, T. D. Veal, P. H. Jefferson, L. F. J. P. C. F. M. S. A. Hatfield, F. Fuchs, J. Furthmüller, H. L. F. Bechstedt and W. J. Schaff, *Physical Review B,* vol. 77, p. 045316, 2008.

[64] L. Piper, T. Veal, M. Lowe and C. McConville, *Physical Review B,* vol. 73, p. 195321, 2006.

[65] P. King, T. Veal, A. Schleife, J. Zuñiga-Pérez, B. Martel, F. F. V. M.-S. F. B. P. H. Jefferson and C. McConville, *Physical Review B,* vol. 79, p. 205205, 2009.

[66] T. J. Coutts, X. L. D. L. Young, W. P. Mulligan and X. Wu, *Journal of Vacuum Science and Technology,* vol. 18, p. 2646, 2000.

[67] A. Tsukazaki, L. Dai, L. Zhang, R. Yang, L. Li, T. Guo and Y. Yan, *Nature Materials,* vol. 4, p. 42, 2005.

[68] A. P. Ramirez, *Science,* vol. 315, p. 1377, 2007.

[69] Ü. Özgür, Y. I. Alivov, C. Liu, A. Teke, M. A. Reshchikov, S.Doğan, V. Avrutin, S.-J. Cho and H. Morkoç, *Journal of Applied Physics,* vol. 98, p. 041301, 2005.

[70] A. Janotti and C. G. V. d. Walle, *Reports on Progress in Physics,* vol. 72, p. 126501, 2009.

[71] T. Makino, Y. Segawa, M. Kawasaki, A. Ohtomo, R. Shiroki, K. Tamura, T. Yasuda and H. Koinuma, *Applied Physics Letters,* vol. 78, p. 1237, 2001.

[72] J. Ishihara, A. Nakamura, S. Shigemori, T. Aoki and J. Temmyo, *Applied Physics Letters,* vol. 89, p. 091914, 2006.

[73] Y. Zhu, G. Chen, H. Ye, A. Walsh, C. Moon and S.-H. Wei, *Physical Review B,* vol. 77, p. 2008.

[74] D. Detert, S. M. Lim, K. Tom, A. Luce, A. Anders, O. Dubon, K.M.Yu and W. Walukiewicz, *Applied Physics Letters,* vol. 102, p. 232103, 2013.

[75] G. Chen, K. M. Yu, L. A. Reichertz and W. Walukiewicz, *Applied Physics Letters,* vol. 103, p. 41902, 2013.

[76] K. Takahashi, A. Yoshikawa and A.Sandhu, Wide Bandgap Semiconductors: Fundamental Properties and Modern Photonic and Electronic Devices, 1 ed., Berlin: Springer-Verlag Berlin Heidelberg, 2007.

[77] H.Landolt and R. Bornstein, Landolt-Bornstein - Group III Condensed Matter, Berlin: Springer-Verlag, Heidelberg, 2002.

[78] R. Reeber and K. Wang, *Journal of Materials Research,* vol. 15, p. 1, 2000.

[79] H. Maruska and J. Tietjen, *Applied Physics Letters,* vol. 15, p. 327, 1969.

[80] M. Leszczynsk, T. Suski, H. Teisseyre, P. Perlin, I. Grzegory, J. Jun, S. Porowski and T. Moustakas, *Journal of Applied Physics,* vol. 76, p. 4909, 1994.

[81] W. Shan, B. D. Little, A. J. Fischer, J. J. Song, B. Goldenberg, W. G. Perry, M. D. Bremser and R. F. Davis, *Physical Review B,* vol. 54, p. 16369, 1996.

[82] J. F. Muth, J. H. Lee, I. K. Shmagin, R. M. Kolbas, H. C. Casey, B. Keller, U. Mishra and S. DenBaars, *Applied Physics Letters,* vol. 71, p. 2572, 1997.

[83] D. C. Look, J. W. Hemsky and J. R. Sizelove, *Physical Review Letters,* vol. 82, p. 2552, 1999.

[84] D. C. Reynolds, D. C. Look and B. Jogai, *Solid State Communications,* vol. 99, p. 873, 1996.

[85] M. McCluskey and S. Jokela, *Journal of Applied Physics,* vol. 106, p. 071101, 2009.

[86] A. F. Kohan, G. Ceder, D. Morgan and C. G. V. d. Wallle, *Physical Review B,* vol. 61, p. 15019, 2000.

[87] A. Janotti and C. G. V. d. Walle, *Physical Review B,* vol. 76, p. 165202, 2007.

[88] S. Dutta, M. Chakrabarti, S. Chattopadhay, D. Jana, D. Sanyal and A. Sarkar, *Journal of Applied Physics,* vol. 98, p. 053513, 2005.

[89] S. Y. Myong, S. J. Baik, C. H. Lee, W. Y. Cho and K. S. Lim, *Japan Journal of Applied Physics,* vol. 36, p. 1078, 1997.

[90] B. M. Ataev, A. M. Bagamadova, A. M. Djabrailov, V. V. Mamedo and R. A. Rabadanov, *Thin Solid Films,* vol. 260, p. 19, 1995.

[91] M. A. Mayer, D. Speaks, J. Denlinger, K. Yu, L. Reichertz, J. Beeman, E. Haller and W. Walukiewicz, *The Journal of Physical Chemistry C,* vol. 116, p. 15281, 2012.

[92] Y. Xiao, S. Kong, E. Kim and C. Chung, *Solar Energy Materials and Solar Cells,* vol. 95, p. 264, 2011.

[93] A. L. Yang, H. P. Song, X. L. Liu, Y. G. H. Y. Wei, G. L. Zheng, C. M. Jiao, S. Y. Yang, Q. S. Zhu and Z. G. Wang, *Applied Physics Letters,* vol. 94, p. 052101, 2009.

[94] D. M. Roessler and W. C. Walker, *Physical Review,* vol. 159, p. 733, 1967.

[95] S. Heo, E. Cho, H.-I. Lee, G. Park, H. Kang, T. Nagatomi, P. Choi and B.-D. Choi, *AIP Advances,* vol. 5, p. 077167, 2015.

[96] D. Detert, K. Tom, C. Battaglia, J. Denlinger, S. H. N. Lim, A. Javey, A. Anders, K. M. Y. O . Dubon and W. Walukiewicz, *Journal of Applied Physics,* vol. 115, p. 233708, 2014.

[97] S. Farahani, V-Munoz-Sanjose, J. Zuniga-Perez, C. McConville and T. Veal, *Applied Physics Letters,* vol. 102, p. 022102, 2013.

[98] M. Burbano, D. O. Scanlon and G. W. Watson, *Journal of the American Chemical Society,* vol. 113, p. 15065, 2011.

[99] K.M.Yu, M. Mayer, D. Speaks, H.He and R. Zhao, *Journal of Applied Physics,* vol. 111, p. 123505, 2012.

[100] C. Francis, D. Detert, G. Chen, O. Dubón, K.M.Yu and W. Walukiewicz, *Applied Physics Letters,* vol. 106, p. 022110, 2015.

[101] H. Finkenrath, Physics of II-VI and III-V Compounds, Semi-Magnetic Semiconductors, Landolt-Bornstein: Numerical Data and Functional Relationships in Science and Technology. Group III: Crystal and Solid State Physics, vol. 17B, Berlin: Springer, 1982.

[102] A. Wang, J. R. Babcock, N. L. Edleman, A. Metz, M. A. Lane, R. Asahi, V. P. Dravid, C. Kannewurf, A. J. Freeman and T. J. Marks, *Proceedings of the National Academy of Science U.S.A. ,* vol. 98, p. 7113, 2001.

[103] L. Wang, Y. Yang, S. Jin and J. M. Tobin, *Applied Physics Letters,* vol. 88, p. 162115, 2006.

[104] Y. Yang, S. Jin, J. E. Medvedeva, J. R. Ireland, A. W. Metz, J. Ni, M. C.Hersam, A. J. Freeman and T. J. Marks, *Journal of the Americal Chemical Society,* vol. 127, p. 8796, 2005.

[105] S. Jin, Y. Yang, J. E. Medvedeva, L. Wang, N. C. S. Li, J. R. Ireland, A. W. Metz, J. Ni, M. C. Hersam, A. J. Freeman and T. J. Marks, *Chemistry of Materials,* vol. 20, p. 220, 2008.

[106] M. Yan, M. Lane, C. R. Kannewurf and R. P. H. Chang, *Applied Physics Letters,* vol. 78, p. 2342, 2001.

[107] J. Santos-Cruz, G. Torres-Delgado, R. Castanedo-Perez, C. I. Zúñiga-Romero and O. Zelaya-Angel, *Thin Solid Films,* vol. 515, p. 5381, 2007.

[108] A. Ohtomo, M. Kawasaki, T. Koida, K. Masubuchi, H. Koinuma, Y. Sakura, Y. Yoshida, T. Yasuda and Y. Segawa, *Applied Physics Letters,* vol. 72, p. 2466, 1998.

[109] Y. Matsumoto, M. Murakami, Z. Jin, A. Ohtomo, M. Lippmaa, M. Kawasaki and H. Koinuma, *Japanese Journal of Applied Physics,* vol. 38, p. 603, 1999.

[110] T. Maemoto, N. Ichiba, H. Ishii, S. Sasa and M. Inoue, *Journal of Physics: Conference Series,* vol. 59, p. 670, 2007.

[111] B. Laumer, F. Schuster, M. Stutzmann, A. Bergmaier, G. Dollinger and M. Eickhoff, *Journal of Applied Physics,* vol. 113, p. 233512, 2013.

[112] Y. Hu, B. Cai, Z. Hu, Y. Liu, S. Zhang and H. Zeng, *Current Applied Physics ,* vol. 15, p. 423, 2015.

[113] S. Choopun, R. D. Vispute, W. Yang, R. P. Sharma, T. Venkatesan and H. Shen, *Applied Physics Letters,* vol. 80, p. 1529, 2002.

[114] Z. P. Wei, B. Yao, Z. Z. Zhang, Y. M. Lu, D. Z. Shen, B. H. Li, X. H. Wang, J. Y. Zhang, D. X. Zhao, X. W. Fan and Z. Tang, *Applied Physics Letters,* vol. 89, p. 102104, 2006.

[115] Y. Li, B. Yao, Y. M. Lu, Z. P. Wei, Y. Q. Gai, C. J. Zheng, Z. Z. Zhang, B. H. Li, D. Z. Shen, X. W. Fan and Z. Tang, *Applied Physics Letters,* vol. 91, p. 232115, 2007.

[116] C. X. Shan, J. S. Liu, Y. J. Lu, B. H. Li, Francis, C. C. Ling and D. Z. Shen, *Optical Letters,* vol. 40, p. 3041, 2015.

[117] Y.-S. Choi, C.-G. Lee and S. Cho, *Thin Solid Films,* vol. 289, p. 153, 1996.

[118] T. Gruber, C. Kirchner, R. Kling, F. Reuss and A. Waag, *Applied Physics Letters,* vol. 83, p. 3290, 2003.

[119] O. Vigil, L. Vaillant, F. Cruz, G. Santana, A. Morales-Acevedo and G.Contreras-Puente, *Thin Solid Films,* vol. 53, p. 361, 2000.

[120] D. W. Ma, Z. Z. Ye and L. L. Chen, *Physica Status Solidi (a),* vol. 201, p. 2929, 2004.

[121] X. J. Wang, I. A. Buyanova, W. M. Chen, M. Izadifard, S. Rawal, D. P. Norton, S. J. Pearton, A. Osinsky, J. W. Dong and A. Dabiran, *Applied Physics Letters,* vol. 89, p. 151909, 2006.

[122] A. Schleife, M. Eisenacher, C. Rödl, F. Fuchs, J. Furthmüller and F. Bechstedt, *Physical Review B,* vol. 81, p. 245210, 2010.

[123] J. Ishihara, A. Nakamura, S.Shigemori, T. Aoki and J. Temmyo, *Applied Physics Letters,* vol. 89, p. 091914, 2006.

[124] U. Paliwal, T. Bredow and K. B. Joshi, *AIP Conference Proceedings,* vol. 1447, p. 1037, 2012.

[125] F. Atay, I. Akyuz, S. Kose, E. Ketenci and V. Bilgin, *Journal of Materials Science: Materials in Electronics,* vol. 22, p. 492, 2011.

[126] H.Ohta, M. Kamiya, T. Kamiya, M. Hirano and H. Hosono, *Thin Solid Films ,* vol. 445, p. 317, 2003.

[127] A. Banerjee and K. Chattopadhyay, *Progress in Crystal Growth and Characterization of Materials,* vol. 50, p. 52, 2005.

[128] H. Kawazoe, H. Yanagi, K. Ueda and H. Hosono, *MRS Bulletin,* vol. 28, 2000.

[129] S. Fraga, S. Karwowski and K. Saxena, Handbook of Atomic Data, Amsterdam: Elseveir, 1976.

[130] H. Sato, T. Minami, S. Takata and T. Yamata, *Thin Solid Films,* vol. 236, p. 27, 1993.

[131] H.-L. Chen, Y.-M. Lu and W.-S. Hwang, *Surface and Coatings Technology,* vol. 198, p. 138, 2005.

[132] H. Chen, Y.-M. Lu and W.-S. Hwang, *Thin Solid Films,* vol. 498, p. 266, 2006.

[133] H. Liu, W. Zheng, X. Yan and B. Feng, *Journal of Alloy Compounds,* vol. 356, p. 462, 2008.

[134] A. B. Kunz, *Journal of Physics C ,* vol. 445, p. 14, 1981.

[135] R. Powell and W. Spicer, *Physical Review B,* vol. 2, p. 2182, 1970.

[136] W.-L. Jang, Y.-M. Lu, W.-S. Hwang, T.-L. Hsiung and H. Wang, *Applied Physics Letters,* vol. 94, p. 062103, 2009.

[137] P. Kofstad, Nonstoichiometry, Diffusion, and Electrical Conductivity in Binary Metal Oxides, New York: Wiley, 1972.

[138] A. Kuzmin, J. Purans and A. Rodionov, *Journal of Physics: Condensed Matter,* vol. 9, p. 6979, 1997.

[139] D. Adler and J. Feinleib, *Physical Review B,* vol. 2, p. 3112, 1970.

[140] H. B. Wu and L. S. Wang, *Journal of Physical Chemistry,* vol. 107, p. 16, 1997.

[141] R. Deng, B. Yao, Y. F. Li, Y. M. Zhao, B. H. Li, C. X. Shan, Z. Zhang, D. X. Zhao, J. Y. Zhang, D. Z. Shen and X. W. Fan, *Applied Physics Letters,* vol. 94, p. 022108, 2009.

[142] T. Ramond, G. Davico, F.Hellberg, F.Svedberg, P.Salen, P.Soderqvist and

W.C.Lineberger, *Journal of Moleular Spectroscopy,* vol. 216, p. 1, 2002.

[143] T. Veal, P. King and C. McConville, Functional Metal Oxide Nanostructure Springer Series in materials Science, Springer, 2012.

[144] Y. Dou, R. Egdell, D. Law, N. Harrison and B. Searle, *Journal of Physics: Condensed Matter,* vol. 10, p. 8447, 1998.

[145] L. Piper, A. Demasi, K. Smith, A. Schleife, F. Fuchs, F. Bechstedt, J. Zuniga-Pérez and V. Munoz-Sanjosé, *Physical Review B,* vol. 77, p. 125204, 2008.

[146] A. Schleife, F. Fuchs, J. Furthmüller and F. Bechstedt, *Physical Review B,* vol. 73, p. 245212, 2006.

[147] I. Demchenko, M. Chernyshova, T. Tyliszczak, J. Denlinger, K. Yu, D. Speaks, O. Hemmers, W. Walukiewicz, G. Derkachov and K. Lawniczak-Jablonska, *Journal of Electron Spectroscopy and Related Phenomena,* vol. 184, p. 249, 2011.

[148] Z. Shen, R. List, D. Dessau, B. Wells, O. Jepsen, A. Arko, R. Barttlet, C. Shih, F. Parmigiani, J. Huang and P. Lindberg, *Physical Review B,* vol. 44, p. 3604, 1991.

[149] S. Zhao, K. Zhao, Q. Zhou, Y. Zhou, S. Wang and T. Ning, *Journal of Physics D,* vol. 40, p. 4489, 2007.

[150] S. D. Singh, V. Nandanwar, H. Srivastava, A. K. Yadav, A. Bhakar, P. R. Sagdeo, A. K. Sinha and T. Ganguli, *Dalton Transactions,* vol. 44, p. 14793, 2015.

[151] Y. R. Park and K. J. Kim, *Journal of Crystal Growth,* vol. 258, p. 380, 2005.

[152] D. D. Dogan, Y. Caglar, S. Ilican and M. Caglar, *Journal of Alloy Compounds,* vol. 509, p. 2461, 2011.

[153] Z. G. Yang, L. P. Zhu, Y. M. Guo, Z. Z. Ye and H. Zhao, *Thin Solid Films,* vol. 519, p. 5174, 2011.

[154] F. Omnès, E. Monroy, E. Muñozc and J. L. Reverchond, in *SPIE*, 2007.

[155] C. Niedermeier, M. Råsander, S. Rhode, V. Kachkanov, B. Zou, N. Alford and M. Moram, *Scientific Reports,* vol. 6, p. 31230, 2016.

[156] M. Ohring, Materials Science of Thin Films: Deposition and Structure, Academic Press, 2001.

[157] A. Metz, J. Ireland, J.-G. Zheng, R.P.S.M.Lobo, Y. Yang, J.Ni, C. Stern, V. Dravid, N. Bontemps, C. Kannewurf, K. Poeppelmeier and J. Marks, *Journal of the American Chemical Society,* vol. 126, p. 8477, 2004.

[158] J. Mudd, T. Lee, V. Muñoz-Sanjosé, J. Zúñiga-Pérez, D. Hesp, J. M. Kahk, D. J. Payne, R. G. Egdell and C. F. McConville, *Physical Review B,* vol. 89, p. 035203S, 2014.

[159] D. K. M. Yu, "Rutherford Backscattering Spectrometry and Related Techniques," Berkeley and Hong Kong, 2014.

[160] M. Mayer, in *AIP Conference Proceedings*, 1999.

[161] W. K. Chu, J. W. Mayer, M. A. Nicolet, T. M. Buck, G. Amsel and F. Eisen, *Thin Solid Films,* vol. 17, p. 1, 1973.

[162] W.-K. M. J. W. Chu and M.-A. Nicolet, Backscattering Spectrometry, New York: Academic Press Inc., 1978.

[163] A. L. Patterson, *Physical Review,* vol. 56, p. 978, 1939.

[164] B. D. Cullity and S. R. Stock, Elements of X-ray Diffraction, Upper Saddle River: Prentice Hall, 2001.

[165] C. Kittel, Introduction to Solid State Physics, 8 ed., Hoboken: John Wiley & Sons Inc., 2005.

[166] L. V. d. Pauw, *Phil. Technical Review,* vol. 20, p. 220, 1958.

[167] O. Heavens, Optical Properties of Thin Solid Films, Courier Dover Publications, 1991.

[168] K. F. Berggren and B. E. Sernelius, *Physical Review B,* vol. 24, p. 1971, 1981.

[169] W. Walukiewicz, *Physical Review B,* vol. 41, p. 10218, 1990.

[170] E. O. Kane, *Journal of Physics and Chemistry of Solids,* vol. 1, p. 249, 1957.

[171] M. Jaquez, K. Yu, M. Ting, M. Hettick, J. F. Sánchez-Royo, M. Wełna, A. Javey, O. Dubón and W. Walukiewicz, *Journal of Applied Physics,* vol. 118, p. 215702, 2015.

[172] E. García-Hemme, K. Yu, P. Wahnon, G. González-Díaz and W. Walukiewicz, *Applied Physics Letters,* vol. 106, p. 182101, 2015.

[173] J. Wu, W. Walukiewicz, W. Shan, K. Yu, J. A. III, S. Li, E. Haller and H. Lu, *Journal of Applied Physics,* vol. 94, p. 4457, 2003.

[174] J. Langer, C. Delerue, M. Lannoo and H. Heinrich, *Physical Review B,* vol. 38, p. 7723, 1988.

[175] J.Suh, D. Fu, X. Liu, J. Furdyna, K.Yu, W. Walukiewicz and J.Wu, *Physical Review B,* vol. 89, p. 115307, 2014.

[176] R. Smith, Atomic & ion collisions in solids and at surfaces: theory, simulation and applications, Cambridge: Cambridge University Press, 1997.

[177] W. Shan, W. Walukiewicz, J. W. A. III, E. E. Haller, J. F. Geisz, D. J. Friedman, J. M. Olson and S. R. Kurtz, *Physical Review Letters,* vol. 82, p. 1221, 1999.

[178] J. Wu, W. Shan and W. Walukiewicz, *Semiconductor Science Technology,* vol. 17, p. 860, 2002.

[179] N. Segercrantz, K. Yu, M. Ting, W. Sarney, S. Svensson, S. Novikov, C. Foxon and W.Walukiewicz, *Applied Physics Letters,* vol. 107, p. 14204, 2015.

[180] M. A. Mayer, P. R. Stone, N. Miller, H. S. III, O. D. Dubón, E. E.Haller, K. M. Yu, W. Walukiewicz, X. Liu and J. K. Furdyna, *Physical Review B,* vol. 81, p. 045205, 2010.

[181] K. Alberi, J. Wu, W. Walukiewicz, K. Yu, O. Dubon, S. Watkins, C. Wang, X. Liu, Y.-J. Cho and J. Furdyna, *Physical Review B,* vol. 75, p. 045203, 2007.

[182] A. Fujimori, F. Minami and S. Sugano, *Physical Review B,* vol. 29, p. 5225, 1984.

[183] G. A. Sawatzky and J. W. Allen, *Physical Review Letters,* vol. 53, p. 2339, 1984.

[184] S. Hüfner, *Solid State Communications,* vol. 52, p. 793, 1984.

[185] L. Soriano, I. Preda, A. Gutiérrez, S. Palacín, M. Abbate and A. Vollmer, *Physical Review B,* vol. 75, p. 233417, 2007.

[186] M. Biesinger, B. P. Payne, L. Lau, A. Gerson and R. S. C. Smart, *Surace Interface Analysis,* vol. 41, p. 324, 2009.

[187] C. Wagner, W. Riggs, L. Davis and J. Moulder, Handbook of X-ray Photoelectron Spectroscopy, Eden Prairie: Physical Electronics Industries, 1979.

[188] K. Kim, W. Baitinger, J. Amy and N. Winograd, *Journal of Electron Spectrscopy and Related Phenomena,* vol. 5, p. 351, 1974.

[189] M. Ristova, J. Velveska and M. Ristov, *Solar Energy Materials and Solar Cells,* vol. 71, p. 219, 2002.

[190] A. Mansour, *Surface Science Spectroscopy,* vol. 3, p. 231, 1994.

[191] A. Grosvenor, M. Biesinger, R. Smart and N. McIntyre, *Surface Science,* vol. 600, p. 1771, 2006.

[192] A. Carley, S. Jackson, J. O'Shea and M. Roberts, *Surface Science,* vol. 440, p. L868, 1999.

[193] S. Hufner, Photoelectron spectroscopy, Solid State Science Series 82, Berlin: Springer-Verlag, 1995.

[194] M. Ristova, C. Francis, F. Toma, K. Yu and W. Walukiewicz, *Solar Energy Materials and Solar Cells,* vol. 147, p. 127, 2016.

[195] F. Menchini, M. Grilli, T. Dikonimos, A. Mittiga, L. Serenelli, E. Salza, R. Chierchia and M. Tucci, *Physica Status Solidi(c),* vol. 13, p. 1006, 2016.

[196] S. Liu, R. Liu, Y. Chen, S. Ho, J. H. Kim and F. So, *Chemistry of Materials,* vol. 26, p. 4528, 2014.

[197] S. Seo, I. Park, M. Kim, S. Lee, C. Bae, H. Jung, N.-G. Park, J. Kim and H. Shin, *Nanoscale,* vol. 8, p. 11403, 2016.

[198] J. Bandara and H. Weerasinghe, *Solar Energy Materials & Solar Cells,* vol. 85, p. 385, 2005.

[199] X. Xu, Z. Liu, Z. Zuo, M. Zhang, Z. Zhao, Y. Shen, H. Zhou, Q. Chen, Y. Yang and M. Wang, *Nano Letters ,* vol. 15, p. 2402, 2015.

[200] U. Kwon, B.-G. Kim, D. C. Nguyen, J.-H. Park, N. Ha, S.-J. Kim, S. Ko, S. Lee, D. L. and H. J. Park, *Scientific Reports,* vol. 6, p. 30759, 2016.

[201] J. Cui, F. Meng, H. Zhang, K. Cao, H. Yuan, Y. Cheng, F. Huang and M. Wang, *ACS Applied Materials & Interfaces,* vol. 6, p. 22862, 2014.

[202] F. Tuomisto and I. Makkonen, *Review of Modern Phys,* vol. 85, p. 1584, 2013.

[203] S. Dutta, M. Chakrabarti, S. Chattopadhyaay and D. Jana, *Journal of Applied Physics,* vol. 98, p. 053513, 2005.

[204] J. Slotte, F. Tuomisto, K. Saarinen, C. G. Moe, S. Keller and S. P. DenBaars, *Applied Physics Letters,* vol. 90, p. 151908, 2007.

[205] A. Uedono, S. Ishibashi, T. Watanabe, X. Q. W. S. T. Liu, G.Chen, L. W. Sang, M. Sumiya and B. Shen, *Journal of Applied Physics,* vol. 112, p. 014507, 2012.

[206] S. F. Chichibu, K. Hazu, T. Onuma and A. Uedono, *Applied Physics Letters,* vol. 99, p. 051902, 2011.

[207] N. Miller, E. Haller, G.Koblmuller, C. Gallinat, J. Speck and W. Schaff, *Physical Review B,* vol. 84, p. 075315, 2011.

[208] R. Karthick, P. Sathyakam and P. Mallick, *Nature,* vol. 3, p. 815, 2011.

[209] R. B. H. Tahar and N. B. H. Tahar, *Journal of Applied Physics,* vol. 92, p. 8, 2002.

[210] V. I. Fistul and V. M. Vainshtein, *Soviet Physics-Solid State,* vol. 8, p. 2769, 1967.

[211] Z. Zhang, Y. Zhao and M. Zhu, *Applied Physics Letters,* vol. 88, p. 33101, 2006.
[212] T. Bak, *International Journal of Hydrogen Energy ,* vol. 27, p. 991, 2002.
[213] C. G. V. d. Walle and J. Neugebauer, *Nature,* vol. 423, p. 626, 2003.